Towards Bridging the Material Gap between Real-World Catalyst and Ideal Single Crystal Surfaces on Ceria Based Solid Solution

Thesis Submitted to
Academy of Scientific and Innovative Research
For the Award of the Degree of
Doctor of Philosophy in Chemical sciences

by
Anjani Dubey
Registration Number **10CC11A26030**

Under the guidance of
Dr. Chinnakonda S. Gopinath

Catalysis Division
CSIR- National Chemical Laboratory
Pune – 411008, India

राष्ट्रीय रासायनिक प्रयोगशाला
(वैज्ञानिक तथा औद्योगिक अनुसंधान परिषद)
डॉ. होमी भाभा रोड, पुणे - 411 008. भारत
NATIONAL CHEMICAL LABORATORY
(Council of Scientific & Industrial Research)
Dr. Homi Bhabha Road, Pune - 411008. India

Certificate

This is to certify that the work incorporated in this Ph.D. thesis entitled **"Towards Bridging the Material Gap between Real-World Catalyst and Ideal Single Crystal Surfaces on Ceria Based Solid Solution."** submitted by **Mr. Anjani Dubey** to Academy of Scientific and Innovative Research (AcSIR) in fulfillment of their requirements for the award of the Degree Of **Doctor of Philosophy in Chemical Sciences,** embodies original research work under my supervision. I further certify that this work has not been submitted to any other university or institution in part or full for the award of any degree or diploma. Research material obtained from other sources has been duly acknowledged in thesis. Any text, illustration, table etc. used in the thesis is from other sources, have been duly cited and acknowledged.

Date - 17/06/2016

Dr. Chinnakonda S. Gopinath
(Thesis Supervisor)

Catalysis Division and
Center of Excellence on Surface Science
CSIR - National Chemical Laboratory
Dr. Homi Bhabha Road, Pune - 411 008, India

Declaration

I hereby declare that the thesis entitled **"Towards Bridging the Material Gap between Real-World Catalyst and Ideal Single Crystal Surfaces on Ceria Based Solid Solution."** submitted for the degree of **Doctor of Philosophy in Chemical Sciences** to the Academy of Scientific & Innovative Research (AcSIR), has been carried out by me at the Catalysis Division of CSIR-National Chemical Laboratory, Pune under the guidance of **Dr. Chinnakonda S. Gopinath**. Such material as has been obtained by other sources has been duly acknowledged in this thesis. The work is original and has not been submitted in part or full by me for any other degree or diploma to any other Institution or University.

Date - 17/06/2016

CSIR-National Chemical Laboratory,
Pune - 411008

Research Student
Mr. Anjani Dubey

Dedicated to

My Beloved Parents

Brother "Rishabh Dubey"

And my wife "Rama Dubey"

Acknowledgements

During my PhD tenure at CSIR-National chemical laboratory, I have been supported, inspired and accompanied by many people like scientists, friends, non-academic staffs etc. It gives me great privilege to take this opportunity to express my heartfelt gratitude for all of them.

First of all, I would like to thank my teacher and research advisor ***Dr. Chinnakonda S. Gopinath*** *for excellent guidance, incessant encouragement and positive criticism in every respect at all phases of research career. I consider myself extremely fortunate to have a supervisor who not only guided me how to do research and think independently but also taught me discipline, professionalism and shown unique ways to reach goals. I consider him as a gentle and generous person who has brought all round development in me in all perspective of life. I must say, without his help it was not possible for me to complete my research work in time. I am thankful to UGC for awarding junior and senior research fellowship.*

I owe a special debt to Dr. C. P. Vinod and his research student A. C. Sunilsekhar, for giving me the opportunity to have a hand on experience on Spin-coating machine. I would like to pay special thanks to Dr. Satishchandra B. Ogale for his support regarding the use of profilometer instrument. I would like to pay special thanks to Dr. Pankaj Poddar for allowing me to use AFM instrument.

I owe to thank Dr. B. L. V. Prasad, Dr. T. G. Ajithkumar, Dr. P. A. Joy, Dr. C. P. Vinod, Dr. C. V. V. Satyanarayana, Dr. C. V. Rode, Dr. C. S. Gopinath, Dr. R. Nandini Devi and Dr. Sreekumar Kurungot who taught me during my course work in NCL. I also thank Dr. Nirmalya Ballav (IISER, Pune) for appearing my UGC upgradation seminar. I thank to my DAC members Dr. C. P. Vinod, Dr. P. N. Joshi and Dr. Rahul Banerjee for evaluating me at various DAC meetings. I thank Prof. Ashwini Kumar Nangia, Director, NCL, Dr. Vijayamohanan K. Pillai, Dr. Sourav Pal, (Ex-Director NCL), Dr. Darbha Srinivas, (Head, Division Catalysis) and Dr. A. P. Singh (Former HoDs, Catalysis Division) for giving me the opportunity to perform research work in NCL, Pune and providing all necessary facilities and infrastructures. I thank Dr. Anil Kumar (Former HoDs, Physical chemistry division) for consistent help during my PhD tenure in research as well as social aspect of life. I would also like to thank Dr. T. Raja and Dr. Ekambaram Balaraman for their enthusiastic encouragement and support. Among the non-academic staffs I am thankful to Ms. Purnima

Kolhe, Ms. Deepa Puranik, Ms. Vaishali Suryawansi and others from SAC office for their help and support for various documentations during my PhD. I am also thankful to Mr. Puroshottaman and Mr. Madhu for their kind help. Special thanks to my teachers who guided me in my school and graduation because of whom I learnt a lot.

I thank my labmates Dr. Edwin S. Gnanakumar, Dr. Sadhu Kolekar, Dr. Ravi Dr. Ashwin A. Melvin, Dr. Anand, Dr. Sheetal, Dr. Naveen Sathu, Dr. Rajambal, Dr. Sanjay Negi, Dr. Sivaranjini, Dr. K. S. Thushara. Dr. Kanak Roy, Dr. Naresh Nalajala, Mr. kshirodra patra, Mr. P. Devaraji, Mr. Manoj K. Ghosalya, Mr. Prabhakar Reddy, Mr. Madhusudan, Mr. Jino, Mr. Sreejith, Ms. Pradnya Bharad, Ms. Bela Bhuskute, Ms. Ruchi Jain, Ms. Kavya, Ms. Geethu, Ms. Femi Thomas, Ms. Swati Yadav, Ms. Shilpa Khandelwal, Ms. Manisha Tripathi for their help. Especially I am very thankful to my roommate Mr. Asis K. Jana and closest friend Mr. Anil Nagaraj, Mr. Manoj Sharma and Mr. Rajendra Prasad Meena who encouraged and supported me in every stages of my research career. I am grateful to Mr. Puneet Khandelwal for generously helping me in doing AFM analysis of my samples. Sincere thanks to all hostelites of Golden Jublee hostel that have spent time along with me in various voluntary activities and also for their constant support and help. I am very much thankful to Dr. Sadhu K. Kolekar and Mr. Prabhakar Reddy for their consistent help during installation of Molecular beam instrument and vacuum FT-IR instrument. I thank B.Sc. Project student Ms. Shilpa Khandelwal for her help in various project.

My heartfelt thanks and appreciation to my parents for their unending support and sacrifices they have made in raising me to this level. I would also specially thank my wife 'Rama Dubey' for her love and care that she had showered upon me in each and every moment of life. I want to acknowledge my brother ' Mr. Rishabh Dubey' and sisters 'Ms. Alka Tiwari, Ms. Abhilasha Pandey and Ms. Nidhi Mishra' for their love and care.

Final respects and thanks to "God Almighty" for his enormous love and blessings.

Anjani Dubey

List of Abbreviations

XPS	X-ray Photoelectron Spectroscopy
UHV	Ultra High Vacuum
FWHM	Full width half maxima
QMS	Quadrupole Mass Spectrometer
OD	Outer Diameter
MBI	Molecular Beam Instrument
PES	Photoelectron Spectroscopy
RT	Room Temperature
TWC	Three way Catalytic Converter
RDS	Rate Determining State
SS	Steady State
TS	Transition State
TPD	Temperature Programmed Desorption
XRD	X-Ray diffraction
TEM	Transmission Electron Spectroscopy
SEM	Scanning Electron Spectroscopy
OSC	Oxygen Storage Capacity
BE	Binding Energy
IRAS	Infrared Reflection Absorption Spectroscopy
L	Langmuir
ML	Mono Layer
SIMS	Secondary Ion Mass Spectrometry

List of Symbols

Kn	Knudsen Number
s	Sticking Coefficient
k_B	Boltzman Constant
R_{max}	Reaction rate at maximum
λ_{gas}	Mean free path of gas molecule
λe	Mean free path of electron
θ_O	Surface oxygen coverage
$\theta_{O\text{-}sub}$	Subsurface oxygen coverage
R_{O2}	Rate of O_2 decomposition
R_{H2O}	Rate of formation of H_2O
F	Flux
T	Temperature in Kelvin
O_v	Oxygen vacancy
E_a	Activation Energy

Contents

Abstract

Reaction undergoing in real-world catalysis differs from the ideal reaction happening on single crystal in ultra high vacuum condition (UHV). So there is a "disconnect' between these two extremes regarding nature of material used as well as the surface exposed to reactants, it is known as material gap. In this thesis an attempt has been made to bridge the material gap that exists between ideal single crystals and real world powder nanocatalyst employed in surface science and heterogeneous catalysis, respectively. We have made $Ce_{1-x}Zr_xO_2$ (x = 0-1) (CZ) and metal ion i.e. Mn^{3+}, $Cu^{1+/2+}$, Ti^{4+} etc. doped CZ thin films with uniform thickness (~40 nm) and smooth surface characteristics. Uniform thickness and surface smoothness of the films over a large area will help us to study the reaction in single collision conditions in scattering environment. The aim of this work is to bring the properties of single crystal i.e. surface roughness and real world catalyst i.e. porosity, diffusion into one catalyst, thus reaching close to bridging the material gap. Molecular beam (MB) studies of O_2 adsorption and methane oxidation on CZ surfaces and metal ion doped CZ surface reveals the oxygen storage capacity (OSC), and sticking coefficient and partial and selective oxidation of methane increases with increase in temperature of the reaction. Porous nature of thin film enhances O_2 adsorption and OSC, predominantly due to O-diffusion and redox nature. In this way we can know the kinetics of reaction and also study the factors which enhance the rate of reaction by correlating the reaction at two different extremes. In this way by bridging the material gap we can address various important issues about reactions which are important industrially as well as socially to human life. By bridging the material gap between these two extremes help us to understand various unanswered questions. More studies about the kinetics of elementary reaction has been done in molecular beam instrument (MBI) and addressed in detail in respective chapters.

Chapter 1

This chapter deals with brief introduction about heterogeneous catalysis and surface science. This chapter explains about the material gap briefly which exists between surface science and heterogeneous catalysis. It explains why we have chosen ceria and ceria based solid solution for our study; OSC of ceria makes it helpful to catalyze various oxidation reactions. This chapter also gives brief introduction about C-H activation of methane and why it is difficult to catalyze the reaction at lower temperature.

Chapter 2

This chapter discusses in detail about the molecular beam instrument (MBI) and preparation procedure of catalyst under studies i.e. CZ and metal ion doped CZ thin film. This chapter also discusses the principle and procedure about various instruments which are employed in study during Ph.D. tenure. This chapter also discusses about methods which are used in calculation for various studies i.e. it discusses in details about calculation of various surface science parameter like sticking coefficient, coverage, order of reaction etc.

Chapter 3A

This chapter introduces the concept of bridging the material gap that exists between real world catalysis and surface science, with an overview of the factors that guide towards bridging the material gap. We have prepared CZ thin film by simple wet chemical method which is known as Sol-gel spin coating method. The surface roughness of thin film is in nano-regime i.e. ~ 5 to 30 nm resembling to that of single crystal and it is porous in nature which resembles to that of powder catalyst, thus we are able to bridge the material gap. We have done CO oxidation on powder CZ catalyst and found that ce-rich content material show better CO oxidation reaction which increases with increase in reaction temperature. MBI study of O_2 adsorption on CZ thin film also reveals that O_2 adsorption increases with an increase of cerium content of thin film as well as with increase in temperature. In this way we found one to one correlation between CO oxidation on powder catalyst and O_2 adsorption on CZ thin film. This confirms that we have reached close to bridge the material gap between these two extremes.

Chapter 3B

This chapter deals with molecular beam study of selective oxidation of methane on CZ thin film. As in previous chapter we observed that Ce-rich content thin film shows more OSC which increases with increase in temperature, thus increase redox properties of CZ thin film. Enhancement in redox property of CZ thin film and single collision condition in MBI help to selectively oxidize methane of HCHO. It is observed that Ce-rich content thin film shows selective oxidation of methane i.e. $HCHO+CO_2+H_2O$ and Zr-rich content thin film shows total oxidation of methane i.e. CO_2+H_2O.

Chapter 4

This chapter deals with partial oxidation of methane on manganese doped CZ thin film i.e .MCZ. MCZ thin film is formed by sol-gel spin coating method. Molecular beam study of O_2 adsorption shows that rate of O_2 adsorption increases with increase in manganese content of thin film as well as with increase in temperature. Partial oxidation of methane is done on

MCZ thin film and observed that increase in manganese content of thin film increases rate of reaction i.e. $Mn_{0.15}Ce_{0.8}Zr_{0.05}O_2$ thin film is best for partial oxidation of methane. C-H activation takes place at lower temperature i.e. 650 K on $Mn_{0.15}Ce_{0.8}Zr_{0.05}O_2$ thin film. Rate of reaction increases with increase in reaction temperature those results to increase in syngas production. XPS analysis of spent catalyst reveals that surface of MCZ thin film is completely reduced, thus confirming that redox condition is favorable for the reaction to takes place.

Chapter 5

This chapter deals with *insitu* study of CO oxidation on thin film of spinel cobalt oxide. We have prepared thin film of Co_3O_4 on Co metal foil *insitu* in molecular beam instrument (MBI). We have oxidized few layers of Co into Co_3O_4 which is confirmed by XRD and Raman spectroscopy. We have studied CO oxidation reaction by varying $CO:O_2$ ratio and observed that 1:3 ratio is an optimum condition for the CO oxidation reaction. We have observed low temperature CO oxidation reaction on Co_3O_4 irrespective of presence of desired morphology on surface of catalyst. We have also studied the effect of temperature on rate of reaction and we observed that increasing temperature has a little effect on rate of reaction. We have also studied the effect of presence of moisture in gaseous mixture and observed that rate of reaction in retarded by the presence of moisture in gaseous feedstock of the reaction.

List of publications

1. Ruchi Jain, **Anjani Dubey**, Manoj K. Ghosalya and C. S. Gopinath. Gas solid interaction of H_2-$Ce_{0.95}Zr_{0.05}O_2$: new insights into surface participation in heterogeneous catalysis. *Catal. Sci. Technol.*, **2016**, 6, 1746-1756.
2. A**njani Dubey**, Sadhu K. Kolekar, Edwin S. Gnanakumar, Kanak Roy, C. P. Vinod and C. S. Gopinath. Porous thin films towards bridging the material gap in heterogeneous catalysis. *Catal. Struc. React.*, **2016**, DOI 10.1080/2055074X.2015.1133269.
3. **Anjani Dubey**, Sadhu K. Kolekar and C. S. Gopinath. C-H activation of methane to syngas on $Mn_xCe_{1-x-y}Zr_yO_2$: A molecular beam study. *ChemCatChem*, **2016**, DOI: 10.1002/cctc.201600365.
4. **Anjani Dubey**, Sadhu K. Kolekar and C. S. Gopinath. C-H activation of methane to formaldehyde on $Ce_{1-x}Zr_yO_2$ thin films. (Submitted to *ChemCatChem*)
5. Sadhu K. Kolekar, **Anjani Dubey,** Kalyani Date, Suwarna datar and C. S. Gopinath. Kelvin probe imaging and molecular beam investigations on $Ce_{1-x}Zr_xO_2$ thin films: A potential combination to explore physical and catalysis aspects of material surfaces. (Submitted to *Analytical Chemistry*)
6. **Anjani Dubey**, Kasal P. Reddy and C. S. Gopinath. In-situ preparation and study of spinel Co_3O_4 for CO oxidation on Co metal foil: A molecular beam APPES study. (Manuscript to be submitted)
7. **Anjani Dubey**, Sanjay Singh Negi and C. S. Gopinath. Morphology and Electronic Structure Dependent Photocatalytic Water Splitting of $Ce_{0.9}Ti_{0.1}O_2$ Solid Solution. (Manuscript to be submitted)
8. **Anjani Dubey**, Sadhu K. Kolekar and C. S. Gopinath. Partial oxidation of methane to Formaldehyde and syngas on $Cu_xCe_{1-x-y}Zr_yO_2$ thin film: A molecular beam study. (Manuscript under preparation)
9. **Anjani Dubey,** Dama Srikant, C. V. V. Satyanarayana and C. S. Gopinath. C-H activation of methane to syngas on $Mn_xCe_{1-x-y}Zr_yO_2$ powder catalyst simulating condition of low contact time. (Manuscript under preparation.)
10. Edwin S. Gnanakumar, **Anjani Dubey**, Sreejith P. Nandan and C. S. Gopinath. CO oxidation on solid solution of ceria-cobalt mixed oxide having different morphology. (Manuscript under preparation)

Chapter 1 -Introduction

1.1 Heterogeneous catalysis

Catalyst is a substance which alters the rate of reaction by altering activation energy of the reaction pathway. It is classified into two branches i.e. homogeneous catalysis and heterogeneous catalysis depending on the phase of reaction. Heterogeneous catalysis is more advantageous over homogeneous catalysis to industrial catalysis, because of its easy separation from the reactants. Catalyst plays a vital role not only in the chemical industry but in a simple and complex form to all living beings. Heterogeneous catalysis is the back bone of industrial catalysis; it occurs on the surfaces/interfaces of the catalyst.[1-3] This phenomenon is most probable on surfaces and interfaces because of its unsaturation due to its low coordination of atom; so to minimize the surface energy as well as surface tension it attracts foreign entity from the immediate environment. The heterogeneous catalysis begins and started to flourish in early 19th century. This field has fetched Noble prize for Fritz Haber in 1918 and Carl Bosch in 1931, Irving Langmuir in 1932 and few other distinguished scientists. More than 80 % of the chemicals are produced through heterogeneous catalysis which plays an important role in production of manmade materials and medicines. Advancement in heterogeneous catalysis leads to industrial revolution,[4] which brings a remarkable synthesis of various chemicals like synthesis of ammonia (Haber-Bosch process), synthesis of nitric acid (Ostwald process), olefin polymerization (Ziegler-Natta polymerization) and various other industrial processes.[5]

Though these discoveries are fruitful but also lead to some pollution to the environment. To overcome these hazardous issues catalysis again plays an important role to discover a new path of sustainable green chemistry. Generally, industrial catalysis occurs under drastic condition like high temperature and high pressure; due to this mechanistic and kinetic aspect of the reaction are not well explored. The factors which enhance the rate of reaction in heterogeneous catalysis are not understood well. This disconnects hampers the further development of catalysts towards better activity/selectivity. Nowadays advanced studies have been carried out to understand the kinetic and mechanistic study of the reaction in surface science through ambient pressure x-ray photoelectron spectroscopy (APXPS), Molecular beam study, IR integrated with surface science instruments.

1.2 Surface science

Surface science is a branch of heterogeneous catalysis which deals only with few atomic layer of the surface for the reaction to happen. It is generally studied under ultra high vacuum (UHV) condition ($p < 10^{-8}$ torr). Surface science started growing in mid 20^{th} century and flourished as an interdisciplinary science. The surface science field fetched Noble prize in 2007 for the study of chemical processes on solid surfaces by Gerhard Ertl. Generally UHV is an essential requirement for most of the surface science experiment. The UHV condition is required to prepare atomically clean surface for a longer time to study the kinetics of the reaction using electron/ions/photons based in-situ techniques. UHV condition prevents energy and momentum loss of probe atoms/molecule/electrons/ions from gas phase scattering. As surface is unsaturated due to which it attracts foreign atoms/molecules, which adsorb on the surface of the catalyst. Adsorption on the surface is classified into two depending on adsorption strength, namely, a) physisorption – it's a weak bond or simply Vander Waals interaction, and b) chemisorption (strong bond). With increase in temperature of reaction physisorbed moiety will desorb, while chemisorbed moiety will dissociate/diffuse depending on the reaction condition; that leads to formation of new species which desorbs as a product.

Generally real world catalysis happens at ambient pressure or at high pressure and high temperature. Due to porous nature of real-world catalyst it is difficult to analyze it by surface science method, which complicates the kinetic analysis. Here comes the role of surface science in heterogeneous catalysis to answer such questions? However, the complexity of the real-world catalyst makes it difficult to understand the kinetic and mechanistic aspect of the reaction in heterogeneous catalysis. Hence traditional surface science relied on catalysis aspects measurements on ideal systems, such as single crystal surface, under ideal conditions like high vacuum and controlled interaction with gas-phase species at relevant temperatures. However, there is a vast difference in the nature of real-world catalysts and measurements conditions, compared to conventional surface science measurements on ideal single crystals. This gap is known to be the material gap in surface science and catalysis. In any case, there is a prior need for design of new catalyst which gives maximum yield and selectivity for a given reaction. It is difficult to understand the factors, which lead to maximum yield and selectivity of the reaction at microscopic level from surface science measurements. However, it is also imperative to perform surface science measurements on real-world catalysts in a suitable form to get more details. Will the surface science really answer these questions/aspects? The answer is yes, with significant difficulties;

the research is going on to understand reaction at microscopic level by the bridging the material gap that exist between ideal single crystal and real world catalyst, as well as the pressure gap between these two extremes.

1.2.1 Material gap

Surface science of catalysts is the study of elementary reactions from adsorption of reactants, dissociation and possible diffusion followed by product formation and desorption. Generally these studies are conducted on single crystal surfaces under ideal conditions, while the real world heterogeneous catalysis is performed on powder material which is porous in nature and exhibit rough surfaces. While single crystal material surfaces is very well-defined, it is not the case with powder catalysts, as the real-world catalysts contain many different components, such as support, promoters, spacers. Further, catalytic activity depends on the particle size, morphology, even synthesis method employed, metal-support interaction etc. Role of each and every component of real-world catalyst is not defined, but in general it was assumed that they lead to better activity. In the absence of role of different components, often the catalysis aspects derived from surface science methods on single crystals and powder catalysts does not correlate well. The simplest possible single crystal employed in surface science and highly complex real-world catalysts employed in industrial catalysis vary to a large extent. There is a "disconnect" between these two extremes with respect to nature of the materials that leads to a material gap.[6-8] Single collision, adsorption, scattering of molecules is the prominent phenomenon on surface science studies on single crystal while bulk diffusion, multiple adsorption is the prominent phenomenon in industrial heterogeneous catalysis. Correlation of the result obtained from the Surface science study under UHV condition to industrial catalysis is a big challenge. Prevalent condition in UHV are drastically different from industrial catalysis (pressure gap), while heterogeneous catalyst are different from single crystal (Material gap). Shell is the only company which utilizes single crystal study to heterogeneous catalysis for Fischer-Tropsch synthesis on cobalt[9-13] as well as epoxidation of ethylene on silver.[14,15] So to bridge the material gap we have designed such catalyst in form of thin film of Ceria-Zirconia (CZ) as well as metal ion doped CZ solid solution which exhibit significant qualities of single crystal as well as that of real world catalyst.[15] Thin film has surface roughness comparable to that of single crystal, which is also porous in nature thus having the characteristic feature of real world catalyst; in this way we are able to bridge the material gap that exist between these two extremes. Present thesis predominantly attempted to address the material gap and our efforts may be considered as the baby-step in addressing the material gap. Many aspects, such as diffusion, needs to be

addressed in detail, which will be attempted hopefully by our group as well as by other groups.

Fig. 1.1 High surface quality thin films with porous characteristics bridge the material gap. These types of thin films could be useful to study the fundamental aspects such as, adsorption, elementary reactions in a surface science setup as well as can be employed to investigate real-world catalysis aspects, such as diffusion, heat/mass transfer aspects due to porosity aspects available in it.

1.2.2 Present status of material gap

In heterogeneous catalysis it is very difficult to understand the structure-activity relationship because of the complex nature of the catalyst. Surface and bulk material differs dynamically because of its geometric structure, compositions and local electronic environment around the

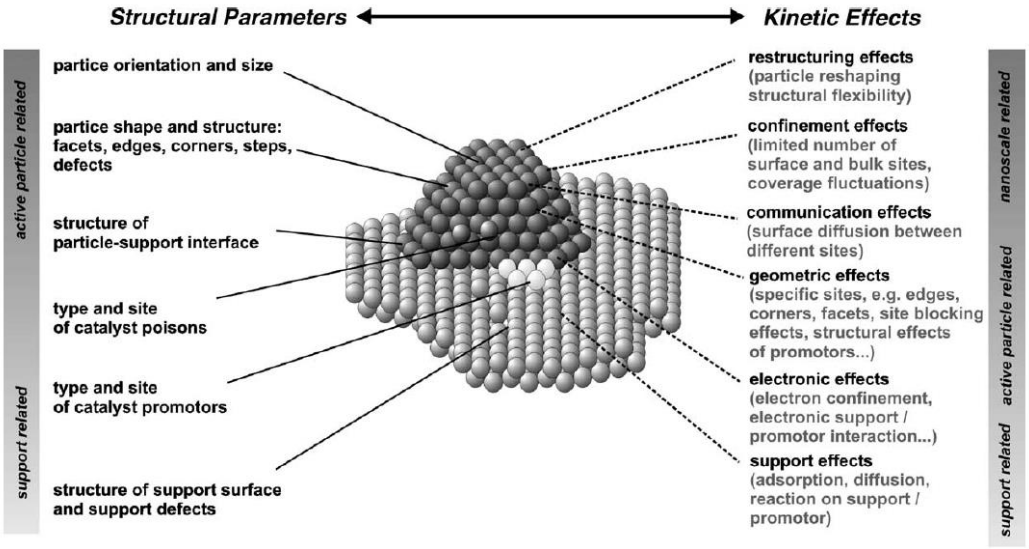

Fig. 1.2 Structural parameters and kinetic effects on supported metal catalyst. (Reproduced from Ref. 16 with permission from Elsevier publishing group)

active centre. Thus all factors needs to be analyzed separately like surface, support, and promoters and then coupled in a systematic and gradually complexing manner to move towards designing better catalyst in a rational manner. In surface science single crystal was

used for study which differs from the actual powder catalyst of same material, which is known as 'material gap'. So to bridge this material which exists between surface science and heterogeneous catalysis, model catalyst has been used. The idea behind this is to have surface properties of single crystal as well as powder catalyst which are easily analyzed by surface science technique. The factors[16] which lead to material gap have been summarized in Fig. 1.2.

To bridge the material gap several efforts has been made in the past. Freund et. al[17] has synthesized model catalyst where they deposited metal nanoparticles and also has applied a variety of experimental techniques which is helpful in bridging the material gap which exists between surface science and catalysis. They have catalyzed methanol dehydrogenation and ethane hydrogenation in UHV as well as in ambient conditions. It has been concluded that there is good correlation between results obtained on model system and real-world catalysts towards understanding of catalysis. Generally industrial catalysts are prepared such that active part of the catalyst (usually a metal or metal oxide) is supported on high surface area material; this is very complex in nature and not suitable for surface science study for several reasons, including the inability to atomically clean the surface, rough surface nature etc. To simulate the support effect, it was prepared from original elements; for example, flat alumina surface can be prepared by controlled oxidation of aluminium surface and metal particles can be deposited on such flat surfaces. These are known as flat model catalysts, which can be useful in surface science techniques. Gunter et. al[18] has given a concept of surface science approach to flat model supported catalyst to bridge the material gap which is shown in Fig. 1.3. Here they have discussed about the flat model system which act as a replacement of porous support for the study in UHV with surface science techniques.

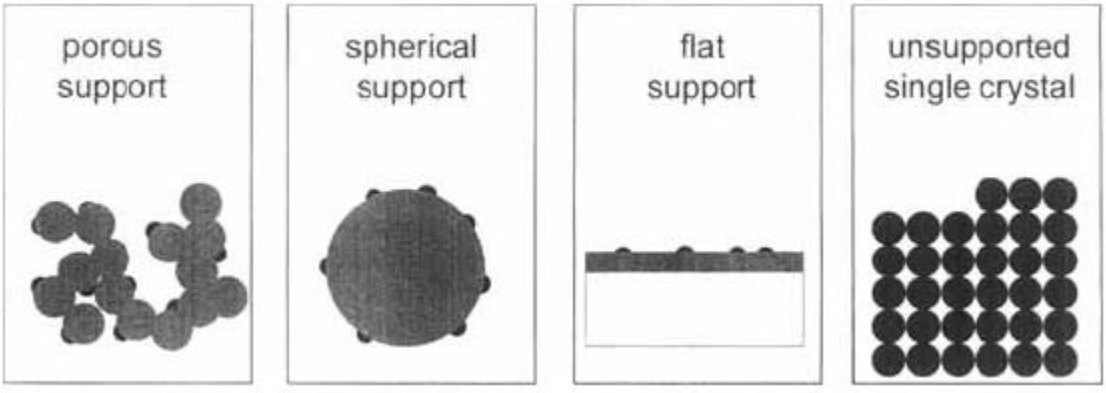

Fig. 1.3 Several possibilities for modelling catalysts exist between the industrial system with a high surface area, porous support (left) and the surface of a single crystal (right.) (Reproduced from Ref. 18 with permission from Taylor and Francis group)

Spin coating is the best possible technique to form uniform thin films and Kuipers[19] was the first to identify the use of spin coating to form model supported catalyst. Van Hardeveld et. al.[20] compared the thickness data (atomic layers) obtained from Rutherford backscattering spectroscopy to the predicted/expected loading amount of material by spin coating technique and based on simple model calculation , which is shown in Fig. 1.4. It was found that only 10 % deviation in calculated loading values, suggesting spin-coat models may lead to probably more accurate predictions.

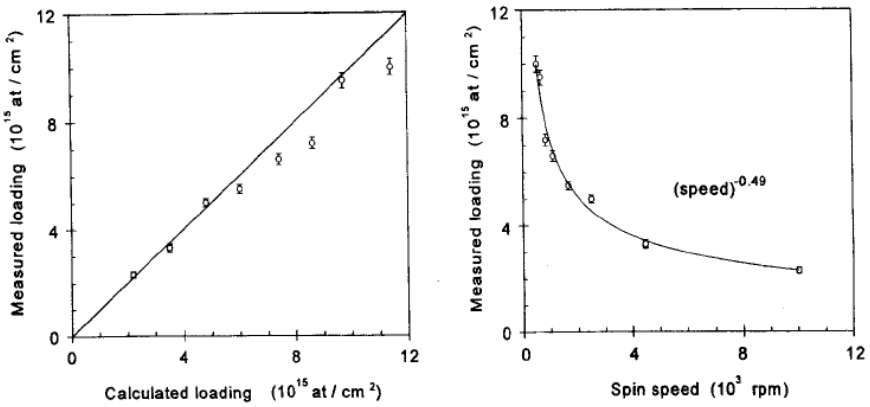

Fig. 1.4 Quantification of Mo loading on a silicon wafer obtained by spin coating with a 0.62 wt % MoO_2Cl_2 solution in ethanol. The measured (Rutherford backscattering) loading is compared to the predicted loading (a), and depends on the spinning frequency as shown in (b) (for details see Ref. 20.) (Reproduced from Ref. 18 with permission from Taylor and Francis group)

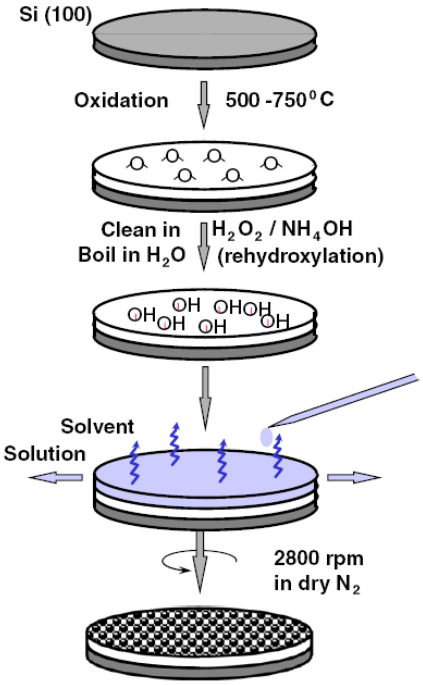

Fig. 1.5 Preparation of a supported model catalyst by spin coating impregnation starting from a single crystal silicon wafer. (Reproduced from Ref. 21 with permission from Elsevier publishing group)

Thune et. al.[21] proposed a concept of planar models of supported catalyst and found that supported model catalyst prepared by spin coating followed by impregnation method can be well suited to be evaluated by surface science technique (Fig. 1.5). In this way they prepare real world catalyst in form of thin film, thus minimizing the material gap that exists between surface science and heterogeneous catalysis.

1.2.3 Pressure Gap

Along with "Material Gap" "Pressure Gap" also exist between surface science and heterogeneous catalysis. Bridging of the pressure gap is generally an extension of pressure regime from UHV condition unto actual reaction conditions or at least 1 bar. With change in gas pressure, free energy of gas will change; so it is very difficult to correlate the results obtained from UHV condition to real world high pressure reaction (1 to 100 bars). Pressure gap can be minimized in two possible ways one is the attachment of the high pressure cell along with UHV system. In such type of system the formation and characterization has been done in UHV condition while the catalytic reaction has been performed close to real-world catalytic condition in high pressure cell. The second method to minimize the pressure gap is the study the reaction *in-situ* at elevated pressure; this method appears to be simple but technique is complicated. These *in-situ* studied can be used to study the structure sensitivity of catalyst as well as the effect of the promoters/inhibitors on rate of reaction. This type of technique has been developed and implemented to study high pressure reaction, eg. Infrared-visible sum frequency generation vibrational spectroscopy (SFG)[22-24], polarization modulation infrared absorption reflection spectroscopy (PM-IRAS)[25,26], near-ambient pressure photoelectron spectroscopy (NAPPES)[27,28], and insitu scanning tunneling microscopy (STM)[29,30]. We have studied all elementary reaction in Molecular Beam Instrument (MBI). In this instrument pressure on the catalyst is of the order of 10^{-6} to 10^{-4} mbar while the chamber pressure is of 10^{-8} mbar during reaction condition; thus minimizing the pressure gap.

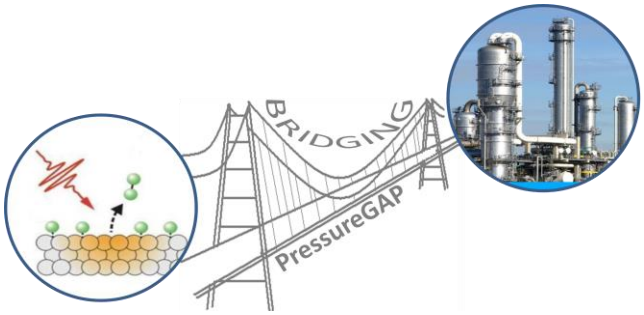

Fig. 1.6 Graphical representation of "bridging of Pressure Gap" that exist between ideal surface science study and heterogeneous industrial catalysis.

1.3 Ceria

Ceria is the versatile and most studied material next to silica in catalysis. It is a vital catalyst for various oxidation reactions, because of its redox properties and its high oxygen storage capacity (OSC). It is well known for the removal of post combustion pollutant and organic materials from waste water.[31,32] Though pure ceria has very little application at high temperature because it agglomerates, thus loses its oxygen mobility i.e. ceria has low thermal stability.[33,36] Ceria is well known for OSC due to which it finds an immense application in three-way catalytic convertor.[37] Ceria, because of its redox properties, is used as a self-cleaning agent in ovens where it oxidizes the hydrocarbons into CO_2 and H_2O.[38] Ceria also finds its application in UV absorption as well as solid oxide fuel cells (SOFC).[39] Ceria based catalyst finds its application in various field like Fluid-cracking catalyst in refineries, ethylbenzene dehydrogenation catalyst in styrene formation. Ceria is also used in low temperature CO oxidation, wet-oxidation of organic pollutant in water, water-gas shift reaction, partial oxidation of hydrocarbons, steam reforming etc.

Ceria has calcium fluoride (CaF_2) type structure with *Fm3m* space group.[40] Sun et. al.[41] have described cubic fluorite structure of ceria with its defect chemistry to nano-size effect; it is shown in Fig. 1.7 below:

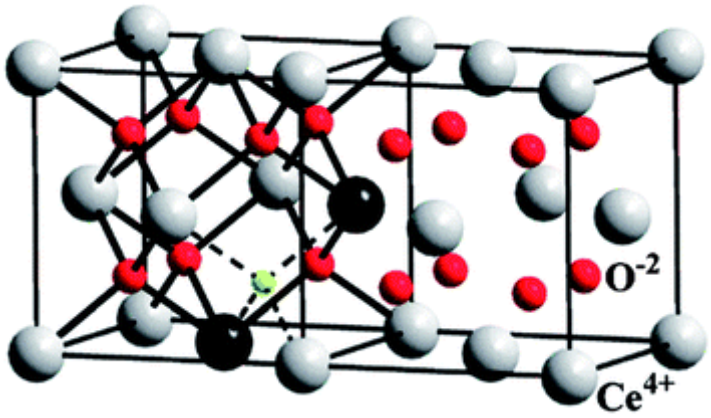

Fig. 1.7 Cubic fluorite structure of ceria as explained in reference 35. Red colour sphere is O^{2-} ion while light grey colour sphere is Ce^{4+} ion. (Reproduced from Ref. 41with permission from RSC publishing group)

Cerium being second element of rare earth series has an electronic configuration taking Xenon into consideration, as $(Xe)6s^2 5d^1 4f^1$. Since the volume of 6s and 5d orbital's are large compared to that of 4f orbital, so three $6s^2$and $5d^1$electron only participates in chemical bond formation. Due to this reason lanthanide elements generally exist in 3+ oxidation state. Ce^{3+} has an electronic configuration of $(Xe)4f^1$, and it loses f electron easily in order to acquire more stable structure of the tetravalent ion Ce^{4+}. Ceria is cubic fluorite in

structure containing four formula units per unit cell. Ce^{4+}ion are coordinated to eight O^{2-} ions and are situated at the corner of regular tetrahedron, while each O^{2-} ion is coordinated to four Ce^{4+} ions. The edge length of CeO_2 is approximately 0.5411 nm, but its melting point is not well known due to its volatile nature at high temperatures. However, Rouanet[42] reports a tentative value of melting point to be around 2480 ^oC. At higher temperature and at low oxygen partial pressure ceria gets reduced into complex stoichiometric oxide, of which maximum reduced state of ceria is Ce_2O_3. With increase in dis-orderness in structure of ceria or with change in morphology of ceria, brings defect in cubic fluorite structure of ceria. This defect can be minimized with oxygen mobility in order to maintain the stability of structure. This usual property of ceria can be useful in various applications which has been discussed above and shown below in a flow chart in Fig. 1.8.

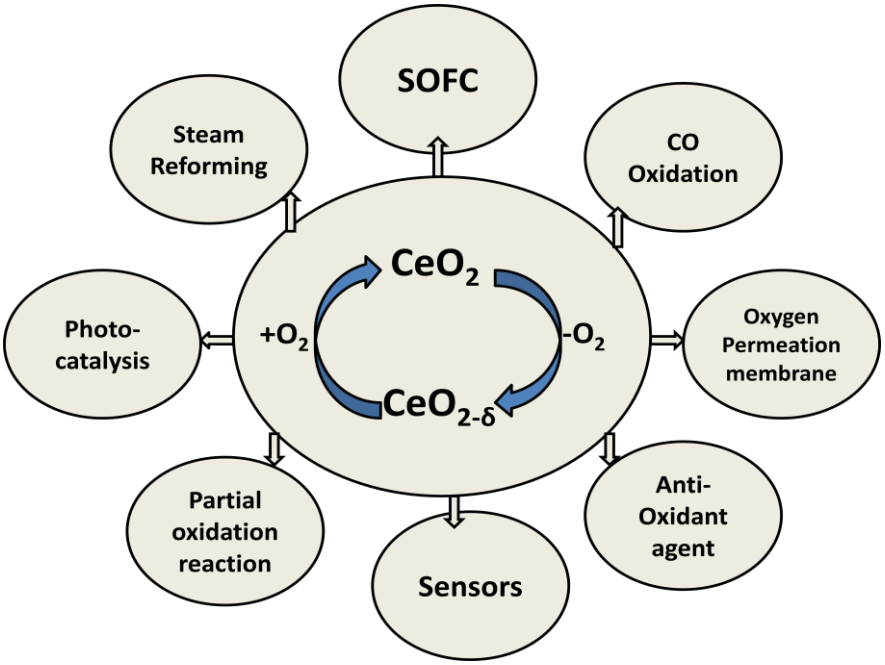

Fig. 1.8 Various applications of ceria in flow chart diagram.

1.3.1 Doping of metal ion into ceria lattice

Ceria is a very good oxidation catalyst because of its high OSC; however, its thermal stability is very low at high temperatures. At high temperatures ceria particles agglomerates which reduces the surface area, oxygen mobility property of ceria, due to which there is a reduction in its catalytic property at higher temperature. To overcome the problem of thermal stability and in order to increase the oxygen mobility, ceria has to be doped with metal ions, i.e. $Mn^{2+/3+}$, Zr^{4+}, Hf^{4+}, $Co^{2+/4+}$ etc. Doping of the metal ion into ceria lattice not only increases the thermal stability but also enhances its redox properties. In this context many studies has been made for the last three decades on doping on zirconium ion into ceria lattice.[43-45]

Incorporation of zirconium ion leads to more concentration of defects which enhances the O^{2-} ion mobility thus improving the redox behaviour of ceria.[46] Mixed ceria-zirconia oxide have been used for CO oxidation,[47] treatment of exhaust gas,[48-50] methane reforming[51] and partial oxidation of methane.[52] Ceria is renowned for oxidation catalysis and doping of manganese into its lattice attracted much attention in pollution control. This system is very useful in catalytic wet oxidation where water is used as an oxidant for the removal of hydrocarbon pollutant from the aqueous stream of reaction.[53-56] Doping of the manganese into ceria lattice will bring the light off temperature for diesel soot oxidation[57] as well as for catalytic reduction of NO_x with ammonia.[58]

Doping of the metal ion into ceria lattice enhances the redox properties of ceria. This reduction facilitates the oxygen mobility; thus enhancing OSC of ceria. Copper based ceria system has a promising effect on selective oxidation of CO in presence of H_2.[59-63] It facilitates low temperature CO oxidation with high selectivity in presence of hydrogen. This happens because of strong redox property of the combined system compared to ceria.[64] The reduction of ceria induces oxygen vacancies which accelerate oxidation reaction; the equation for reduction of ceria is shown below:

$$CeO_2 \longrightarrow CeO_{2-\delta} + \delta/2 O_2 \qquad (1.1)$$

$$O^{2-} \longleftrightarrow \tfrac{1}{2} O_2 + V_o + 2e^- \qquad (1.2)$$

In eq. 1.2 V_o is the oxygen vacancy which is created when it leaves the ceria lattice reducing Ce^{4+} into Ce^{3+} ion. This oxygen vacancy has high mobility to diffuse to surface and hence actively participates in catalyzing various oxidation reactions. Due to this oxygen mobility, ceria is usually known for its oxygen storage capacity.

1.3.2 Oxygen storage capacity (OSC)

OSC is the amount of oxygen that can be released during net reducing condition as well as the amount of oxygen uptake during net oxidizing condition.[65,66] Generally OSC is measured by temperature programmed desorption (TPD). The fluctuation of valence state between Ce^{4+}/Ce^{3+} is the reason for the oxygen mobility in and out of the ceria lattice; this is associated with oxygen vacancy formation which is responsible for the high OSC of ceria.[67]Since ceria agglomerates at high temperatures, its surface area decreases. Decrease in surface area of pure ceria decreases oxygen mobility which decreases OSC at higher temperature. When metal ion is doped into ceria lattice, reducibility of ceria increases with formation of solid solution.

When zirconium ion is added into cerium lattice it forms a solid solution in stoichiometric ratio with formula $Ce_{1-x}Zr_xO_2$. Metal-ion doping in ceria lattice can be easily

observed by x-ray diffraction (XRD). XRD lines get broadens which signifies smaller crystallite size with high surface area of $Ce_{1-x}Zr_xO_2$ solid solution which reflects its high OSC. Cubic structure associated with pure ceria changes gradually to fluorite with increased doping level. The most important use of $Ce_{1-x}Zr_xO_2$ solid solution is its enhanced OSC which is used in the storage and release of oxygen by lowering the fluctuation of air to fuel ratio during transient state.[68] Surface area is not the only property which decides the OSC of ceria; it is the active interstitial oxygen ions that provide necessary oxygen mobility is crucial in the functioning of ceria as a catalyst or catalyst support.[69] Crystallite size of ceria plays a crucial role in determining the OSC of ceria. It has been found from experimental studies that OSC of polycrystalline ceria confirms that mobility of oxygen depends on the crystallite size. Several studies also confirm that oxygen vacancy decides the OSC of ceria. It is also reported that at high temperatures OSC of smaller nanoparticle decreases; decrease in OSC correlates well with increasing concentration of Ce^{3+} ions.[70] Ceria at higher temperature in oxygen environment replenishes its oxygen vacancy with gas-phase molecular oxygen. This fully supports the Mars van Krevelen mechanism at high temperature, i.e. exchange of lattice oxygen with gas-phase oxygen.

OSC of ceria is displayed mostly in the form of Ce^{4+}/Ce^{3+} redox couple. Ceria and metal ion doped ceria is well known for various oxidation reactions is because of its high OSC. Due to this property it is able to catalyze various reactions at lower temperature even in an absence of noble metal, i.e. Au, Pt, Pd etc.[71] Ceria and metal ion doped ceria being vital enough for many useful reactions because of the properties that are discussed above. So we have chosen to prepare a thin film of ceria-zirconia (CZ) and metal ion doped CZ to bridge the material gap that exist between ideal single crystal and real world catalyst.

1.4 CZ thin film to bridge the material gap

We have prepared CZ thin film with an aim to bridge the material gap that exists between ideal single crystal and real world catalyst. There is a huge disconnect between these two extremes, one like single crystal have well ordered surface, definite crystallographic facets, no diffusion of adsorbed atoms into the bulk etc. while real world powder catalyst have disordered porous structure with no defined crystallographic facets, diffusion is the prominent phenomenon etc. Single crystal has very low surface roughness of the order of less than 20 nm while the real world catalyst has very rough surfaces which are also porous in nature. The prominent phenomenon on single crystal is adsorption without diffusion where only particular plane with few atomic layer are active for catalysis. The prominent phenomenon that occurs on real world catalysis is diffusion of the reactants due to its porous nature. Since

the nature of the surface as well as the processes happening on it is very different and it is also very difficult to correlates the findings of results between these two extremes. Keeping these disconnect in mind we have planned to bring the properties of single crystal and real world catalyst in same catalyst and study various catalytic and kinetic aspect of reaction. Since ideal single crystal is used in surface science study in UHV condition, while complex nature of real world catalyst makes it difficult to explore the knowledge at molecular level. Bridging the material gap and combining it with *in-situ* technique such as MBI, NAPPES will give molecular level understanding for the reaction. We have prepared the CZ thin film by simple wet chemical method, i.e. Sol-gel spin coating method. The surface roughness of the CZ thin film is in close resemblance with that of ideal single crystal in order of 5 to 50 nm. The as prepared film is also porous in nature so it resembles to real world catalysis. In this way we are able to bring the desired properties of smooth surface quality and porous nature in thin films. We have employed this thin film in MBI to study the kinetics of the reaction as well as various parameters which influences the reaction. Fundamental adsorption and catalysis aspects inferred from these studies are expected to be useful to understand the real-world industrial catalysis as well as to model them. In other words, studies carried out on high surface quality porous thin films basically bridges the material gap divide.

1.5 C-H activation and partial oxidation of methane

Methane is an important component of natural gas and its conversion to useful products is well acknowledged by scientific community. The challenging problem in methane conversion is the energy required for C-H activation which is 439.3 kJ/mol.[72] Heterogeneous catalysis is the key for methane conversion as it get adsorbed and dissociated on surface of the catalyst.[73-75] Partial oxidation of methane with molecular oxygen and methane-rich composition generally leads to formation of syngas while in other ratio may also lead selective oxidation of methane to formaldehyde. Nowadays research is going on to catalyze partial oxidation of methane into a) syngas, b) ethylene, c) formaldehyde and d) methanol. Till date methane conversion to formaldehyde and methanol has been evaluated upto research laboratory levels, while ethylene formation has reached to industrial production. Formation of syngas has reached upto pilot plant stage.[76]

$CH_4 + ½\ O_2 \rightarrow CO + 2\ H_2$ $\Delta H^o_{298} = -36$ kJ/mol (1.3)

$CH_4 + ½\ O_2 \rightarrow ½\ C_2H_4 + H_2O$ $\Delta H^o_{298} = -185$ kJ/mol (1.4)

$CH_4 + O_2 \rightarrow HCHO + H_2O$ $\Delta H^o_{298} = -320$ kJ/mol (1.5)

$CH_4 + ½\ O_2 \rightarrow CH_3OH$ $\Delta H^o_{298} = -164$ kJ/mol (1.6)

Partial oxidation of methane to syngas and formaldehyde is very important from the fundamental as well as applied catalysis aspects, and these two reactions have been discussed in detail. Methane oxidation reaction is exothermic in nature and it occurs generally at a faster rate. It is also to be noted that methane combustion is highly exothermic and hence partial oxidation of methane is very important to convert to useful and desired products.

$CH_4+2O_2 \rightarrow CO_2+2H_2O$ $\Delta H = -803$ KJ/Mol (1.7)

Gas phase transformation is important in deciding the nature of the reaction. Due to exothermic nature of reaction heat generation is faster than heat release by process of radiation, convection and conduction. The important part of surface-gas phase reaction is the radical exchange between surface and gas.[77,78] It has been found that at low temperature formation of CO_2 and H_2O is more prominent compared to CO and H_2. As the reaction temperature increases, yield and selectivity of H_2 increases compared to that of CO.[79-81]

The first step in partial oxidation of methane is the dissociative adsorption of methane. Many *in-situ* studies have been made to study the mechanism of the reaction. These reaction studies have been made on single crystal under UHV condition to elucidate the mechanism of the reaction, i.e. MBI. The mechanistic details about partial oxidation is still not well explored, but reported studies acknowledges that the principal mechanism for partial oxidation of methane is direct dissociative chemisorption of methane i.e. loss of H-atom on adsorption with catalyst surface. Loss of H-atom is highly activated phenomenon which is dependent on vibrational as well as translational energy of impinging methane molecule.[82-84] Partial oxidation of methane proceeds via two mechanisms one is direct dissociative adsorption of methane where methane is directly converted into CO and H_2gas molecules without formation of CO_2 and H_2O molecules,[85] which are shown below:

$CH_4 \rightarrow C_s + 4H_s$ (1.8)

$C_s + O_s \rightarrow CO$ (1.9)

$H_s + H_s \rightarrow H_2$ (1.10)

and b) formation of complete oxidation product i.e. CO_2 and H_2O (Equn. 1.7) and then CO_2 and H_2O combines with CH_4 through reformation pathway to form syngas (combustion-reforming) i.e. CO and H_2.[86-91]

$CH_4 + H_2O \rightarrow CO + 3H_2$ $\Delta H = +341$ KJ/Mol (1.11)

$CH_4 + CO_2 \rightarrow 2CO + 2H_2$ $\Delta H = +247$ KJ/mol (1.12)

The mechanistic aspect of partial oxidation of methane helps us to decide thermodynamic pathway of reaction, which is shown as pictorial representation below.

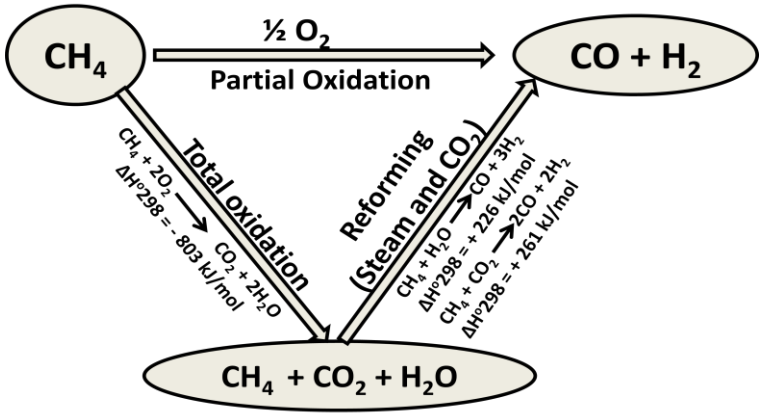

Fig. 1.9 Pictorial representation showing thermodynamic view of partial oxidation of CH_4.

Direct selective oxidation of methane to oxygenates i.e. formaldehyde; methanol etc. in a single step is a very difficult process, however very much desired. The indirect conversion of methane to formaldehyde involves three different steps, i.e. steam reforming of methane to syngas, syngas conversion to methanol and further, partial oxidation of methanol to formaldehyde. The indirect process is an energy consuming process and very costly; so direct conversion of methane to formaldehyde is definitely advantageous. Though direct conversion is energy and cost effective but, the yield and selectivity of formaldehyde is low. Since enthalpy of formation of total oxidation product from further oxidation of HCHO is more than the enthalpy of formation for selective oxidation of methane to formaldehyde; this is the reason for low yield of HCHO.

$CH_4 + O_2$ $HCHO + H_2O$ $\Delta H^o_{298} = -319$ kJ/mol (1.13)

$HCHO + O_2$ $CO_2 + H_2O$ $\Delta H^o_{298} = -571$ kJ/mol (1.14)

These reactions have been done on CZ thin film as well as metal ion doped CZ thin film. It is found that reduced cerium ion in CZ thin film is favourable condition for partial as well as selective oxidation of methane. We found that CZ thin film give selective oxidation of methane to formaldehyde at a temperature $T \geq 950$ K varying CH_4:O_2 ratio from 5:1 to 1:5. We found that with increase in temperature of reaction yield as well as selectivity of reaction increases in CH_4 rich molecular beam. On doping of the Manganese ion into CZ lattice with CH_4:O_2 = 2:1 it shows partial oxidation of methane: the product obtained is syngas. On incorporation of manganese ion into CZ lattice C-H activation temperature decreases and it occurs at temperature $T \geq 650$ K. It is also observed that, with increases in mol % of Mn ion into CZ lattice increases the rate of formation of syngas product. With increase in temperature rate of formation of syngas product increases changing surface Ce^{4+} concentration fully to Ce^{3+} concentration.

The thesis begins with an aim to bridge the material gap that exists between surface science and heterogeneous catalysis and divided into three working chapters, apart from introduction (Chap. 1) and experimental methods (Chap. 2). Uniform surface quality and homogeneous thin film of CZ was prepared by a combination of sol-gel and spin coating method (Chap. 3A). They exhibit surface properties resembles as that of single crystal while porous nature of thin film brings the characteristic property of real world catalyst; indeed brining these two extreme characteristics is the first requirement to bridge the material gap . CO oxidation on CZ powder catalyst measured in a typical heterogeneous reactor and O_2 adsorption measured on CZ thin film in MBI and the results obtained shows very good correlation. In next section of first working chapter (Chap. 3B), selective oxidation of methane to formaldehyde was evaluated on CZ thin films. We have studied selective oxidation of methane with different CH_4:O_2 ratios and studied how the rate of reaction varies. We have also studied the effect of change of temperature on selective oxidation of methane. Detailed kinetic analysis hints the oxygen vacancy associated with Ce3+ sites are responsible for HCHO production.

Chapter 4 deals with the synthesis of manganese doping into the CZ lattice and formation of a uniform solid solution thin film on Si wafer i.e. MCZ thin film. The solid solution thus formed was subjected to O_2 adsorption as well as partial oxidation of methane. The as prepared MCZ thin film is subjected to O_2 adsorption as a function of temperature. Various surface science parameters like sticking coefficient, coverage and oxygen storage capacity (OSC) has been calculated. Partial oxidation of methane was evaluated on MCZ thin film with different Mn content (2 to 15 mol %). Syngas production was observed from 700 K and above. An interesting mechanistic aspect was revealed from the MBI studies. A thorough analysis leads to a revelation of competition as well as cooperation existing among the various elementary reactions. Probably this is the first time in the literature it was revealed for such a complex reactions and we attribute this to the employing MCZ thin films and the diffusion mechanism operative in the C-H activation of methane.

In Chap. 5 spinel cobalt oxide thin film was prepared in-situ on cobalt metal foil in MBI. The formation of spinel cobalt oxide thin film is confirmed by various characterizations like XRD, Raman Spectroscopy. There is no specific (or random) morphology was observed in FE-SEM analysis. The molecular beam study of CO oxidation was carried out on Co_3O_4. CO oxidation reaction was evaluated under many relevant conditions. Low temperature CO oxidation occurs on Co_3O_4 at 275 K and also studied this reaction as a function of temperature. We have also studied the effect of moisture present in gas feedstock on rate of

CO oxidation on spinel cobalt oxide. In contrast to the literature reports on the requirement of nanorod morphology for ambient CO oxidation activity, random morphology also gives the similar results. This aspect is discussed in detail in Chap. 5.

Chapter 6 provides the conclusions and the broad outlook and future prospective available has been discussed.

1.6 References

1. Z. Ma, F. Zaera, Heterogeneous Catalysis by Metals in Encyclopedia of Inorganic Chemistry, John Wiley, **2006**.
2. M. Salmeron, R. Schlögl, *Surf. Sci. Rep.* **2008**, *63*, 169, and references therein.
3. B. Lindströma, L. J. Pettersson. *cat tech.* **2003**, 7, 130.
4. G. Ertl, H. Knozinger, J. Weitkamp, *Handbook of Heterogeneous Catalysis*, Vol. **1** Wiley-VCH, Weinheim, **1997**.
5. H. Oosterbeek, *Phys. Chem. Chem. Phys.* **2007**, *9*, 3570.
6. H. J. Freund, H. Kuhlenbeck, J. Libuda, G. Rupprechter, M. Bäumer, H. Hamann, *Top. In Catal.* **2001**, *15*, 201.
7. M. Baernsa, R. Imbihl, V.A. Kondratenko, R. Kraehnert, W. K. Offermans, R. A. van Santen, A. Scheibe, *J. Catal.* **2005**, *232*, 226.
8. J. J. C. Geerlings, M. C. Zonnevylle, C. P. M. de Groot, *Surf. Sci.* **1991**, *241(3)*, 315.
9. J. J. C. Geerlings, M. C. Zonnevylle, C. P. M. de Groot, *Catal.Lett.* **1990**, *5*, 309.
10. J. H. Wilson, C. P. M. de Groot, *J. Phys. Chem.* **1995**, *99*, 7860.
11. G. A. Beitel, A. Laskov, H. Oosterbeek, E. W. Kuipers, *J. Phys. Chem. B* **1996**, *100*, 12949.
12. G. A. Beitel, C. P. M. De Groot, H. Oosterbeek, J. H. Wilson, *J. Phys. Chem. B,* **1997**, *101*, 4035.
13. C. Backx, C. P. M. de Groot, *Surf. Sci.* **1982**, 115, 382.
14. C. Backx, C. P. M. de Groot, P. Biloen, *Appl. Surf. Sci.* **1981**, *6*, 256.
15. A. Dubey, S. K. Kolekar, E. S. Gnanakumar, K. Roy, C. P. Vinod, C. S. Gopinath, *Catal. Struc. React.* **2016**, DOI: 10.1080/2055074X.2015.1133269.
16. J. Libuda, H. J. Freund, *Surface Science Reports* **2005**, *57*, 157.
17. H. J. Freund, M. Bäumer, J. Libuda, T. Risse, G. Rupprechter, S. Shaikhutdinov, *J. Catal.* **2003**, *216*, 223.
18. P. L. J. Gunter, J. W. H. Niemantsverdriet, F. H. Ribeiro, G. A. Somorjai, *Catal. Rev. – Sci. Eng.* **1997**, *39(1&2)*, 77.
19. E. W. Kuipers, C. Laszlo, and W. Wieldraaijer, *Catal. Lett.* **1993**, *17*, 71.

20. R. M. van Hardeveld, P. L. J. Gunter, L. J. V. IJzendoorn, W. Wieldraaijer, E. W. Kuipers, and J. W. Niemantsverdriet, *Appl. Surf: Sci.* **1995**, *84*, 339.
21. P. C. Thune, J. W. Niemantsverdriet, *Surface Science* **2009**, *603*, 1756.
22. J. Miragliotta, R. S. Polizotti, P. Rabinowitz, S. D. Cameron, R. B. Hall, *Appl.Phys.A* 1990, *51*, 221.
23. X. Su, P. S. Cremer, Y. R. Shen, G. A. Somorjai, *J. Am. Chem. Soc.* **1997**, *119*, 3994.
24. T. Dellwig, G. Rupprechter, H. Unterhalt, H. J. Freund, *Phys. Rev. Lett.* **2000**, *85*, 776.
25. G. A. Beitel, A. Laskov, H. Oosterbeek, E. W. Kuipers, *J. Phys. Chem*. **1996**, *100*, 12494.
26. E. Ozensoy, D. C. Meier, D. W.Goodman,*J. Phys. Chem. B***2002**,106*, 9367-9371.
27. H. Bluhm, M. Hävecker, A. Knop-Gericke, E. Kleimenov, R.Schlögl, *J. Phys. Chem. B* **2004**, *108*, 14340.
28. K. Roy, C. P. Vinod, C. S. Gopinath, *J. Phys. Chem. C* **2013**, *117*, 4717.
29. G. A. Somorjai, *Appl. Surf. Sci.* **1997**, *121*, 1.
30. A. Kolmakov, D. W. Goodman, *Surf. Sci.* **2001**, 490, L597.
31. P. Fornasiero, G. Balducci, R. Di Monte, J. Kaspar, V. Sergo, G. Gubitosa, A. Ferrero, M. Graziani, *J. Catal.* **1996**, *164*, 173.
32. A. Trovarelli, C. De Leitenburg, M. Boaro, R. Dolcetti, *Catal. Today* **1999**, *50*, 353.
33. A. Laachir, V. Perrichon, A. Badri, J. Lamotte, E. Catherine, J. C. Lavalley, J. El Fallah, L. Hilarie, F. Leonormand, E. Quemere, G. N. Sauvion, O. Touret, *J. Chem. Soc., Faraday Trans.* **1991**, *187*, 1601.
34. R. S. Mikhail, R. M. Gabr, R. B. Fahim, *J. Appl. Chem.* **1970**, *20*, 222.
35. J. E. Kubsh, J. S. Rieck, N. D. Spencer, *Stud. Surf. Sci. Catal.* **1994**, 71.
36. M. Pijolat, M. Prin, M. Soustelle, O. Touret, *J. Chem. Phys.* **1994**, *91*, 37.
37. H. ling, Y. Xiu-Min, L. Guo-Liang, X. Nan, *Energy Procedia* **2012**, *17*, 547.
38. J. Verhelst, D. Decroupet, D. D. Vos, *Catal. Sci. Technol.* **2013**, *3*, 1579.
39. T. Masui, K. Fujiwara, K. Machida, G. Adachi, *Chem. Mater*. **1997**, *9*, 2197.
40. M. K. Devaraju, X. Liu, K. Yusuke, S. Yin, T. Sato, *Nanotechnol.* **2009**, *20*, 1.
41. C. Sun, H. Li, L. Chen, *Energy Environ. Sci.* **2012**, *5*, 8475.
42. A. Rouanet, *Thesis, Montpellier, France,* **1970.**
43. M. Thammachart, V. Meeyo, T. Risksomboon, S. Osuwann, *Catal. Today* **2001**, *68*, 53.
44. A. Cabana, J. A. Darr, E. Lester, M. Poliakoff, *J. Mater.Chem.* **2001**, *11*, 561.
45. E. Rohart, O. Larcher, C. Hedouin, M. Allain, P. Macaudiere, *SAE Int. Paper* **2001**, *1*, 1274.

46. P. Fornasiero, R. di Monte, G. Rao, J. Kaspar, S. Meriani, A. Trovarelli, J. Graziani, *J. Catal.* **1995**, *151*, 168.
47. P. Bharali, P. Saikia, L.Katta, B. M. Reddy, *J. Indust. Eng. Chem.* **2013**, *19*, 327.
48. H. He, H. X. Dai, L. H. Ng, K. W. Wong, T. C. Au, *J. Catal.* **2002**, *206*, 1.
49. F. Klingstedt, A. K. Neyestanaki, R. Byggningsbacka, L. E. Lindfors, M. Lunden, M. Petersson, P. Tengstrom, T. Ollonqvist, J. Vayrynen, *Appl. Catal. A* **2001,** *209*, 301.
50. R. J. Farrauto, R. M. Heck, *Catal. Today* **1999**, *51*, 351.
51. L. V. Mattos, E. R. Oliveira, D. E. Resasco, F. B. Passos, F. B. Noronha, *Fuel Process. Technol.* **2003**, *83*, 147.
52. L. V. Mattos, E. R. Oliveira, P. D. Resende, F. B. Noronha, F. B. Passos, *Catal. Today* **2002**, *77*, 245.
53. S. K. Bhargava, J. Tardio, J. Prasad, K. Foger, D. B. Akolekar, S. C. Grocott, *Ind. Eng. Chem. Res.* **2006**, *45*, 1221.
54. M. Abecassis-Wolfovich, R. Jothiramalingam, M. V. Landau, M. Herskowitz, B. Viswanathan, T. K. Varadarajan, *Applied Catalysis B: Environmental* **2005**, *59*, 91.
55. A. M. T. Silva, R. R. N. Marques, R. M. Quinta-Ferreira, *Applied Catalysis B: Environmental* **2004**, *47*, 269.
56. S. Imamura, in A. Trovarelli (Editor), *Catalysis by Ceria and Related Materials, Imperial College Press; London,* **2002**.
57. K. Tikhomirov, O. Krocher, M. Elsener, A. Wokaun, *Applied Catalysis B: Environmental* **2006**, *64*, 72.
58. F. Eigenmann, M. Maciejewski, A. Baiker, *Applied Catalysis B: Environmental* **2006**, *62*, 311.
59. G. Avgouropoulos, T. Ioannides, H. K. Matralis, J. Batista, S. Hocevar, *Catal. Lett.* **2001**, *73*, 33.
60. G. Avgouropoulos, T. Ioannides, C. Papadopoulou, J. Batista, S. Hocevar, H. K. Matralis, *Catal. Today* **2002**, *75*, 157.
61. P. Ratnasamy, D. Srinivas, C. V. V. Satyanarayana, P. Manikandan, R. S. S. Kumaran, M. Sachin, V. N. Shetti, *J. Catal.* **2004**, *221*, 455.
62. G. Sedmak, S. Hocevar, J. Levec, *J. Catal.* **2003**, *213*, 135.
63. G. Sedmak, S. Hocevar, J. Levec, *J. Catal.* **2004**, *222*, 87.
64. J. Kaspar, P. Fornasiero, M. Graziani, *Catal. Today* **1999**, *50*, 285.
65. A. Trovarelli, *Comments Inorg. Chem.* **1999**, *20*, 263.
66. H. C. Yao, Y. F. Y. Yao, *J. Catal.* **1984**, *86*, 254.

67. N. V. Skorodumova, S. I. Simak, B. I. Lundqvist, I. A. Abrikosov, B. Johansson, *Phys. Rev. Lett.* **2002**, *89*, 166601.
68. Q. Dong, S. Yin, C. Guo, T. Sato, *Chem. Lett.* **2012**, *41*, 1250.
69. E. Mamontov, T. Egami, R. Brezny, M. Koranne, S. Tyagi, *J. Phys. Chem. B* **2000**, *104*, 11110.
70. J. Kullgren, K. Hermannson, P. Broqvist, *J. Phys. Chem. Lett*. **2013**, *4*, 604.
71. M. P. Yeste, J. C. H. Garrido, D. C. Arias, G. Blanco, J. M. R. Izquierdo, J. M. Pintado, S. Bernal, J. A. P. Omil, J. J. Calvino, *J. Mater. Chem. A*, **2013**, *1*, 4836.
72. D.R. Lide (Ed.), *CRC Handbook of Chemistry and Physics, CRC Press*, **2005**.
73. C. T. Au, M. S. Liao, C. F. Ng, *J. Phys. Chem. A* **1998**, *102*, 3959.
74. M. J. Hei, H. B. Chen, J. Yi, Y. J. Lin, Y. Z. Lin, G. Wei, D. W. Liao, *Surf. Sci.* **1998**, *417*, 82.
75. T. V. Choudhary, D. W. Goodman, *J. Mol. Catal. A: Chem.* **2000**, *163*, 9.
76. G. J. Hutchings, M. S. Scurrell, J. R. Woodhouse, *Chem. Soc. Rev.* **1989**, *18*, 251.
77. R. J. Olsen, W. R. Williams, X. Song, L. D. Schmidt, *Chem. Eng. Sci.* **1992**, *47*, 2505.
78. S. Chattopadhyay, G. Veser, *AlChe J.* **2006**, *52*, 2217.
79. D. A. Hickman, L. D. Schmidt, *Science* **1993**, *259*, 343.
80. D. T. P. Watson, J. J. W. Harris, D. A. King, *J. Phys. Chem. B* **2002**, *106*, 3416.
81. S. F. Rice, A. H. McDaniel, E. S. Hecht, A. J. J. Hardy, *Ind. Eng. Chem. Res.* **2007**, *46*, 1114.
82. L. B. F. Jurlink, P. R. McCabe, R. R. Smith, C. L. Dicologero, A. L. Utz, *Phys. Rev. Lett.* **1999**, *83*, 868.
83. M. P. Schmidt, P. Maroni, R. D. Beck, T. R. Rizzo, *J. Chem. Phys.* **2002**, *117*, 8603.
84. R. D. Beck, P. Maroni, D. C. Papageorgopoulos, T. T. Dang, M. P. Schmidt, T. R. Rizzo, *Science* **2003**, *98*, 302.
85. J. N. Wilson, F. Zaera, *J. Phy. Chem. C* **2010**, *114*, 16946.
86. R. Horn, K. A. Williams, N. J. Degenstein, L. D. Schmidt, *J. Catal.* **2006**, *242*, 92.
87. B. C. Enger, R. Lodeng, A. Holmen, A. *Appl. Catal. A* **2008**, *346*, 1.
88. A. P. E. York, T. C. Xiao, M. L. H. Green, J. B. Claridge, *Catal. Rev.-Sci. Eng.* **2007**, *49*, 511.
89. T. Liu, C. Snyder, G. Veser, *Ind. Eng. Chem. Res.* **2007**, *46*, 9045.
90. A. Donazzi, A. Beretta, G. Groppi, P. Forzatti, *J. Catal.* **2008**, *255*, 241.
91. M. Maestri, D. Vlachos, A. Beretta, P. Forzatti, G. Groppi, E. Tronconi, *Top. Catal.* **2009**, *52*, 1983.

Chapter 2 – Molecular Beam Instrument and Experimental Methods

2.1 Molecular Beam Instrument (MBI)

MBI is an important instrument in the field of surface science, which operates under the UHV condition, to understand the kinetics and dynamics of the reaction happening on the surface of the catalyst. It was introduced first by Dunoyer in 1911[1] to study quantitative experiments. Present thesis mainly draws an attention on the kinetic aspects of the catalytic reaction with minimum amount of dynamic aspects. The detailed study about MBI and its application is well cited in references 2 and 3. A molecular beam (MB) is spatially well-defined, directed beam of gaseous molecule with uniform velocity and unidirectional, which does not undergo collision between each other.[3,4] Molecular beam (MB) application in surface science provides an insight into the kinetics and dynamics of the surface reaction. First molecular beam setup for measuring catalysis aspects was reported by King and Wells on 1978.[5] Spatially well-defined and directed MB works on the principle of single collision, which will open a pathway for performing wide variety of experiments. There is a possibility of measurement of reactant flux which pave the way for the measurement of the reaction probabilities with respect to adsorbate coverage. Unique information about the transient phase can be derived by fast variation of reactant flux for the reaction. We can control many properties of gaseous molecules by changing its flux i.e. kinetic energy, rotational and vibrational state of incident gaseous molecules; thus reaction can be studied by varying these parameters.

MB has many advantages, such as (a) without flooding the UHV chamber, high flux on the surface can be obtained and hence surface coverage can be achieved on the metal substrates, (b) single scattering condition prevails in MBI, due to which it minimizes there-adsorption of reactant gases compared to the conventional experiments, (c) pressure difference between sample surface and the background differs up to seven orders of magnitude, depending on the experimental conditions, which can be maintained throughout the experiment. Generally two types of MB have been used for such studies, one is effusive and other is supersonic and they vary in expansion conditions. These two types of MB differ in distribution of energy in the gaseous molecules. In our present study we have used only effusive MB. In effusive molecular beam the gaseous molecules effuses through small orifice from high pressure i.e. 10^{-3} mbar upto few mbar to low pressure i.e. UHV condition. This

condition implies on the expansion of the gaseous molecules into UHV without losing energy and momentum. This condition fully favours the principle of single collision.

Fig. 2.1 shows the schematic representation of MBI with an effusive MB. It comprises of three stages: first is the production of effusive MB through fine microcapillary. The second stage comprises of collimated MB formation in one direction which is usually pumped into other direction producing steady state. Commercial molecular beam setup includes one to three sets of aperture-collimator-skimmer combinations; however, after each stage the effective flux decreases however, becomes perfectly unidirectional. Present setup employs microcapillary disc with uniform capillary size as collimator and hence high flux can be obtained on the catalyst surfaces. In this way MB enters into the UHV chamber. The distance is adjusted between the MB doser and the sample in such a way that there is a minimum possible divergence of the beam flux. The beam can be directed or stopped from impinging on the sample surface with the help of shutter operation. The dynamic properties of MB are generally higher than one and it is measured in terms of Knudsen number 'Kn'.

$$\mathrm{Kn} = \frac{\lambda}{d} \qquad (2.1)$$

Where λ = Mean free path, and d = length of opening through which expansion takes place.

Under the effusive condition of MB dynamic properties of reactant gas is retained thus maintaining the Maxwell-Boltzmann distribution. Supersonic sources operate at low Knudsen numbers. Supersonic beam advantages are as follows a) narrow velocity distribution, b) variable kinetic energy and c) a large degree of control over the internal energy. As discussed above effusive MB operates at high Knudsen number has following advantages, a) maximum intensity, b) variable beam without changing beam profile, c) generation of molecular beam with lower vapour pressure due to low stagnation state pressure, d) due to less consumption of gas expensive isotopic study is possible. Generally upto now two types of MB setup has been described; one is to study gas surface dynamics[6-13] which uses supersonic source to study the dynamic parameter of the reaction. The other type of MB setup is used to study the kinetics of the surface reaction.[11,12,14-22] The product formed after the reaction or the scattered reactant molecule can be analyzed by two different ways; one is angle integrated way and the other is angle resolved way, by using quadruple mass spectrometer (QMS), bolometer or laser spectroscopy. The information about the spatial distribution of the product was well analyzed by angle resolved mode of detection.

To study the kinetics and mechanism of the reaction a simple effusive molecular beam instrument was setup in our lab.[23] The detailed technical and mechanistic aspect of

MBI is described in this segment of discussion. MBI consist of a 12 or 25 L capacity of stainless steel UHV chamber which is equipped with all required accessories to generate a

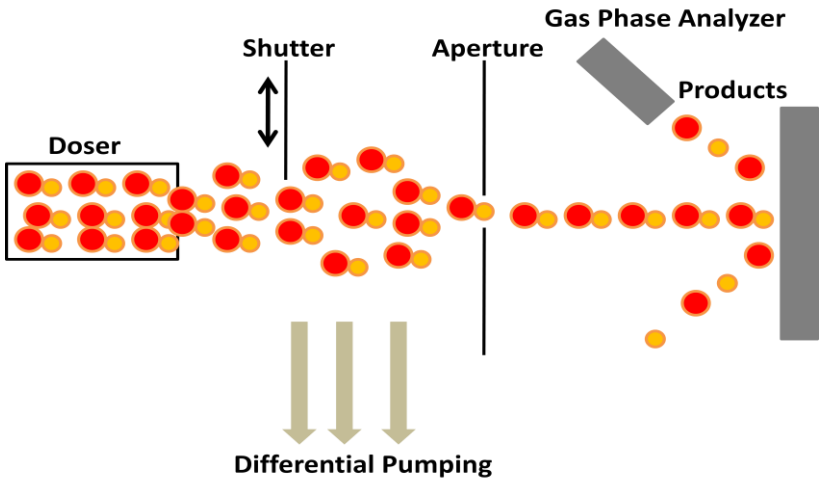

Fig. 2.1 General setup for the Molecular beam instrument (MBI).

collimated molecular beam. The UHV chamber is evacuated at a speed of 210 L/s with help of turbo molecular drag pump (Pfeiffer, TMU 261)) to a chamber base pressure of 3 x 10^{-10} Torr. MBI has MB doser which will be described later in the segment, and also equipped with sputter ion gun (AG5000, VG Scientific) which is placed exactly opposite to MB doser at 180 ^{o} (Fig. 2.2). The surface of the sample was cleaned by Ar^{+} ion sputter gun using up to 5 KV of power to generate Ar^{+} ions. The sample holder is mounted on power-thermocouple feed-through (Caburn, 30 A-DC and 5 KV), which is attached with XYZ manipulator and a rotary platform, placed perpendicular between doser and sputter ion gun. Due to this alignment sample can be rotated in all three direction as well as angular displacement is of about 360 ^{o}. Above described feed-through assembly passes through thermo-well by which the sample can be cooled to a low temperature with help of liquid nitrogen; in our present setup we can reach a minimum temperature of 125 K. The sample holder is made of niobium which is spot welded with 0.5 mm tantalum wire through which sample is resistively heated upto 1,200 K by home-built temperature controller.

MBI is equipped with stationary quadrupole mass spectrometer (QMS) (Pfeiffer, HiQuadTM, QMG 700 with QMA 410, 1–128 amu), which can detect a gas phase species upto 128 amu. The background pressure of UHV chamber is measured by cold cathode gauge (Pfeiffer, IKR270). The cold cathode gauge and QMS are placed far apart and at an angular distance with each other as well as the doser. The QMS is kept closer to the sample (distance between them is almost 10 cm) in order to detect any change in partial pressure of the component. The distance between the QMS and cold cathode gauge from the turbo molecular

pump is almost the same in order to minimize the total pressure readings. Due to the above geometrical arrangement of the accessories and devices, the least count to measure reaction probability is of 0.001 ML/s. The sample was placed inside Nb sample holder which is attached with copper barrel with help of tantalum wire, which in turn is connected to power-thermocouple feed through. A K-type thermocouple was spot welded on the surface of sample holder which in turn is also connected with thermocouple lead of feed-through. The above MBI discussed is an extension of King and well's method.[5] Clausing's[25] has introduced the concept of molecular beam flow in capillary tube. The doser is assembled in such a way that it should create low energy molecular beams.[26] Collimated gas beams finds its application in many useful experimental techniques in molecular physics, mechanistic aspect of chemical reaction, spectroscopic techniques, surface science and epitaxial growth of crystals.[27] Mostly the MB is used extensively in surface science studies.[28-36] Molecular beam doser consist of open segment of disk with multichannel array of capillary disk; the diameter of open portion of the disk is 10 mm. The enhancement factor 'E' is an important parameter to decide the quality of doser; it is defined as the ratio between true flux actually on the sample due to MB and the gas flux due to background gas pressure, P. It is expressed by following equation.[37]

$$E = 1 + fS/k_B T(1-fs)v_c A \qquad (2.2)$$

where v_c = velocity of gas molecules, $v_c = \sqrt{2\pi m k_B T}$, f = fraction of beam intercepted by the sample, k_B = Boltzmann constant, T = temperature in Kelvin, S = pumping speed, s = sticking probability of molecule, A = surface area of sample, and m = mass of the gas molecules.

Aspect ratio of microcapillary decides the beam profile, which is defined as the ratio between length (L) to diameter (a) of capillary. It has been found that microcapillary doser having aspect ratio greater than 40 has no considerable changes in beam profile except with decrease in conductance with an increase in aspect ratio.[38] In present MBI setup, we employ an aspect ratio of microcapillary doser to be around 100. This setup provides uniform flux all around the surface of the sample. The MB doser diameter is approximately 13 mm which consist of multiple arrays of microcapillary glass tubes; the length of microcapillary is 1 mm and its diameter is 10 μm (Collimated Holes Inc.).Open portion of the microcapillary is 10 mm. The doser is tightened on its head with teflon O-rings by threaded cap. The doser head is further attached with a quarter inch tube (OP) of 15 cm in length with baffles (shown in Fig. 2b) welded inside tube to avoid gas molecules to take the shape of quarter inch tube. This setup of MB doser provides a minimum dead volume with a maximum gas load as compared

to reported beam doser.[39] The MB supply was switched on and off from the sample surface by placing laterally movable shutter between the microcapillary doser and the sample. The minimum distance which can be maintained between sample to doser is 5 mm in our present MBI setup (Fig. 2.2b inset); it gives an enhancement factor 'E' of ~ 12 % and ~ 45 % fraction of beam (f) is intercepted by the surface.

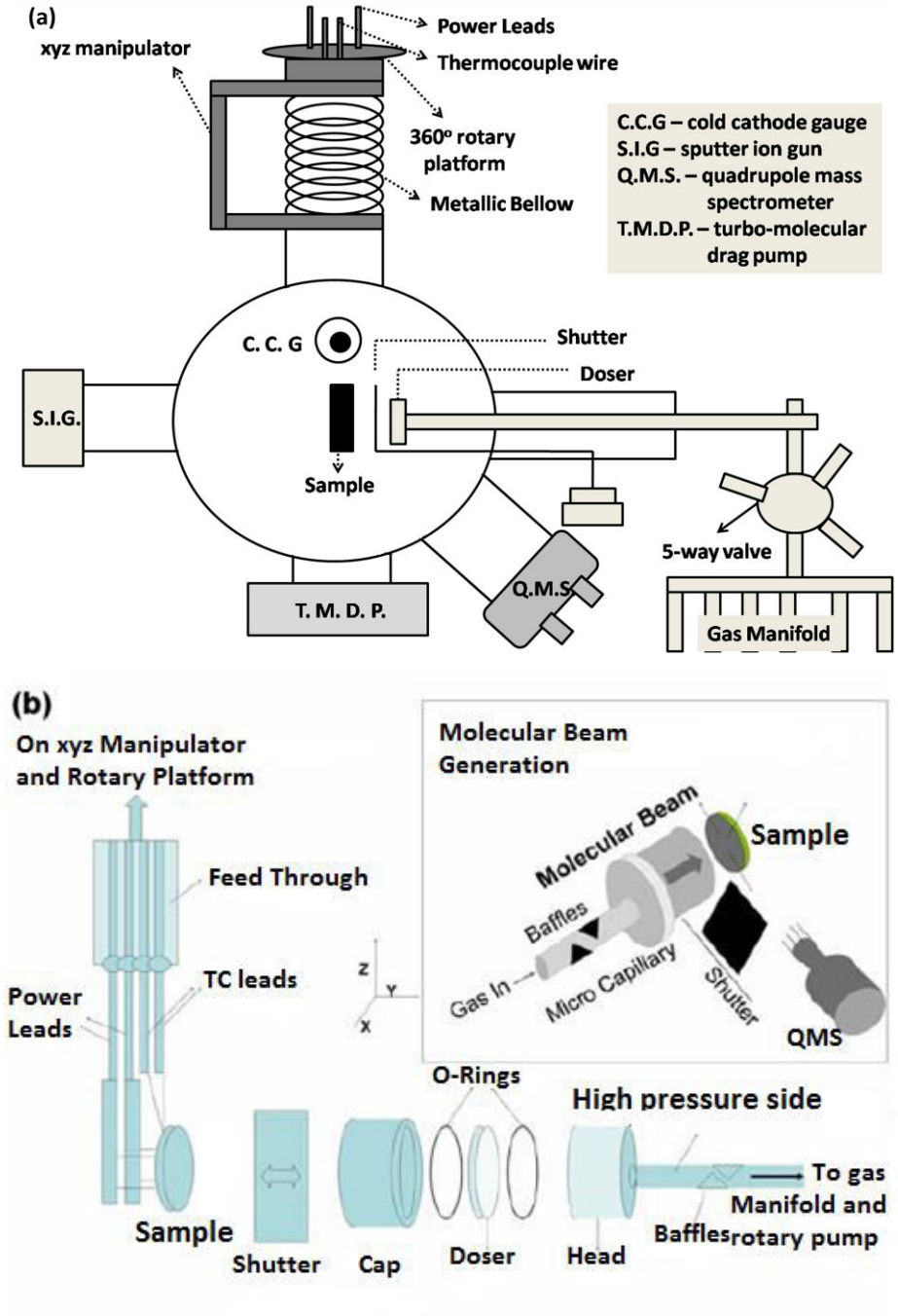

Fig. 2.2 a) Schematic representation of MBI; b) Schematics of doser assembly and process of generation of MB is shown in inset.

Fig. 2.3 shows the image of MBI one which is present earlier i.e. Fig. 2.3a and another is present MBI setup i.e. Fig. 2.3b. It is same as described above and various parts have been assigned number which is described below:

1 – QMS, 2 – turbo-molecular drag pump, 3 – Ar^+ ion sputter gun (not visible in Fig. 2.3b it is exactly placed opposite to 6, 4 – rotary drive for shutter movement, 5 – copper barrel lead and thermocouple lead, 6 – molecular beam doser setup with leak valve, 7 – gas manifold, 8 – 360 ^{o} rotatory platform and 9 – XYZ manipulator.

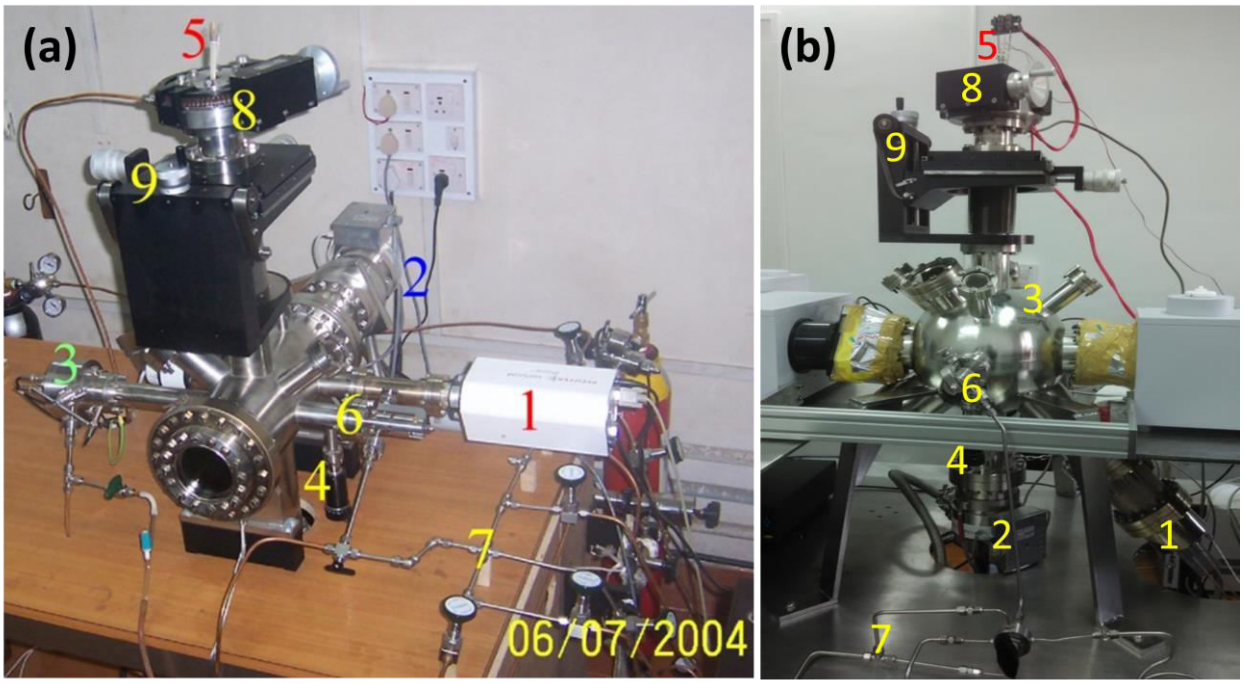

Fig. 2.3 – MBI setup a) earlier and b) present setup, in National chemical laboratory, Pune.

To calculate the adsorbate coverage at time, t,[40] fractions of the beam which impinges on the surface should be known; it is calculated by performing an experiment of cyclohexane condensation on surface of Pd(111) at 125 K in present MBI setup.[41]

$$\theta(t) = \frac{N(t)}{A} = \frac{1}{A}\int_0^t [\alpha \Delta P(\tau) + \beta s(\tau) P(\tau)] dt \qquad (2.3)$$

where, N(t) = number of adsorbate molecules, A= surface atom density of the Pd(111) sample (surface atom density of Pd = 1.53 x 10^{15} cm^{-2}), α, β are constants and independent of the beam flux, sample-to-surface distance and surface temperature. The sticking probability of cyclohexane is assumed to be unity at 125 K. Calculated value for α and β is 2.99 x 10^6 molecules/g and 1.76 x 10^5 molecules/g, respectively, for our present MBI set-up.[34] The pumping rate of present MBI setup is determined with the help of following equation.[42]

$$\rho = \rho_o \exp[(-\frac{\wedge RT}{V})t] \qquad (2.4)$$

where ρ and ρ_o, Λ and V symbolizes pumping rate, pumping coefficient, pumping constant and volume of the chamber, respectively. The gas flux in MBI was determined and maintained with help of precision leak valve and backing pressure in the gas-manifold. The pressure in gas manifold is determined by MKS Baratron pressure gauge, which was initially calibrated by equilibrating against vapour pressure of water at different temperatures. The metal and single crystal catalyst surfaces is usually cleaned in-situ by Ar^+ ion sputter gun at required temperature for sample in Ar and oxygen atmosphere, which was further annealed at higher flashing temperature in oxygen atmosphere. The procedure of cleaning is same as described by Ramsier, et. al.[43,44] However, for nanocrystalline thin films employed mostly for the present thesis has been cleaned by treatment with oxygen or hydrogen at different temperatures; such treatments are explained in the respective chapters.

2.2 Preparation of thin film

2.2.1 Preparation of CZ and metal ion doped CZ thin film

The thin film was prepared by simple sol-gel spin coating method. We have prepared thin film of ceria- zirconia (CZ) as well as metal ion doped CZ by this method. The precursor used for cerium ion source is cerium (III) nitrate i.e. $Ce(NO_3)_3.6H_2O$(Loba Chemie), zirconium ion source is zirconium oxychloride i.e. $ZrOCl_2.8H_2O$, manganese ion source is manganese nitrate i.e. $MnNO_3.4H_2O$ and ethanol (99.9 % pure) (all from Thomas backer). 0.01M solution was prepared by adding the precursor in desired stoichiometric ratio. For preparation of $Ce_{0.5}Zr_{0.5}O_2$ thin film, 0.434 g of cerium nitrate hexahydratre and 0.322 g of zirconium oxychloride was mixed in 20 ml of ethanol. The solution prepared was magnetically stirred for 3 h to make the solution transparent for complete miscibility. The as prepared solution has been utilized for spin coating on substrate; substrate used in our study for preparation of thin film is Si wafer (99.9999 % pure and 0.625 mm thick – MaTeck, Germany). The 5 µl of the above solution was taken in a micropipette and spun coated on 2.5 cm^2 area of Si wafer at a spinning speed of 8500 rpm for 120 s. Depending on the desired thickness of film; this procedure is repeated several times. The as prepared thin film was kept in oven at a temperature of 313 K for 48 h i.e. conversion of sol into gel, subsequently the temperature of oven was raised to 373 K after 48 h for 12 h to remove water vapor, if any, present in the prepared film. The amorphous thin film formed was calcined at 773 K for 1 h, at a ramping rate of 2 ^oC/min in static air. Calcination of thin film changes nature of film from amorphous to crystalline and it also removes any organic moiety (such as alcohol) which is present within the thin film. The same procedure was also applied for thin film formation on Au-Pt grid as was applied on silicon wafer, for the analysis of thin film by

HRTEM. There is a difficulty in formation of pure ceria thin film but upon doping of zirconium ion into ceria lattice adhesive property to Si wafer increases. Therefore all the results are shown in for CZ as well as metal ion doped CZ thin film in this thesis. Above described is the most common thin film preparation method adopted for all thin films prepared for the present studies. Minor changes were applied, such as spinning speed, calcination temperature, wherever required and they are mentioned in the corresponding chapters.

Thickness of thin film depends on many factors like spinning speed, viscosity of the solution, volatile nature of the solvent, spin duration etc.[45,46] Each factor has its own influence on determining the thickness of film. All the factors are separately studied and it is adjusted in such a way to get a uniform homogeneous thin film by several trial experiments. The best possible thin film quality was prepared for present studies and reported throughout the thesis. Indeed there is a scope to improve the surface quality of thin film. We are able to prepare a thin film in nano-regime with the lowest thickness of film ranging between 30-50 nm with surface roughness resembling to that of single crystal. We believe, by fine-tuning the preparation procedure and spin-coating methods, there is a possibility to improve the surface qualities of thin films.

2.2.2 Preparation of spinel cobalt oxide thin film

A polycrystalline Co-metal foil (MaTech Germany) of 1 x 1 cm^2 is placed in a niobium metal sample holder, which is heated by tantalum wire from RT to 1100 K. Surface of metal is cleaned first by dipping in 1 M aq. HNO_3 acid in the open atmosphere. Then nitric acid cleaned Co-metal foil was placed in MBI and then it is further cleaned several time by Ar^+ sputter ion gun. Then the surface of the Co-Metal foil is exposed to O_2 atmosphere in UHV chamber at an O_2 pressure of 5 x 10^{-6} torr which is heated up to 600 K for 3 h. A few layer of the surface gets oxidized into spinel cobalt oxide. Formation of Co_3O_4 was confirmed by XRD, Raman and XPS spectra.

2.3 Factors guiding thickness of film

Residual film formed by sol-gel spin coating method not only depends on spinning velocity (ω) and metal ion concentration (c_o), but it also depends on molar mass M and molar mass distribution. In general when film was formed by spinning, at that time solvent evaporates with the passage of time which in turn, residual film covers the substrate. This procedure is generally known as spin coating, which has an advantage of producing thin film in nanothick regime with uniform homogeneous thickness. Concentration of solution affects thickness of film to a great extent; for moderate concentrated solution, thickness of film is directly

proportional to the concentration,[47] while for low and high concentrated solution, deviation from the proportionality is observed.[48] Schubert et al.,[46] has studied the spin coating from a molecular point of view and shown the schematic diagram of spin coating which is shown below in Fig. 2.4.

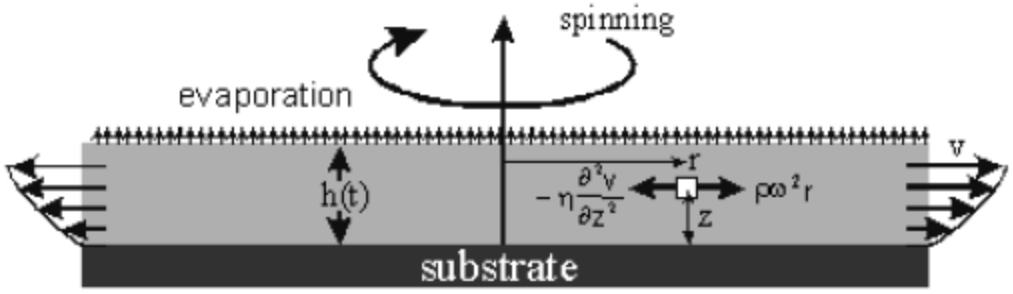

Fig. 2.4 Schematic diagram of spin coating process. (Reproduced from Ref. 46 with permission from Springer international publishing AG group)

Theory behind spin coating was first studied by Emslie et. al.[49] and Meyer-hofer et al.[50] using several simplifications. Spinning concept is based on balancing of the two centripetal and centrifugal forces for a volume element, which is shown below:

$$-\eta d^2v/dz^2 = \rho\omega^2 r \qquad (2.5)$$

where η is the viscosity, v is the velocity in radial direction and ρ is the density of the solution. The homogeneity of thickness of the film can be determined by following eq. 2.6 which is well reported in literature.[51-54]

$$h(t) = 1/(h_o^{-2} + (4\rho\omega^2/3\eta)t)^{1/2} \qquad (2.6)$$

where h_o is the film thickness at the beginning. Mayerhofer obtained an expression for the thickness of film after infinite spinning time, which is shown in eq. 2.7.

$$h_\infty \sim \omega^{-2/3} e^{1/3} \eta^{1/3} c_o \qquad (2.7)$$

Pannek et. al.[55] recently shown the influence of spinning time on thickness of film which is expressed by eq. no. 2.8.

$$h(t) = h_\infty + \Delta h \exp(-kt) \qquad (2.8)$$

$$\text{with } k = e/h_\infty \qquad (2.9)$$

where e is the constant evaporation rate.

From the thorough study and theoretical background it is known that the thickness of the film is not guided by one parameter, but on several parameters which is discussed above. Apart from these parameters volatility and viscosity of the solvent also plays a role in determining the thickness and uniform surface quality of thin films. More volatile solvent will evaporate faster leaving behind a thick and uneven film while less volatile solvent do not

evaporate easily on spinning thus spill over takes place and no film or poor quality thin film was formed on the substrate. Another factor for formation of thin film on substrate is the lattice match between the thin film and substrate materials; if lattice mismatch happens adhesive property becomes weak and generally there are difficulties in thin film formation.

2.4 Sol-Gel method

We applied sol-gel method for spin coating of material on to the substrate. The name sol-gel itself depict the micro-particle or molecules agglomerate in solution (sols) which under controlled condition forms a coherent network (gel) by linking together. There are two variations in sol-gel technique, one is based on colloidal method and other is based on polymeric or alkoxide pathway. The only difference between these two techniques is the difference in use of precursor. Both methods generally involve dissolving the precursor molecule in suitable solvent; water is used as a solvent for the colloidal route while alcohol is used as a solvent for the polymeric route. Sometimes Acids (like HCl) and bases (like potassium hydroxide) are used to activate the precursor. Activated precursor grows into network with passage of time and temperature. During this period of time viscosity of solvent increases exponentially until gelation occurs. If the gel was dried by evaporation, capillary forces lead to shrinkage of network leading to formation of xerogel. Under supercritical condition network structure is maintained and porosity is preserved within materials.

Sol-gel method enables the mixing of particle at atomic level and it results in small particle which are easily sinterable. It is a very good technique for the formation of thin films as it prevents agglomeration of particles at higher temperature. Hence, we used sol-gel spin coating method for the formation of CZ and metal ion doped CZ thin film.

2.5 Physicochemical characterization

2.5.1 Introduction

To understand the nature and characteristic property of a material, it has to be thoroughly analyzed by its physicochemical characterization. There are various techniques utilized for the characterization of materials like diffraction, spectroscopy, microscopy, and adsorption - desorption based methods. These techniques provides information about phase structure, crystallinity, crystallite size, optical properties, surface structure, textural properties, nature of active sites, morphology, particle size, acidity and other characteristic features. Besides, it is possible to know the nature as well as chemical states of the dopant. Through various characterizations one can correlate the structure-activity relationship and this helps to enhance the activity of catalyst for various applications. Various analytical techniques have been used to characterize the catalyst which includes , X-ray diffraction

analysis (XRD), Raman spectroscopy, profilometer, surface area and pore volume measurements, transmission electron microscopy (TEM), AFM (Atomic force microscopy), energy dispersive x-ray (EDX) analysis, x-ray photoelectron spectroscopy (XPS), scanning electron microscopy (SEM). All these techniques help to understand the nature of the catalyst, such that it can be improved or designed in a better way towards better activity. The techniques used in this thesis are described in a brief manner highlighting the experimental techniques which is used for study. For brevity, extensively used technique or special techniques employed in this thesis are discussed in the following.

2.5.2 Theory and experimental procedures

2.5.2.1 TEM (Transmission Electron Microscopy)

Determination of structure, porosity, particle size and morphology of nanomaterials is of utmost importance in today's research as it provides information about structure-property correlation. Since optical microscope has resolution limitations, which pave a way for discovery of electron microscopy by Knoll and Ruska in 1932. HRTEM works on the principle of evaluation of transmitted electron by the sample. A beam of focussed electron passes through the sample to form an image and gives information related to sample like particle size, porosity, distribution at a spatial resolution of 1.4 nm. HRTEM can focus on a single nano particle to determine its size and morphology. This technique is useful to variety of materials like metals, ceramics, semiconductors, minerals, polymers etc. Electron gun, voltage generator, vacuum system, electromagnetic lenses and recording devices clubbed and work together in a HRTEM setup. The specimen sample was illuminated by thermionic gun (tungsten filament, LaB_6 crystal) or field emission gun. The resolution of electron microscope was determined by acceleration voltage of electron. The electron beam was directed to thin sample by passing it through condenser lens system. The thickness of sample which can be evaluated by HRTEM is in range of 50 to 100 nm. High vacuum is maintained inside microscope column to prevent scattering of electrons by atmospheric component. The image and diffraction pattern is formed at image plane of objective lens and at back focus plane. Image mode is operated in transmitted electrons while diffraction mode is operated in diffracted electrons. Diffraction pattern from selected area of specimen is known as selected area electron diffraction (SAED). General requirement for high resolution is the high instrumental resolving power and high image contrast and this technique is known as HR-TEM. A FEI TECNAI 3010 electron microscope operating at 300 kV (Cs = 0.6 mm, resolution 1.7 Å) was employed for all HR-TEM measurements of the sample.

We have carried out TEM analysis of CZ and metal ion doped CZ sample in two ways. The first method involve scratching of thin film formed on Si wafer and sonicating it into isopropyl alcohol and then drop casting it on carbon coated copper grid (Ted Pella, USA). The other method involve preparation of thin film on Au-Pt grid (Ted Pella, USA) by same procedure as was used to prepare thin film on Si wafer. The Au-Pt grid containing the sample was used for TEM analysis. Analysis of thin film formed on Au-Pt grid gives clear view of thickness, roughness and porous nature of thin film. Au-Pt grid is a Pt coated Au grid which can withstand high calcination temperature. It comes in 300 and 400 mess grid. The image of Pt coated Au grid is given in Fig. 2.5.

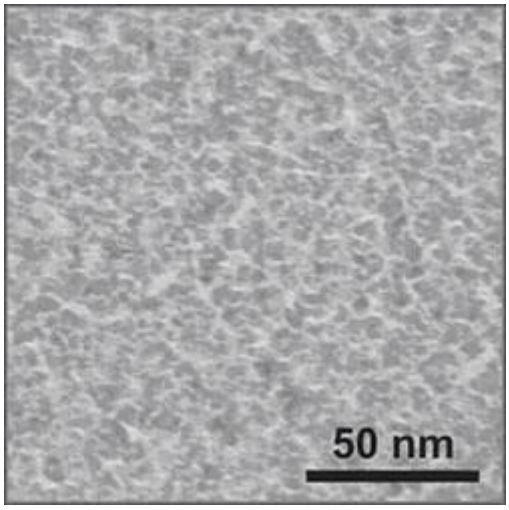

Fig. 2.5 Image of Au-Pt grid..

2.5.2.2 Raman Spectroscopy

Solid materials can be analyzed by vibrational spectroscopy by recording its unique fingerprint spectra. Raman spectroscopy is one of the finest analytical tool which gives vibrational spectrum; it helps to analyze the physical and chemical properties of materials. The phenomenon of inelastic scattering of light was discovered by Sir Chandrashekharan Venkata Raman in 1928, which is known as Raman Effect. It explains wavelength shift in small fractions of radiations scattered by molecules which have different frequency compared to that of incident beam.[56] Scattered light was used in Raman spectroscopy for analysis of structure, symmetry, electronic environment and bonding of molecule. Monochromatic light was used to irradiate the sample which generates two types of light scattering, elastic and inelastic. In 'elastic scattering' photon frequency do not change or wavelength and energy does not change, while in 'inelastic scattering' photon frequency changes due to excitation or deactivation of molecular vibrations. In inelastic scattering change in photon frequency is accompanied by loss or gain of some amount of energy by photon. This is accompanied by

three type of phenomenon when light is incident on a molecule. The first phenomenon where light interacts with molecule, but net exchange of energy is zero; this results in same frequency as that of incident light ($E = E_o$). This phenomenon is called as Rayleigh scattering. The second phenomenon happens when light incident on material interact in such a way that net exchange of energy is energy of one molecular vibrations. In this case photon gains vibrational energy by interacting with molecule, which results in higher frequency of scattered photon compared to that of incident photon ($E = E_o + E_v$), this is known as anti-stokes Raman scattering. Third phenomenon occurs when light interacts with molecules causes gain of energy of molecule due to transfer of energy from photon, then scattered light has a lower frequency compared to that of incident photon ($E = E_o - E_v$), this is known as stokes Raman scattering. The Raman spectra was recorded and reported in this thesis was carried out with Horiba JY LabRAM HR 800 Raman spectrometer coupled with microscope in reflectance mode. It uses monochromatic laser source which have a wavelength of 633 nm with spectral resolution of 0.3 cm^{-1}.

2.5.2.3. Profilometer

Profilometer is an important and simple instrument which is used for measuring surface profile of thin film samples in order to quantify its roughness and the thickness. Generally, two types of profilometers are available. Contact and noncontact (optical) profilometer are in use to determine the surface profile of a sample. Contact profilometers have a diamond stylus which first moves vertically and then laterally along the specified distance on the sample with specific force. It is very sensitive as it measures small surface variation in vertical stylus as a function of position. Generally contact mode profilometer measures vertical features ranging from 10 nm to 1 mm. Analog signal was generated by height position of diamond stylus which get transformed into digital signal and thus stored, analyzed and displayed. The diamond stylus is very soft which can bear a force of 1 to 50 mg and it has a diameter ranging between 20 nm to 50 µm. Advantages of contact profilometer is that it measures the surface nature of thin film samples.

An optical profilometer is a non contact method of surface profiling which gives similar results as was obtained by stylus based profilometer. The advantage of optical profilometer over contact profilometer is that it speeds up its acquisition electronics and the reliability of the results are more as it do not touch the sample surface which may cause wear and tear of surface. We have used contact profilometer i.e. Dektak profilometer to determine thickness of film for our studies in this thesis. Thickness of CZ and metal ion doped CZ was measured with the step distance of 200 nm per scan over a distance of about 2 mm.

2.5.2.4. Atomic force microscopy

Atomic force microscopy (AFM) of scanning force microscopy (SFM) is a nanoscience instrument with very high resolution scanning probe microscopy (SPM). It is thousand times better than optical diffraction limit as its resolution is of the order of a nanometer.AFM functions through cantilever which has a sharp tip; cantilever is made of silicon or silicon nitride with tip radius of curvature of the order of nanometers. When cantilever tip is brought in near vicinity of sample surface, force is experienced between tip and surface which produces deflection in cantilever. Various types of forces can be measured by AFM like Vander Waal's forces, electrostatic forces, chemical bonding, capillary forces, magnetic forces, salvation forces etc. There are two different mode of operation of AFM one is static mode (contact) and other is a variety of dynamic (non contact or "tapping") mode, where cantilever is vibrated or oscillated at a certain frequency. In contact mode tip is dragged on sample surface and the signals are measured in two ways; one is measured by deflection of cantilever and other by keeping the cantilever position constant. In contact mode force on tip is kept constant and its height changes as it moves on the surface of the sample. Generally low stiffness cantilever are used to produce better signal due to presence of noise/thermal drift. Tapping mode is used for analysis generally in ambient condition where a liquid meniscus layer develops. The tip of cantilever is placed close enough to measure short range forces without sticking to the sample. In tapping mode cantilever is made to oscillate near to its resonance frequency. Various forces like Vander Waal's forces, dipole-dipole interaction, electrostatic forces changes the amplitude of cantilever oscillation, and control electronics

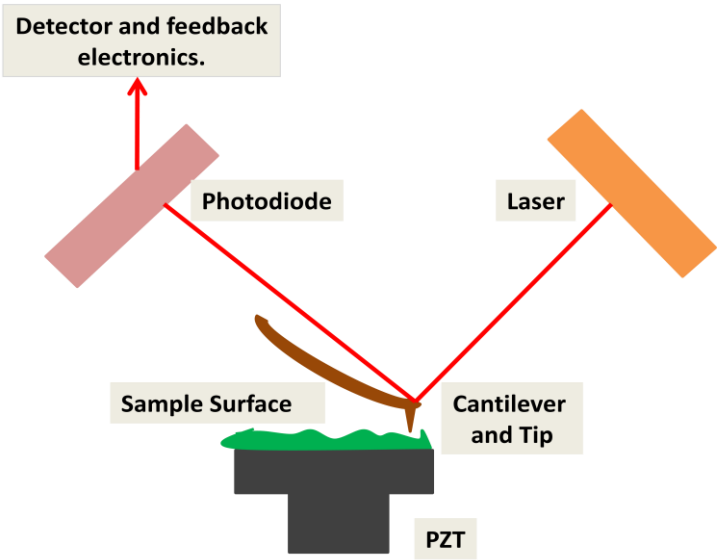

Fig. 2.6 Block-diagram of AFM.

adjusts the height of cantilever to maintain the amplitude of its oscillations. A tapping AFM image is produced by imaging force of intermittent contact between tip with the sample surface. In non-contact AFM mode tip of cantilever do not touch the surface of the sample. In non-contact mode cantilever is set in oscillation at its resonant frequency or just above where amplitude of oscillation is in few nanometer and down to few picometer. Under these conditions, cantilever is deflected by Vander Waal's forces so, its height is adjusted. At each data point the tip to sample distance is measured which helps scanning software to construct a topographic image of the surface of sample. Fig. 2.6 shows the block-diagram of AFM.

In this thesis we have determined the morphology of the sample by using AFM at ambient conditions using a multimode scanning probe microscope installed with the nanoscope IV controller (Vecco Instrument Inc., Santa Barbara, CA.).

2.5.2.5. Mass Spectrometer

Mass spectrometer is an analytical instrument which is able to measure the masses as well as relative concentration of atoms and molecules. It basically makes the use of magnetic field on moving charged particles. A schematic representation of the processes happening in mass spectrometer is shown below.

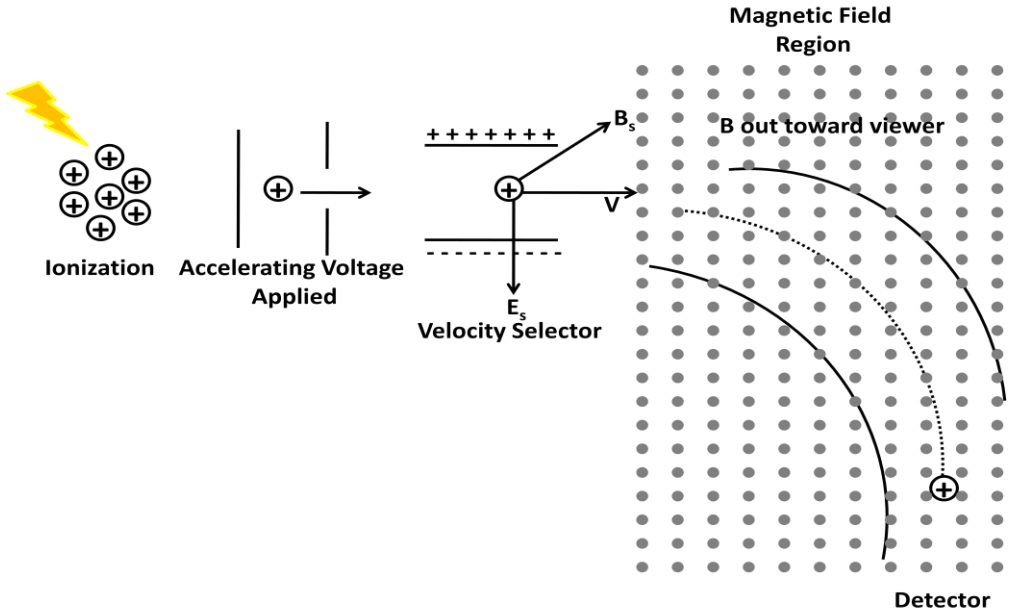

Fig. 2.7 Schematic diagram of working of mass spectrometer.

After ionization, acceleration and selection of single velocity particles, the ions move into a mass spectrometer region where radius of path and thus the position on the detector is a function of mass. The radius of path of ions produced by magnetic field is shown in eq. 2.10 below.

$$r = \frac{mv}{qB} \qquad (2.10)$$

where r is the radius of path, m is the mass of particle, v is the velocity of particle produced by accelerating voltage V, q is the charge on the particle and B is the applied magnetic field. This is the basic principle in which mass spectrometer works, let's elaborate it. First process is the ionization of atoms or molecules into ions into vacuum chamber, thereafter ions from vacuum chamber enters into powerful electric field, where it is accelerated. Different ions have different amount of charge on them, so ion having more charge are accelerated more and in this way charged ions are separated. Now charged ions enter into magnetic field and they take a shape of arc. Lighter charged particles in magnetic field bend more compared to heavier charged particles. Computerized detector records mass spectrum of different charged particles depending on number of ions reaching to detector for each mass/charge.

For our study on various parameter and reactions in this thesis, we have used a quadruple mass spectrometer (Pfeiffer, HiQuadTM, QMG 700 with QMA 410, 1–128 amu) for the detection of all the relevant species of the reaction. This mass spectrometer is highly sensitive having broad dynamic range with extremely fast measuring speed. It analyzes gas concentration by means of integrated matrix calculation. This mass spectrometer consists of QMA 410 analyzer which can measure a mass in range of 1 – 128 amu; it has a detection limit of 3.75 x 10^{-16} torr/5 x 10^{-16} mbar gas pressure. The bake out temperature of analyzer is about 673 K which is very advantageous. This mass spectrometer analyses all the fragments as well as the isotopes of elements with high sensitivity. This mass spectrometer is kept near to the sample at a distance of 10 cm due to which we are able to detect even a small change in partial pressure during reaction condition.

2.6 References

1. G. Comsa, *Surf. Sci.***1994**, *300*, 77–91.
2. R. Campargue, *Atomic and Molecular beams: The state of the art 2000, Springer Verlag, Berlin and Heidelberg*, **2001**.
3. G. Scoles, D. Bassi, U. Buck, D. Lainé, *Atomic and Molecular Beams Methods I, Oxford University Press, Oxford*, **1988**.
4. N. F. Ramsey. *Molecular Beams. Oxford University Press, Oxford*, **1956**.
5. D. A. King, M. G. Wells *Surf Sci* **1972**, *29*, 454.
6. J. A. Barker, D.J. Auerbach, *Surf. Sci. Rep.* **1985**, *4*, 1.
7. C. T. Rettner, D. J. Auerbach, J. C. Tully, A. W. Kleyn, *J. Phys. Chem.* **1996**, *100*, 13021.
8. S. T. Ceyer, W. J. Siekhaus, G. A. Somorjai, *J. Vac. Sci. Technol.* **1981**, *19*, 726.

9. M. E. M. Spruit, E. W. Kuipers, M. G. Tenner, J. Kimman, A. W. Kleyn, *J. Vac. Sci. Technol.* **1987**, *A5*, 496.
10. M. G. Tenner, E. W. Kuipers, W. Y. Langhout, A. W. Kleyn, G. Nicolasen, S. Stolte, *Surf. Sci.* **1990**, *236*, 151.
11. K. D. Gibson, S.J. Sibener, *J. Chem. Phys.* **1988**, *88*, 791.
12. L. S. Brown, S. J. Sibener, *J. Chem. Phys.* **1988**, *89*, 1163.
13. J. Häger, H. Walther, *Annu. Rev. Mater. Sci.* **1989**, *19*, 265.
14. C. Duriez, C. R. Henry, C. Chapon, *Surf. Sci.* **1991**, *253*, 190.
15. B. N. Eldridge, M. L. Yu, *Rev. Sci. Instrum.* **1987**, *58*, 1014.
16. M. Balooch, W. J. Siekhaus, D. R. Olander, *J. Phys. Chem.* **1984**, *88*, 3521.
17. J. Liu, M. Xu, T. Nordmeyer, F. Zaera, *J. Phys. Chem.* **1995**, *99*, 6167.
18. S. M. Wetterer, D. J. Lavrich, T. Cummings, S. L. Bernasek, G. Scoles, *J. Phys. Chem. B* **1998**, *102*, 9266.
19. K. Hayek, M. Fuchs, B. Klötzer, W. Reichl, G. Rupprechter, *Top. Catal.* **2000**, *13*, 55.
20. I. Stara, V. Matolin, *Surf. Sci.* **1994**, *313*, 99.
21. R. Denecke, M. Kinne, C. M. Whelan, H. P. Steinrück, *Surf. Rev. Lett.* **2002**, *9*, 797.
22. J. Libuda, I. Meusel, J. Hartmann, H. J. Freund, *Rev. Sci. Instrum.* **2001**, *71*, 4395.
23. a) K. Thirunavukkarasu, C. S. Gopinath, *Catal Lett* **2007**, *119*, 50. b) C. S. Gopinath, Anjani Dubey, S. K. Kolekar. (In preparation)
24. P. Clausing, *J. Vac. Sci. Tech.* **1932**, *8(5)*, 636.
25. H. Pauly, *In: Scoles G (ed) Atomic and molecular beam methods, vol 1. Oxford University Press*, **1988,** p 99.
26. G. Scoles, *In: Scoles G (ed) Atomic and molecular beam methods, vol 1. Oxford University Press*, **1988**, p 1.
27. H. J. Freund, M. Baumer, J. Libuda, T. Risse, G. Rupprechter, S. Shaikhutdinov, *J. Catal.* **2003**, *216*, 223.
28. J. Hoffmann, I. Meusel, J. Hartmann, J. Libuda, H. J. Freund, *J. Catal.* **2001**, *204*, 378.
29. V. Johanek, S. Schauermann, M. Laurin, C. S. Gopinath, J. Libuda, H. J.Freund, *J. Phys. Chem. B* **2004**, *108*, 14244.
30. C. R. Henry, *Surf. Sci. Rep.* **1998**, *31*, 23 and references therein.
31. J. Libuda, H. J. Freund, *Surf. Sci. Rep.* **2005**, *57*, 157.
32. A. W. Kleyn, *Chem. Soc. Rev*. **2003**, *32*, 87.
33. K. Thirunavukkarasu, *Molecular beam studies of nitric oxide reduction reactions on Pd(111) surfaces Ph.D. Thesis, University of Pune*, **2006**.

34. M. Bowker, R. P. Holroyd, R. G. Sharpe, J. S. Corneille, S. M. Francis, D. W. Goodman, *Surf. Sci.***1997**, *370*, 113.
35. K. Thirunavukkarasu, K. Thirumoorthy, J. Libuda, C. S. Gopinath, *J. Phys. Chem. B* **2005**, *109*, 13283.
36. C. T. Campbell, S. M. Valone, *J. Vac. Sci. Technol. A* **1985**, *3*, 408.
37. J. M. Guevremont, S. Sheldon, F. Zaera, *Rev. Sci. Instrum.* **2000**, *71*, 3869.
38. G. L. Fisher, C. A. Meserole, *J. Vac. Sci. Technol. A* **2005**, *23*, 722.
39. J. Liu, M, Xu, T. Nordmeyer, F. Zaera, *J. Phys. Chem.* **1995**, *99*, 6167.
40. K. thirunavukkarasu, C. S. Gopinath, *Catal. Lett.* **2007**, *119*, 50.
41. S. Nagarajan, K. Thirunavukkarasu, C. S. Gopinath, S. D. Prasad, *J. Phys. Chem. C* **2011**, *115*, 15487.
42. R. D. Ramsier, Q. Gao, N. H. Waltenburg, K. W. Lee, O. W. Nooij, L. Leerts, J. J. T. Yates, *Surf. Sci.* **1994**, *320*, 209.
43. R. D. Ramsier, Q. Gao, N. H. Waltenburg, J. J. T. Yates, *J. Chem. Phys.* **1994**, *100*, 6837.
44. T. P. S. Clair, D. W. Goodman, *Top. Catal.* **2000**, *13*, 5.
45. D. W. Schubert, T. Dunkel, *Mat. Res. Innov.* **2003**, *7*, 314.
46. D. W. Schubert, *Poly Bull*, **1997**, *38*, 177.
47. T. Dunkel, *Diploma Thesis, GKSS Forschungszentrum & F. H. Aachen* **2000.**
48. A. G. Emslie, F. T. Bonner, L. G. Peck, *J. Appl. Phys.* **1958**, *29*, 858.
49. D. Meyerhofer, *J. Appl. Phys.* **1978**, *49*, 3993.
50. D. E. Bornside, C. W. Macosco, L. E. Scriven, *J. Appl. Phys.* **1989**, *66*, 5185.
51. D. E. Bornside, R. A. Brown, P. W. Ackmann, J. R. Frank, A. A. Tryba, F. T. Geyling, *J. Appl. Phys.* **1993**, *73*, 585.
52. A. Otzekin, D. E. Bornside, R. A. Brown, P. K. Seidel, *J. Appl. Phys.* **1995**, *77*, 2297.
53. L. E. Stillwagon, R. G. Larson, *Physics of Fluids A* **1992**, *4*, 895.
54. M. Pannek, T. Dunkel, D. W. Schubert, *Mat. Res. Innov.* **2001**, *4*, 340.
55. H. P. Klug, L. E. Alexander*, X-Ray Diffraction Procedures: For Polycrystalline and Amorphous Materials, John Wiley and Sons, New York,* **1974**, p. 618.
56. C.V. Raman, R.S. Krishnan, *Nature* **1928**, *121*, 501.

Chapter 3A – Porous Ceria-Zirconia Thin Films Towards Bridging the Material Gap in Heterogeneous Catalysis.

An attempt has been made to bridge the material gap, which exists between ideal single crystals and real world powder nanocatalyst employed in surface science and heterogeneous catalysis, respectively. Simple wet chemical method (sol-gel and spin-coating deposition) has been applied to make continuous $Ce_{1-x}Zr_xO_2$ (x = 0-1) (CZ) thin films with uniform thickness (~40 nm) and smooth surface characteristics. Uniform thickness and surface smoothness of the films over a large area was supported by a variety of measurements. Molecular beam (MB) studies of O_2 adsorption on CZ surfaces reveals the oxygen storage capacity (OSC), and sticking coefficient increases from 400 to 800 K. Porous nature of Ce-rich CZ compositions enhances O_2 adsorption and OSC, predominantly due to O-diffusion and redox nature, even at 400 K. A good correlation exists between MB measurements made on CZ films for oxygen adsorption, and OSC, and ambient pressure CO oxidation on powder form of CZ; this demonstrates the large potential to bridge the material gap. CZ was particularly chosen as a model system for the present studies, since it has been well-studied and a correlation between surface science properties made on thin films and catalysis on powder CZ materials could be a litmus test.

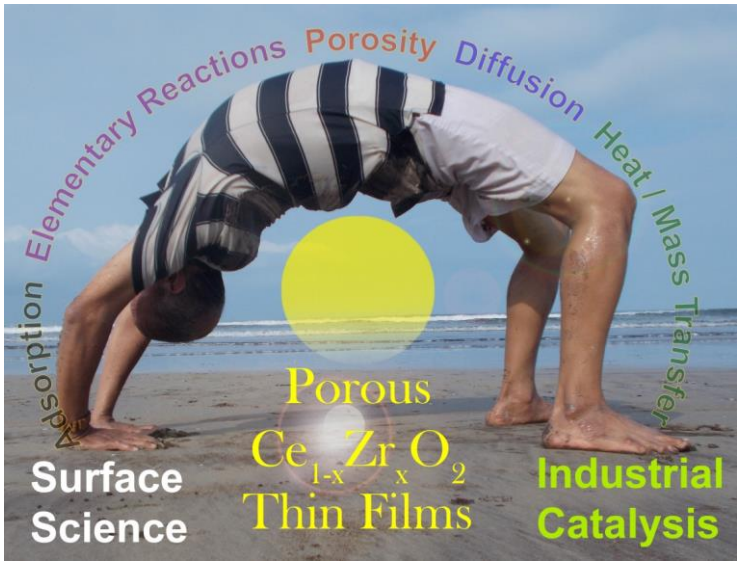

Ambient catalysis on ceria-zirconia nanocatalyst correlates well with surface properties measured through molecular beam on thinfilm and close the material gap.

3A. Introduction

Traditionally, surface science methods employed ideal single crystal materials to explore the fundamental aspects of heterogeneous catalysis under ideal/controlled conditions, like ultra high vacuum (UHV) and atomically clean surfaces.[1-9] Indeed, single crystal surfaces that have been investigated by surface science method consist only catalytically active materials. However, real-world catalyst, in general operates under high temperature and at ambient or high pressure conditions.[10-13] Extremely different conditions most often lead to a "*disconnect*" between the findings from ideal and real world conditions.[2,3] This is further compounded by the complexity of real world catalysts, by the addition of several components, such as, co-catalyst, spacers, stabilizer, and promoters (electronic and structural).[8,10-13] How different components of a catalyst interact with each other remains to be explored by surface analysis methods in a reliable manner. Complexity of the real world catalyst material and simplicity of the ideal single crystal leads to a huge material gap that exists between the two conditions. A possible way to address the above problem is to make the real world catalyst in the form of thin films with surface qualities closer to that of single crystal, so as to represent and retain the complexities of the industrial catalysts and the simplicity of the single crystal simultaneously. This is expected to decrease the material gap to a significant level. Although, there could be complications such as diffusion of surface-adsorbed species into bulk, the above approach is, in our opinion, definitely worth in terms of reproducing the overall properties of real world catalysts. In view of the net advantages, we ventured into making high quality thin films by simple chemical method and characterised the same by physico-chemical, particularly surface science, means.

Over the years, surface science studies on single crystals and metal nanoparticle/metal oxide model surfaces lead to molecular level understanding of catalysis.[1-16] In this regard one of the major challenges is to develop catalytically relevant thin films to bridge the material gap between surface science and heterogeneous catalysis. Such thin film models are closer to the "real world" catalyst and more importantly when coupled with in-situ surface sensitive techniques, such as molecular beam (MB) studies, ambient pressure photoelectron spectroscopy[16-20] could give more reliable and complex kinetic data with further insights into the understanding of working of a catalyst. To make the attempt more meaningful, we chose a material that is catalytically active on its own without any other components. In fact, ceria-zirconia (CeO_2-ZrO_2) (CZ) is a material, widely employed for different applications, of our choice for the present study. We report in this chapter on the simple chemical mean to prepare homogeneous thin films, with an exclusive aim to bridge the material gap to a

significant extent. Further, present method can also be very well extended to make high quality thin films for various applications, from window coating to solar cells for photovoltaics.[21]

Although thin film preparation reports are available in the literature, our method is significantly different, especially in achieving desirable surface qualities along with smooth surfaces as well as textural characteristics. In fact, thin films reported in this manuscript represent a typical industrial catalyst to a good extent. We also underscore the efforts made in the past along the idea of bridging the material gap.[22-23] Niemantsverdriet et al., successfully employed spin coating technique for creating metal supported thin films for exploring molecular level details of reactions ranging from ethylene polymerization to Fischer Tropsch synthesis.[24,25] Similarly, sol-gel dip coating method employed by Brinker et al is another convenient way for making high quality thin films for mimicking catalytically relevant surfaces.[26] However, many problems are yet to be answered; importantly the correlation between surface properties measured on thin films under ideal conditions, and catalysis on corresponding powder materials and measured at ambient pressure and high temperatures.

CZ mixed oxide is a versatile material for various applications, such as, solid oxide fuel cell (SOFC),[27-29] three way catalytic convertor (TWC),[30-33] oxygen storage capacity (OSC),[34-37] etc. This is due to thermal stability or sinter resistivity, and the ability to retain surface area and OSC after high temperature treatment, compared to pure ceria.[27-37]Since catalysis aspects of CZ are well-known, the present study employs the same to validate the methodology and the hypothesis involved. There are various thin film preparation methods available such as, sol-gel, dip coating, physical vapour deposition.[38-42]Among various methods, sol-gel synthesis with spin coating method is a very simple and cost effective method for the preparation of thin films. Indeed, the above combination is good for the deposition of thin homogeneous film over a large surface area.[38-42] The advantage of the sol-gel method is that the particle of the film does not aggregate due to electrostatic repulsion irrespective of amorphous or crystalline nature of the film. Above all this method could be practised in any wet chemical laboratory, since the requirements is very minimal. We also expect that many other laboratories might adopt this method to prepare high quality thin films to bridge the material as well as pressure gap exists in heterogeneous catalysis.

Herein, we report the synthesis and thorough textural characterization of CZ thin films which could be utilized for several surface science studies for understanding the redox[43] properties of this material under *operando* conditions. Further the present method of thin film preparation also can be extended to variety of oxide surfaces.[44] CO oxidation was evaluated

in powder form to explore the redox nature of CZ catalysts. MB method was employed to measure the fundamental adsorption characteristics, such as sticking coefficient (s), bulk OSC, and how porosity influences the OSC.

3A.2 Experimental Section

3A.2.1 Preparation of $Ce_{1-x}Zr_xO_2$ Thin films

0.1 M solution of Ce^{3+} and Zr^{4+} is made by adding cerium (III) nitrate with zirconium oxychloride in required stoichiometric proportion in ethanol to form $Ce_{1-x}Zr_xO_2$. 0.434 g of cerium nitrate and 0.322 g of the zirconium oxychloride was added to 20 ml of ethanol to prepare $Ce_{0.5}Zr_{0.5}O_2$. The solution was stirred for 3 h. The clear transparent sol has been utilised for spin coating on Si wafer (99.9999% pure and 0.625 mm thick - MaTeck, Germany), before it is converted into gel. 5 µl of the above solution was taken in a micropipette and spun coated on ~2.5 cm^2 area of Si wafer at a spinning speed of 8500 rpm for 120 s. The above procedure was followed for preparation of thick film of about 500-600 nm, by repeating the spin-coating procedure for six-eight times. Thin/thick film was kept at 313 K in an oven for 48 h; subsequently the temperature was raised to 373 K and heated for 12 h. Finally, the above films were heated to 773 K in a muffle furnace at a heating rate of 2 deg/min. in static air, and calcined for 1 h. Nanocrystalline thin film was also prepared directly on the Au-Pt grid (see Fig. No. 5 in chapter 2 for images of Au-Pt grid) by the same procedure adopted for Si wafer, especially for HRTEM measurements. High quality pure CeO_2 thin films could not be prepared by the above procedure, and poor quality CeO_2films formed also peels off from the Si-surface relatively easily. Zr-addition to ceria dramatically improved the adhesion characteristics and hence most of the results are given for CZ thin films.

The thickness of the film depends on many factors, such as, spinning speed, viscosity of the solvent, spin duration.[23,45] Each factor has its influence on the thickness of the film. The optimum condition for the formation of the required thickness of the film was fixed by several attempts. Although several different conditions have been attempted, the best quality thin films obtained are reported in this communication. In fact, there is scope to improve the surface quality of the films, by varying viscosity of the solvent, spinning speed etc.

3A.2.2 Instrumental Methods

Structure and crystallinity of the CZ thin and thick films were determined by PANalytical X'pert Pro dual goniometer diffractometer.[46] Sample was rotated throughout the scan to minimize the preferential orientation. Cu Kα (1.5418 Å) radiation source with Ni filter was used for x-ray diffraction (XRD). Data collection was carried out by using the flat sample

holder in Bragg-Brentango geometry. Sample was scanned at a step size of 0.00835°/s. Thickness of the film was determined by the profilometer (Dektak profilometer). Thickness of CZ thin film was measured with the step distance of 200 nm per scan over a distance of about 2 mm. HRTEM (FEI – 300 kV instrument) analysis was carried out in a bright field mode with selected area electron diffraction pattern (SAED). Nanocrystalline thin film was drop casted after sonication on the carbon coated copper grid. Further, the as prepared thin films on Au-Pt grid (Ted Pella, USA) were also employed for HRTEM measurements. Morphology of the thin film was determined by AFM at ambient conditions using a multimode scanning probe microscope installed with the nanoscope IV controller (Vecco Instrument Inc., Santa Barbara, CA.) and SEM (FEI, Quanta 200 3D). Energy dispersive x-ray (EDX) analysis was performed in the SEM system in the spot profile mode on the specific zone of thin film.[47] N_2adsorption-desorption isotherms for powder materials were recorded with Quantachrome Autosorb automated gas sorption system (NOVA 1200). Brunauer-Emmett-Teller (BET) equation was used to calculate the surface area from the adsorption branch of the isotherm. Pore size distribution was calculated from nitrogen sorption isotherm using Barrett-Joyner-Halenda (BJH) method. XPS measurements has been made using a custom built ambient pressure XPS system from Prevac and equipped with VG Scienta SAX 100 emission controller monochromator using Al Kα anode (1486.6 eV) in transmission lens mode.[48,49] Photoelectrons are energy analyzed using VG Scienta's R3000 differentially pumped analyzer. The spectra were recorded at pass energy of 50 eV. Deviations of the error in BE reported is within ±0.1 eV. These are typical characterisation methods employed for characterisation of thin film and powder materials employed in this thesis.

MB experiments reported in this thesis was performed in a homemade 12 L or 25 L capacity molecular beam instrument (MBI)[50] evacuated with a turbo-molecular drag pump to a base pressure of 2 x 10^{-10} Torr. MBI is equipped with a quadruple mass spectrometer (Pfeiffer, HiQuad^{TM}, QMG 700 with QMA 410, 1-128 amu) for the detection of all the relevant species of the reaction, a sputter ion gun for cleaning the sample surface, a molecular beam doser for the beam generation and a shutter to allow or block the beam at will. More details are available in chapter 2. CZ film deposited on a square Si disk (12 x 12 mm^2) was mounted on niobium sample holder, which is spot-welded with tantalum wires for heating and the temperature is measured by a Cr-Al (K-type) thermocouple, spot-welded to the backside or the periphery of the sample holder. The whole sample assembly can be resistively heated up to 1200 K, and cooled to 125 K with liquid nitrogen, controlled through a

homemade temperature controller. A systematic set of kinetic studies of O_2 adsorption on CZ films was carried out as a function of temperature and CZ composition. Changes observed in the partial pressures of O_2 was then converted into parameters, such as sticking coefficient (s), rate of adsorption, OSC by following a calibration procedure described in our earlier publications.[51,52] Results reported are reproducible within an error margin of 10 %. Results obtained in MBI on thin films are correlated to that of the results obtained on powder CZ materials at ambient pressure, and probably this is the first such report.

3A.2.3 CO Oxidation Reactor Setup

CO oxidation was carried out in a fixed bed glass reactor under atmospheric pressure. Reaction gas mixture which contains 5% CO was passed to the fixed bed reactor containing 250 mg of catalyst.[53] The gas mixture (O_2: CO: N_2=5:1:19) was flowing at a rate of 25 ml/min and calculated GHSV was 6000 $cm^3\ g^{-1}h^{-1}$. Gas flow from the respective N_2, O_2 and CO cylinder was controlled by the mass flow controllers (Brooks). Temperature of the tubular furnace was controlled by using Radix 6400 temperature controller. A 4 cm tubular furnace contains a fixed bed reactor with K-type thermocouple near the catalyst to measure the catalyst bed temperature. Temperature of the reaction was increased at a ramping rate of 2 ºC/min, and it was held at different temperature for 10 min for analysis. Reaction was carried out in a steady state condition. Outflow of the gaseous product mixture was analyzed with the online gas chromatograph equipped with sampling valve and attached with thermal conductivity detector (TCD). CO oxidation reaction was carried out from the room temperature to 300 ºC. Reaction gas mixture (O_2: CO: N_2 = 5:1:19) was allowed to flow at a rate of 25 ml/min in the fixed bed reactor containing catalyst. Catalytic activity was recorded in terms of percent conversion of CO to CO_2 molecule by using the following equation (Eq. 3A.1).

$$X_{CO} = \left(\frac{P_{CO,in} - P_{CO,out}}{P_{CO,in}} \right) \times 100 \qquad (3A.1)$$

3A.3 Results and Discussion

3A.3.1 X-Ray Diffraction Analysis

Different composition of CZ solid solution films formed by sol-gel method was characterised by XRD to determine the structure, and the results are shown in Fig. 3A.1a and 3A.1b for thin and thick films, respectively. Thin films of Ce-rich compositions exhibit diffraction features from selective crystallographic planes and they are indexed to cubic (111), (200), (220) and (311) planes indicating the presence of cubic fluorite structure.[54,55] Appearance of a

broad peak around 2θ = 28.36°, corresponds to (111) plane in CeO_2. However, on Zr^{4+} doping in CeO_2, there is a gradual shift in (111) peak towards higher angle, due to the smaller ionic radius of Zr^{4+} (0.84 Å) than Ce^{4+} (0.97 Å), and a consequent decrease in the cell parameter of the lattice. Smaller size Zr^{4+} compensates the structural stress generated by bigger Ce^{3+} and maintains structure. There is a shift in peak parameter which indicates the formation of solid solution that is clearly shown and indicated in Fig. 3A.1.

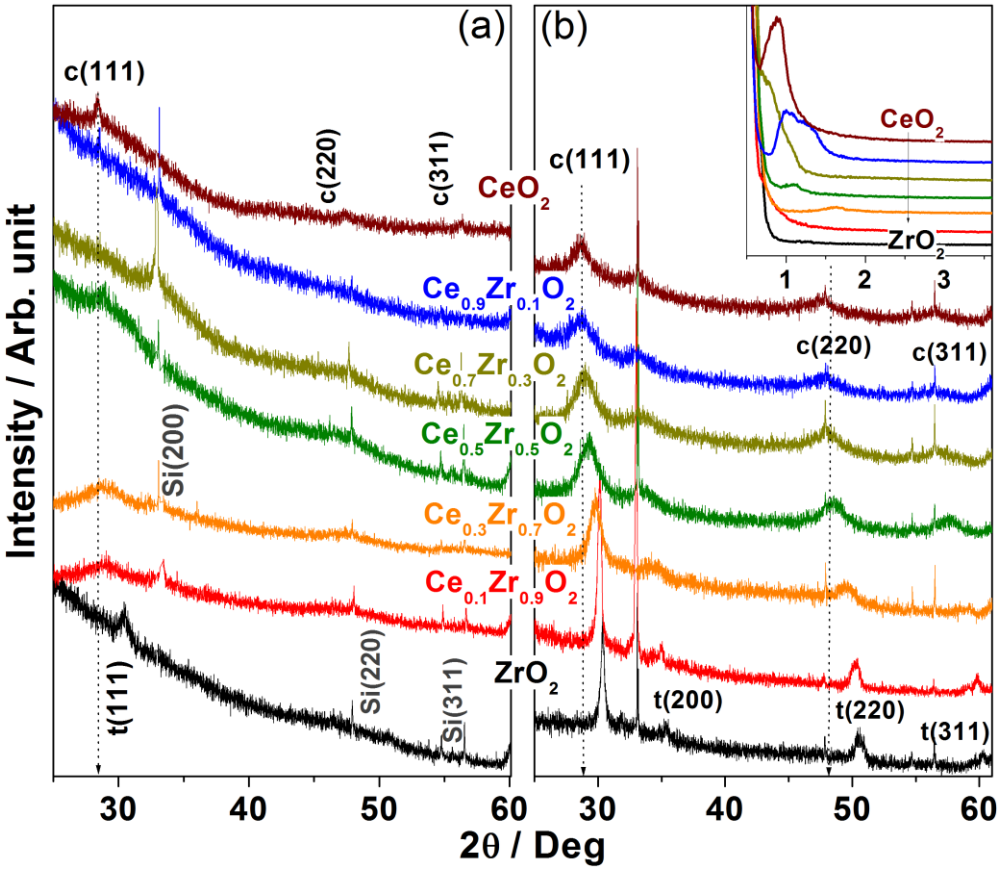

Fig. 3A.1 XRD pattern of $Ce_{1-x}Zr_xO_2$ films with a film thickness of (a) 35-50 nm, and (b) 500-600 nm. Strong diffraction features from Si substrate is intentionally decreased to show the CZ solid-solution features of thin film. Dotted line is shown to indicate the shift in diffraction features of cubic structure and they are guide to eye. Inset in b is shown to indicate the disordered mesoporosity with Ce-rich compositions of CZ powder material. Si features also reiterates that the substrate does not undergo oxidation, even after calcination at 773 K in air atmosphere.

Lattice defects in the fluorite structure of CeO_2 lattice occurs due to doping of Zr^{4+} in CeO_2. Diffraction feature at 2θ = 30.55° corresponds to the tetragonal (111) peak of pure ZrO_2thin film. Sharp and narrow features at 2θ = 33.2, 47.65 and 56.52° corresponds to Si(200), Si(220) and Si(311) planes,respectively.[56] Above Si features appears on all thin and thick films, arises from the substrate Si wafer and it has been employed as internal reference too. It is also to be mentioned that Si remains largely in elemental form, rather than SiO_2, in

spite of calcination at 773 K in air. Thick film (500-600 nm thick) diffraction data is shown in Fig. 1b for comparison as well as confirmation. Indeed a systematic shift in all cubic features ((111), (220) and (311)) towards higher angle with increase in Zr-content is observed. However, predominant tetragonal phase for ZrO_2 was observed. Further, a decrease in full-width at half maximum (FWHM) of all characteristic features is observed with increasing Zr-content indicating an increase in the crystallite size from 5 to 27 nm. A careful comparison of Figs. 3A.1a and 3A.1b suggests the presence of above features ((200) and (311)) and shift to higher angle is also discernible on thin films. Above all, XRD data confirms the solid-solution nature of CZ in thin and thick film forms. Inset in Fig. 3A.1b shows the low angle XRD recorded with thick films. Ce-rich compositions show a single diffraction feature between $2\theta = 0.5$ and 1.5^0 highlight the disordered mesoporosity.[57-59] Zr-rich CZ compositions does not show similar feature, since the surface area is low (see Table 3A.1). Further, similar disordered mesoporous feature was not observed with thin films, due to small amount of material, and broad diffraction features of nanocrystalline material would subsides features due to mesoporosity.

3A.3.2 HRTEM Analysis

CZ thin film was gently dislodged with the help of forceps directly into isopropyl alcohol and sonicated for 1 h and then it was drop casted on the TEM holy grid and the results are shown in Fig. 3A.2a, c and e. HRTEM images recorded on thin films directly prepared on Au-Pt grids are shown in Fig. 3A.2b, d and f. TEM results indicate the mesoporous nature of CeO_2 thin film as well as with Ce-rich compositions (Fig. 3A.2a). This observation may be considered equivalent to "*blessing in disguise*", especially towards bridging the material gap. Mesoporous thin film is a blessing in the sense that real world catalyst microstructure is reproduced in model thin films. Mesoporosity would also allow the diffusion of reactants and products into the porous channels, and further making the case strong to simulate *in situ* reaction conditions encountered in powder/industrial catalysis. Nevertheless, this also makes the fundamental parameter evaluation, like sticking coefficient and surface adsorption capacity, a difficult task, due to the possibility of diffusion of adsorbed species from surface to bulk through mesopores. Indeed a decrease in the thickness of thin films would minimize such diffusion and further efforts are needed in this direction. Porous nature disappears with Zr-rich compositions and it is supported by surface area measurements which are discussed in next segment of characterization for powder catalyst. Porous nature was continued to be observed with CZ films along with nanorod morphology, for Ce-rich compositions and when the film was prepared on Si wafer. Mesoporous nature along with nanorods is observed (Fig.

3A.2b-e) with 10-50 % Zr^{4+} doping. SAED pattern shows that cubic (111) plane is predominant and it is in good correspondence with the XRD pattern displaying the preferred orientation along (111) plane. Both the as-prepared thin film on Au-Pt grid and drop casted film shows (111) plane as the predominant plane; however the nanorod morphology observed

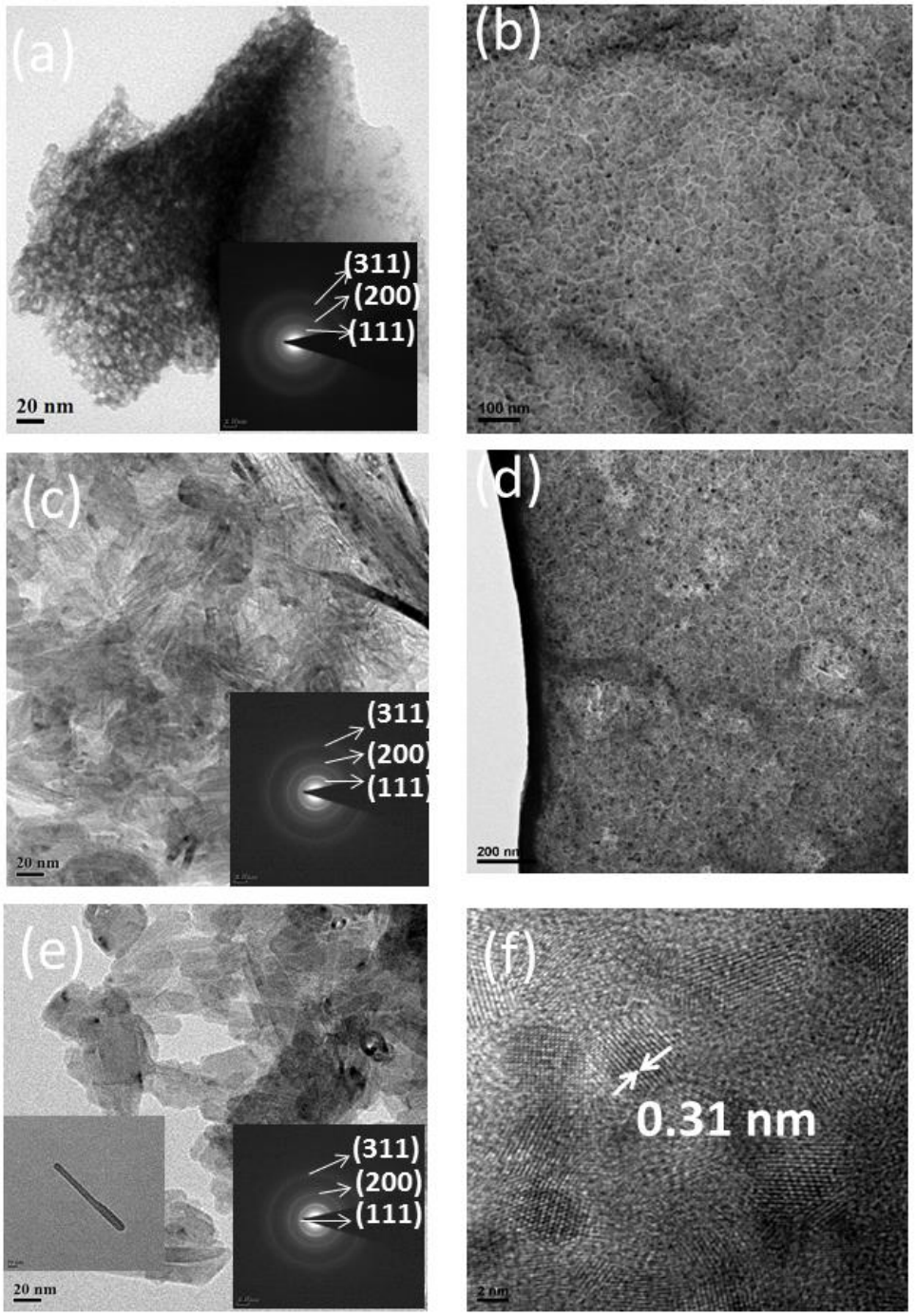

Fig. 3A.2 TEM images of the $Ce_{1-x}Zr_xO_2$ thin films. Images in a, c and e panels were due to sample scraped from Si wafer and drop casted on TEM grid. Images in b, d and f panels were recorded on thin films prepared on Pt-Au grid directly. (a) Disordered mesoporous structure of CeO_2. Homogeneous but porous surface was observed for (b) $Ce_{0.9}Zr_{0.1}O_2$, and (d) $Ce_{0.7}Zr_{0.3}O_2$. Nanorod structure was observed for (c) $Ce_{0.9}Zr_{0.1}O_2$ and (e) $Ce_{0.7}Zr_{0.3}O_2$. A single nanorod is shown in the inset of e. (f) Lattice fringes observed on $Ce_{0.7}Zr_{0.3}O_2$.

on Si wafer indicating the influence of substrate on film growth and particle morphology. Cubic structure associated with Si and Ce-rich compositions is likely to be the determining factor for nanorod morphology. Indeed, overlapping diffraction features of silicon and CZ (Fig. 3A.1) underscore the above point. The interlayer spacing observed between successive planes of (111) from XRD pattern is 0.31 nm, which is very characteristic of CZ solid solution.[60] Indeed HRTEM measurements also directly show the same value for CZ thin films (Fig. 3A.2f) and supporting the XRD results. It is to be underscored that there is a drastic change in the morphology from pure ceria to CZ; however, porosity is observed irrespective of the substrate for Ce-rich compositions.

3A.3.3 Textural Characteristics

Textural characteristics of CZ powder materials were measured by N_2 adsorption-desorption isotherms, and pore-size distribution analysis. The results are shown in Fig. 3A.3 and BET surface area is given in Table 3A.1. It demonstrates an increasing adsorption capacity as well as porosity of thin films with increasing Ce-content. Zr-rich compositions shows exclusive microporous nature with low surface area (<13 m^2/g) and pore diameter of < 2nm. Type IV adsorption isotherms with H2 hysteresis loop is evident for $Ce_{0.5}Zr_{0.5}O_2$ and $Ce_{0.7}Zr_{0.3}O_2$. H3 type hysteresis loop with no saturated adsorption was observed with $Ce_{0.9}Zr_{0.1}O_2$ at P/P_o = 0.8-1 demonstrates the possibility of the significant macropores in $Ce_{0.9}Zr_{0.1}O_2$. Broad pore

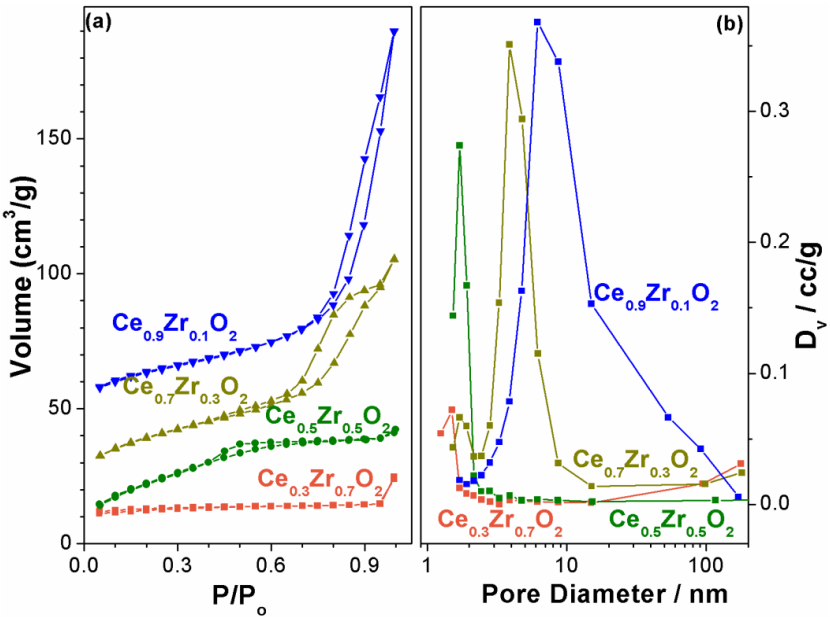

Fig. 3A.3 (a) N_2 adsorption-desorption isotherm measured at 77k, and (b) pore-size distribution measured by BJH method for ceria-zirconia powder materials.

size distribution highlights the presence of predominant mesopores with significant macropores in $Ce_{0.9}Zr_{0.1}O_2$. It is expected that highly porous material is likely to lead to relatively rough surface character than the less porous materials. Increase in porosity of

material with high cerium content makes the surface rough which is also reflected in case of thin film also. The same trend for thin film was also observed for roughness of surface which was found correct with an analysis by XRD and profilometer results. The rough surface of thin film results due to the porous nature of material as was observed by BET surface area analysis of powder sample.

3A.3.4 Thickness and Morphology of $Ce_{1-x}Zr_xO_2$ thin films

Thickness of the films was measured by the profilometer. Although several measurements were made at different areas on various batch thin films, representative results are given in Fig. 3A.4. Profilometer measures the thickness of the films by keeping the substrate Si surface as a reference (denoted by arrows in Fig. 3A.4), and measures the height of the sample on the substrate which is equal to the thickness of the film. Average thicknesses of the film, as observed from Figure 3A.4, are between 35 and 50 nm for all CZ compositions. Surface roughness of the film, as can be seen from Fig. 3A.4 is in the range of 2-30 nm. It has been observed from Figure 3A.4 that as the ceria content of the film increases the roughness of the film also increases. It is to be noted that $Ce_{0.9}Zr_{0.1}O_2$ composition shows similar surface roughness and thickness; this is attributed to highly porous characteristics of Ce-rich compositions as was discussed in above section.

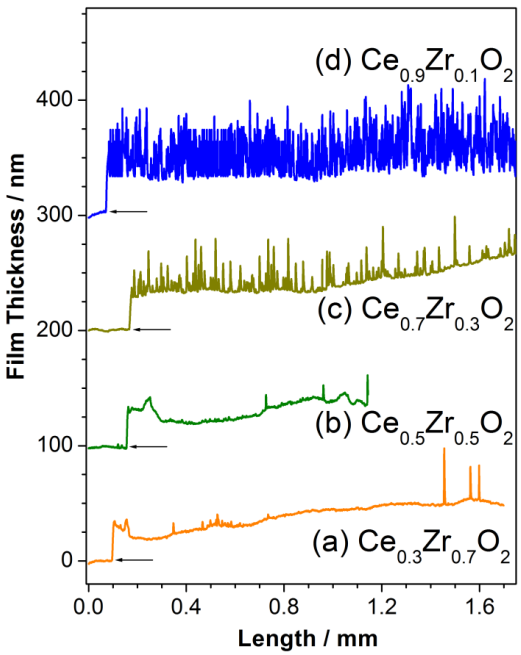

Fig. 3A.4 Thickness of the thin film as measured by profilometer for various compositions. (a) $Ce_{0.3}Zr_{0.7}O_2$, (b) $Ce_{0.5}Zr_{0.5}O_2$, (c) $Ce_{0.7}Zr_{0.3}O_2$, and (d) $Ce_{0.9}Zr_{0.1}O_2$. Surface profiles are vertically shifted for clarity, and the arrow mark indicates the Si-substrate reference level.

Table 3A.1: Surface area, surface and bulk composition and core level binding energy of CZ

Material	Surface Area (m^2/g)	Atom percent			Binding Energy (eV)			Ce/Zr ratio
		O	Ce	Zr	O 1s	Ce $3d_{5/2}$	Zr $3d_{5/2}$	
CeO_2	112	62.3	37.6	0.0	530.2	883.3	--------	---
$Ce_{0.9}Zr_{0.1}O_2$	102	61.6	33.5	4.9	530.2	883.3	182.4	7.60
$Ce_{0.7}Zr_{0.3}O_2$	98	61.8	25.7	12.5	530.3	883.3	182.4	2.20
$Ce_{0.5}Zr_{0.5}O_2$	92	60.1	16.7	23.2	530.4	883.8	182.6	0.94
$Ce_{0.3}Zr_{0.7}O_2$	13	58.1	10.9	31.0	530.5	883.2	182.6	0.43
$Ce_{0.1}Zr_{0.9}O_2$	---	56.1	4.3	39.6	530.5	883.2	182.6	0.02
ZrO_2	---	56.9	0.0	43.1	530.6	--------	182.7	0.00

Surface roughness and profile of CZ films is further examined by the AFM measurements and the results are shown in Fig. 3A.5 for three compositions for large area (5 x 5 μm^2). A glance at AFM images indicates an increase in the Ce-content induces nano-structuring and hence surface roughness of thin films. However, thin film is continuous and no gap between particulate microstructure was observed. Fig. 3A.5 b, d and f, demonstrates that the surface smoothness is nearly uniform throughout the film and in correspondence with the results shown in Fig. 3A.4. Indeed surface profilometer and AFM measurements have been repeated for films prepared in different batches and at different spots. Similar results are reproduced highlighting the reproducibility of the surface texture by sol-gel with spin coating method. Surface profile of Si wafer and a reference single crystal (Ag (111)) are shown in 3A.6. Surface roughness, especially spikes, observed on CZ thin films is partly attributed to that of Si wafer employed in the reported results. Further surface profiles of Ag (111) single crystal underscores a comparable surface quality of thin films reported in this communication.

Increase in surface roughness is attributed, in part, to the increasing porosity of thin films with increasing Ce-content. XRD, TEM, profilometer, AFM, sorption isotherm results (Figs. 3A.1-3A.6) demonstrates the presence of disordered mesoporosity and the same aspect lead to rough surface characteristics in Ce-rich CZ films. It is expected that a porous material lead to rough surface. Nonetheless the present preparation procedure leads to thin film with very low (2 nm) to rough (20-30 nm) surface characteristics; it is also to be underscored that the surface roughness is dependent on material's composition.[35] It is expected, in general, that

such studies would lead to better quality thin films. Atom percent of Ce, Zr and O was measured by EDX and the results are shown in Table 3A.1. EDX analysis demonstrates a linear increase in Zr-content and proportional to that of nominal input content of Zr. However, overall O-content decreases linearly with increasing Zr-content.

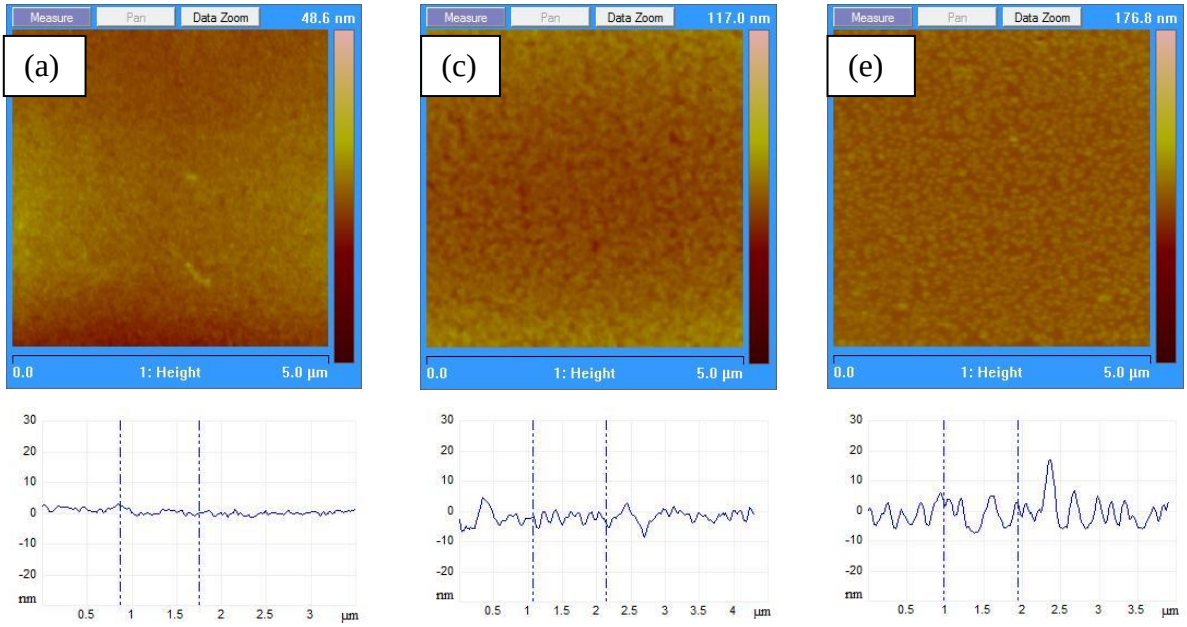

Fig. 3A.5 AFM top view images (top panels) along with the surface roughness profile (bottom panels) of the CZ thin films: (a-b) $Ce_{0.3}Zr_{0.7}O_2$ (c-d) $Ce_{0.5}Zr_{0.5}O_2$, and (e-f) $Ce_{0.7}Zr_{0.3}O_2$.

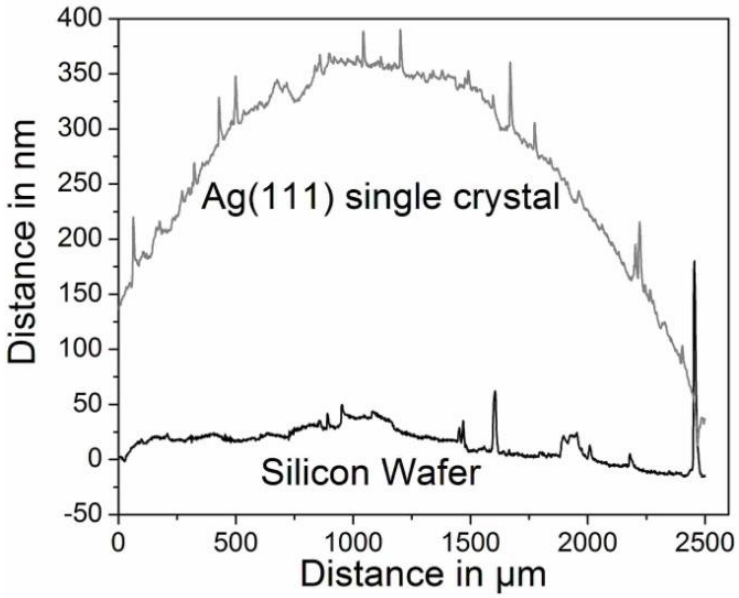

Fig. 3A.6 Surface roughness of the silicon wafer (employed to make thin films in the present communication), and Ag(111) single crystal (from Metal Crystals and Oxides Ltd., Cambridge, UK).

3A.3.5 XPS Analysis

Electronic structure of the CZ thin film and powder materials was analyzed by XPS and the results are shown in Fig. 3A.7. Results for thin film and powders are essentially the same and no significant difference was observed. Binding energy (BE) of O 1s and $3d_{5/2}$ core levels of Ce and Zr are given in Table 3A.1. BE of O 1s core level varies within a small range of 530.2 to 530.6 eV, and corresponds to lattice oxygen in ceria.[61-63] However, a gradual increase in the BE of O 1s from CeO_2 to ZrO_2 through CZ solid solution (Table 3A.1) indicates a change in electronic interaction within CZ lattice. BE for the Zr $3d_{5/2}$ core level in ZrO_2 (Table 3A.1 and Fig. 3A.7a) is observed at 182.7 eV, which is in agreement with the BE of Zr^{4+} reported in literature.[64-65] As the Ce-content increases a shift towards lower BE by 0.3 eV of Zr $3d_{5/2}$ core level is observed with a marginal increase in the FWHM. This indicates a significantly altered electronic environment of Zr upon doping in CeO_2 lattice.

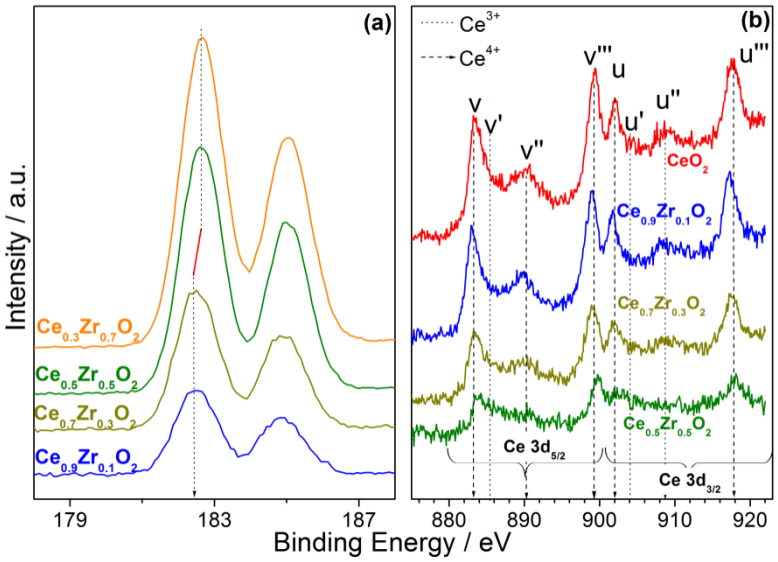

Fig. 3A.7 (a) Zr 3d, and (b) Ce 3d core level features of $Ce_{1-x}Zr_xO_2$ thin films of various compositions.

Ce 3d core level spectra are shown in Fig. 3A.7b for different CZ compositions. Nature of Ce 3d spectrum is very complex. There are two set of spin-orbit multiplets observed for Ce 3d core level which corresponds to Ce $3d_{5/2}$ at 883.4 eV (v), 890.4 eV (v´´) and 899.4 eV (v´´´) and Ce $3d_{3/2}$ at 902 eV (u), 908.6 eV (u´´) and 917.6 eV (u´´´). The doublet v´´´ and u´´´ at BE 899.4 and 917.6 eV corresponds to the Ce(IV) $3d^94f^0$ – O $2p^6$ configuration, doublet v´´/u´´ at BE 890.4 and 908.6 eV corresponds to the Ce(IV) $3d^94f^1$ – O $2p^5$ configuration, and doublet v/u at BE 883.4 and 902 eV corresponds to the Ce(IV) $3d^94f^2$ - O $2p^4$ configuration. However, v´ and u´ features are characteristic of Ce^{3+} oxidation state at 885.5 and 904.2 eV, and corresponds to the Ce(III) $3d^94f^2$ - O$2p^5$ configuration.[66,67]

Interestingly, thin film with 50% Ce content shows considerable broadening of the peak at 883.4 eV (feature v for Ce(IV) $3d^9 4f^1$ – O $2p^5$ configuration) in the XPS than other Ce compositions. This broadening is attributed to the presence of Ce^{3+} at BE 885.5 eV (v´) and its corresponding $3d_{3/2}$ component at 904.0 eV (u´). The formation of Ce^{3+} at high Zr loadings in the thin films is not surprising due to the defects structures (such as oxygen vacancies, Zr^{4+} on surface) present at nano size regimes. Ce 3d peak intensity decreases non-linearly with increasing Zr content underscore a change in surface composition (Table 3A.1); while bulk composition, measured by EDX, shows a linear decrease in Ce content with increasing Zr concentration. Indeed high signal to noise ratio observed for Zr-containing films underscores an increase in Zr-content on the surface.

3A.3.6 Catalytic CO oxidation on Ceria-Zirconia

Powder $Ce_{1-x}Zr_xO_2$ materials prepared by sol-gel method were evaluated for catalytic activity for CO oxidation. CO oxidation activity of four different catalyst compositions are plotted as a function of temperature and shown in Fig. 3A.8. Indeed we made an attempt to measure CO oxidation activity with CZ thin films; due to very small amount of material («1 mg) present in thin film, no significant activity was observed at ambient pressure.

No CO oxidation activity was observed up to 573 K for $Ce_{0.3}Zr_{0.7}O_2$; gradually the CO oxidation to CO_2 increases and about 21 % CO conversion was observed at 673 K. An onset of catalytic activity was observed at 573 K for $Ce_{0.5}Zr_{0.5}O_2$ with CO conversion of about 6.5%. An onset of catalytic activity was observed at lower temperature for other catalyst which depends on the Ce-content present in the catalyst. With increasing Ce (or decreasing Zr) content, CO oxidation activity also increases. 50 % CO conversion to CO_2 was observed at 600 and 555 K with $Ce_{0.7}Zr_{0.3}O_2$ and $Ce_{0.9}Zr_{0.1}O_2$ compositions, respectively. 100 % CO conversion and CO_2 production was observed at 635 K (620 K) for $Ce_{0.9}Zr_{0.1}O_2$ (CeO_2) composition. Catalytic activity reported in Fig. 3A.8 is in good agreement with activity data reported earlier.[68-71] High Zr-content in CZ materials requires high temperature to reach the same extent of CO_2 production (say 10 or 50 %) demonstrating the OSC and oxygen availability for CO oxidation is gradually decreasing. However, it is to be reminded that Zr-containing CZ solid solution largely retains the surface area and OSC even after high temperature treatment (>1000 K); while CeO_2 and less than 20% Zr-containing CZ shows a drastic reduction in surface area and OSC after high temperature treatments.[35,36] These aspects are thoroughly discussed in literature reports and hence not discussed further.

Oxidation catalytic activity of CZ mainly depends upon the redox oscillation between Ce^{4+} and Ce^{3+}. Due to doping of smaller ionic radii Zr^{4+} (0.84 Å) in ceria lattice (Ce^{3+}/Ce^{4+} -

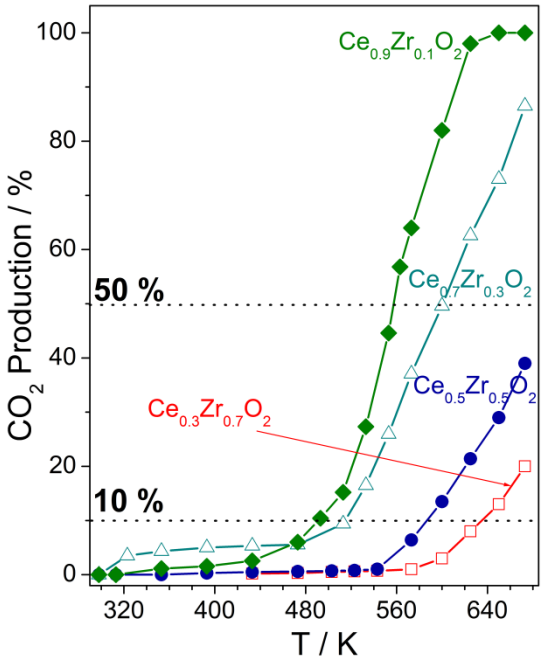

Fig. 3A.8 CO oxidation Catalytic activity by $Ce_{1-x}Zr_xO_2$ catalysts as a function of temperatures. Dotted lines indicating 10 and 50 % CO conversion to CO_2.

1.14 Å/0.97 Å) there is a contraction in the lattice, and hence there is a decrease in bond length Ce-O of Ce-O-Zr.[72] However significant change observed in XRD (Fig. 3A.1) and XPS features (Fig. 3A.7) suggests valence fluctuations towards more Ce^{3+} with increasing Zr^{4+} content to compensate the ionic size changes. OSC represents the ability of the CZ solid solution to shift from Ce^{3+} to Ce^{4+} under oxidizing conditions with charge compensation facilitated via oxygen occupancy. Although all CZ films were subjected to similar calcination treatments, more Ce^{4+} found in Ce-rich films indicates the larger abundance of oxygen for reaction, than Zr-rich compositions, due to higher OSC in the former. Indeed this is an apt system and worth exploring by surface sensitive methods, such as molecular beam methods.[73,74] To investigate on bridging the material gap aspects and an enhanced catalytic activity of ceria rich composition, O_2 adsorption measurements have been made on CZ thin films by MBI as a function of temperature. Interestingly a one to one correlation was found between ambient pressure CO oxidation activity and O_2 adsorption characteristics and OSC measured through MBI.

3A.3.7 Molecular beam study of oxygen adsorption on $Ce_{1-x}Zr_xO_2$ thin films

High surface quality CZ thin films reported in this manuscript has been evaluated for O_2 adsorption and OSC as a function of temperature and the kinetic results are shown in Fig. 3A.9a-c. Fig. 3A.9 shows the O_2 uptake from the O_2 molecular beam with respect to time as a function of temperature on three different CZ compositions. At t = 26 s, the O_2 molecular

beam was turned on into the MBI chamber; however, the shutter is in place prevent any direct interaction between catalyst (thin film) surface with the O_2 molecular beam. At t = 38 s, the shutter was removed to allow the beam to interact directly with catalyst surface. A small amount of adsorption from the background cannot be ruled out between t = 26 and 38 s; however, this is within the error limit of 10 % reported in this manuscript and not taken into account for any calculation. A finite drop in O_2 pressure at t = 38 s demonstrate the adsorption of oxygen on the catalyst surface (Fig. 3A.9a). Initial drop in pressure observed increases with increasing temperature for any given CZ composition. Initial decrease in pressure provides the initial sticking coefficient (s_0) of O_2 on the virgin surface, which will be discussed later. High rate of O_2 adsorption observed at the point of shutter opening decreases with increasing time of exposure at 400 K (Fig. 3A.9a). Indeed this observation indicating the saturation of the surface layers with oxygen coverage (θ_O). Shutter oscillation, by closing and opening the shutter for about 30 s, does not change the O_2 partial pressure supporting the saturation of catalyst surface (not shown). Nonetheless, the amount of O_2 adsorption required to saturate the surface layers increases with increasing temperature. Indeed, O_2 adsorption was observed up to t = 340 s for 600 K. A black trace shown with 600 K data is the reference experiment carried out after the saturation of surface (dark yellow trace); reference experiments are identical to that of the original experiments, except the shutter was not closed throughout the experiment. At 700 K, O_2 adsorption continue to be observed up to t = 400 s, albeit at a lower rate of adsorption, compared to the rate observed at t = 38 s. Surprisingly, initial rate of adsorption at 800 K was observed till the end of the experiment at t = 400 s; a simple comparison between the reference and the original experiments testify this conclusion. Above observation demonstrate an increasing O_2 uptake at high temperatures, and this is attributed to O-diffusion into the subsurface layers and bulk.

It is also to be mentioned that between any two O_2 adsorption experiments, thin film surface was reduced in hydrogen (1 x 10^{-7} Torr at 700 K) for 30 min. This is to regain the original surface characteristics and to avoid any cumulative oxygen coverage due to earlier experiment. It is well known that at high temperatures Mars-van Krevelen (MvK) mechanism prevails in ceria and other oxide-based catalysts, which helps for oxygen diffusion into the bulk under oxidizing conditions.[75-77] Indeed, MvK mechanism[75] is responsible for increasing O_2 uptake at high temperatures. Oxidation of Ce^{3+} to Ce^{4+} requires atomic oxygen on the surface. Increasing amount of O_2 uptake observed at high temperatures is due to the diffusion of oxygen into subsurface layers and bulk, which helps to oxidize Ce^{3+} in those layers to

Ce^{4+}. Highly porous nature associated with Ce-rich compositions of CZ thin film helps for oxygen diffusion into the bulk CZ.

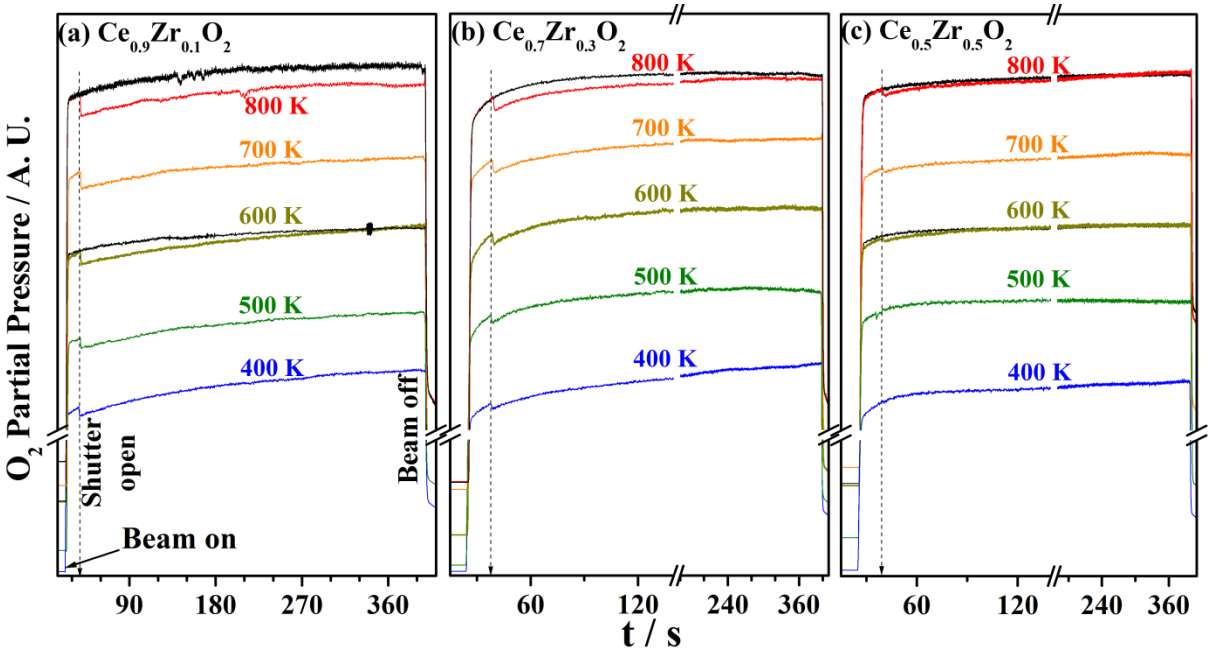

Fig. 3A.9 O_2 uptake as a function of time and temperature on (a) $Ce_{0.9}Zr_{0.1}O_2$, (b) $Ce_{0.7}Zr_{0.3}O_2$, and (c) $Ce_{0.5}Zr_{0.5}O_2$ composition thin films. Reference experiments shown for 600 and 800 K (black line) was carried out after the corresponding O_2 adsorption experiment, but without opening the shutter. Reference experiment data recorded was helpful to calculate the oxygen uptake from the molecular beam and by a simple subtraction with the experimental trace.

A comparison of O_2 uptake observed on $Ce_{0.7}Zr_{0.3}O_2$ (Fig. 3A.9b) and $Ce_{0.5}Zr_{0.5}O_2$ (Fig. 3A.9c) thin films to that of $Ce_{0.9}Zr_{0.1}O_2$ composition (Fig. 3A.9a) demonstrate few important points: With increasing Zr-content, the O_2 uptake decreases at any given temperature. Indeed, marginal amount of O_2 adsorption was observed for $Ce_{0.5}Zr_{0.5}O_2$ up to 600 K suggesting the nature of catalyst and catalyst surface is very different, compared to $Ce_{0.9}Zr_{0.1}O_2$. In addition, the initial rate of O_2 adsorption on virgin surfaces also decreases with increasing Zr-content for any given temperature. Both the above observations is indicating the nature of surface changes from highly oxidizable at high Ce-content to increasingly non-oxidizable (or reducible) with increasing Zr-content. Indeed the textural characteristics of CZ thin films also changes from highly porous for Ce-rich compositions to less-porous material with Zr-rich compositions. A combination of increasingly non-oxidizable and non-porous nature with increasing Zr-content restricts the O_2 adsorption as well as O-diffusion into the sub-surface layers and bulk. Microscopy, profilometer and sorption isotherm results fully support the above points (Figs. 3A.2-3A.6), and indicate the porosity contributes dominantly in the Ce-rich compositions.

From Fig. 3A.9 we can calculate extent of O_2 adsorption at various temperatures. Along with O_2 adsorption experiments, very similar reference measurements were also made (see 800 and 600 K data sets in Fig. 3A.9) in which shutter was in closed position throughout the experiment and hence direct interaction between O_2 MB and sample surface is fully avoided. Reference experiments were carried out for all temperatures after surface saturation. Figure 3A.10 demonstrates the procedure adopted to calculate different quantities, such as total oxygen uptake, s and initial s (s_0). Procedure reported by Liu et al[78] also leads to very similar results; however, we adopted the subtraction method with reference experiment, due to simple procedure. It is to be noted that this method may not be applicable to molecules which adsorbs strongly on the chamber walls, such as NH_3, H_2O. A simple subtraction between reference and direct adsorption experiments (Fig. 3A.10a) provides the extent of adsorption and rate of oxygen adsorption as a function of time (Fig. 3A.10b). Integration of the above area provides the total oxygen uptake or OSC (θ_{OSC}) (Fig. 3A.10c). A plot of cumulative sum of θ_O and time indicates the first order diffusion of O atoms into the subsurfaces/bulk.

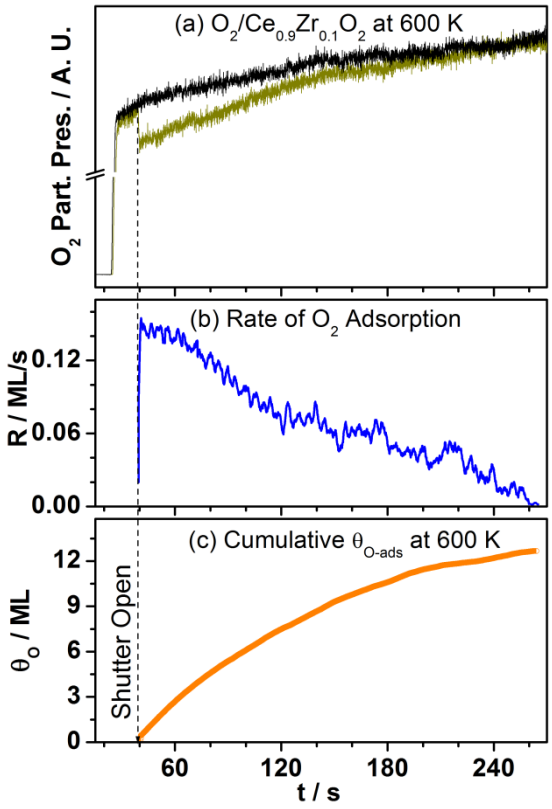

Fig. 3A.**10** (a) O_2 uptake from the molecular beam and reference experiment, (b) rate of O_2 adsorption, and (c)cumulative oxygen coverage as a function of oxygen exposure time measured from the data given in panel a for $Ce_{0.9}Zr_{0.1}O_2$ thin film.

Processed data shown in Fig. 3A.10 for $Ce_{0.9}Zr_{0.1}O_2$ at 600 K demonstrates the rate of adsorption; large extent of adsorption at the time of shutter opening indicating a high s.

Similar rate of adsorption was maintained for about 35 s, after shutter opening and this is indicated by similar s observed up to t = 75 s.

Indeed, this trend fully supports the precursor mediated adsorption,[79-80] and the same trend was observed at other temperatures too. However, adsorption rate begins to decline at t > 80 s and a gradual decrease was observed till t = 260 s, and no further net adsorption was observed at higher time. Total oxygen adsorption calculated was equal to 12±1 ML, which is much higher than 1 ML, if adsorption was restricted only to top surface layer, indicating three different possibilities: (a) diffusion of oxygen into the subsurface layers, as well as (b) large number of surface atoms exposed to molecular beam from external and internal (pores) surfaces, due to highly porous nature of $Ce_{0.9}Zr_{0.1}O_2$; (c) Bulk diffusion of oxygen atoms occurs after a and/or b. In contrast to bulk CeO_2 single crystals, which corresponds to θ_O = 0.25 ML, about 1.5 order of magnitude higher θ_O observed experimentally at 600 K on $Ce_{0.9}Zr_{0.1}O_2$ fully supports the porous nature as well as oxygen diffusion into subsurface layers. Precursor mechanism suggested indicates the surface adsorption at the beginning of the experiment (t = 38-70 s), and simultaneous diffusion of oxygen into subsurface layers. A careful look at the decrease in the rate of oxygen adsorption at later time (t > 80 s) hints the saturation of surface layers, which makes the diffusion difficult. It is also to be remembered that the pre-reduction treatment in H_2 for 30 min at 700 K, before any O_2 adsorption experiment. Pre-reduction treatment creates oxygen-vacancy sites and this could be another factor for oxygen adsorption; however, this factor remains the same for all experiments. Oxygen adsorption measured at 600 K on $Ce_{0.7}Zr_{0.3}O_2$ and$Ce_{0.5}Zr_{0.5}O_2$ compositions are also processed the same manner and the results are given in Fig. 3A.11 A notable decrease in cumulative oxygen coverage by one (two) order of magnitude from $Ce_{0.9}Zr_{0.1}O_2$ to $Ce_{0.7}Zr_{0.3}O_2$ ($Ce_{0.5}Zr_{0.5}O_2$) demonstrates the role of porosity in fast diffusion of oxygen atoms into the bulk, which facilitates MvK mechanism.

A detailed analysis of data at all temperatures demonstrates the contribution of both factors (oxygen diffusion and porosity) at all temperatures, but to a different extent as it depends on the CZ composition. Cumulative θ_O and s is shown in Fig. 3A.12 for $Ce_{0.9}Zr_{0.1}O_2$ thin film to complement the data shown in Fig. 3A.10. Similar s value observed for the first three monolayers of θ_O highlights the precursor mediated adsorption followed by diffusion of oxygen atoms into the subsurface layers through porous network. Due to the large depth of irregular and vertical porous layers of about 30 nm (Fig. 3A.4), it would be difficult to quantify the depth of oxygen diffusion. Nonetheless, oxygen diffusion is likely to occur till the regular layers, which begins below the above porous layers. Peculiar and random

oscillations in s were observed from virgin surfaces to oxygen saturated CZ layers. Extent of oscillation decreases with increasing smoothness or surface quality (Fig. 3A.11) hinting the oscillation is due to porous nature of the thin films, and this requires further investigation.

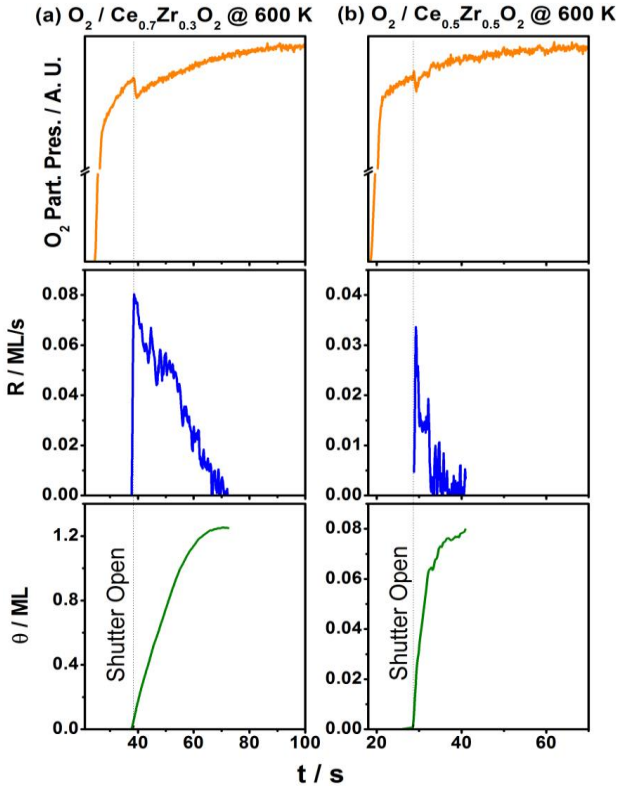

Fig. 3A.11 O_2 uptake from the molecular beam and reference experiment, rate of adsorption, and cumulative oxygen coverage as a function of oxygen exposure time measured from the data given in top panels for (a) $Ce_{0.7}Zr_{0.3}O_2$, and (b) $Ce_{0.5}Zr_{0.5}O_2$ thin films. Note a decrease in one (two) order of magnitude oxygen coverage from $Ce_{0.9}Zr_{0.1}O_2$ to $Ce_{0.7}Zr_{0.3}O_2$ ($Ce_{0.5}Zr_{0.5}O_2$).

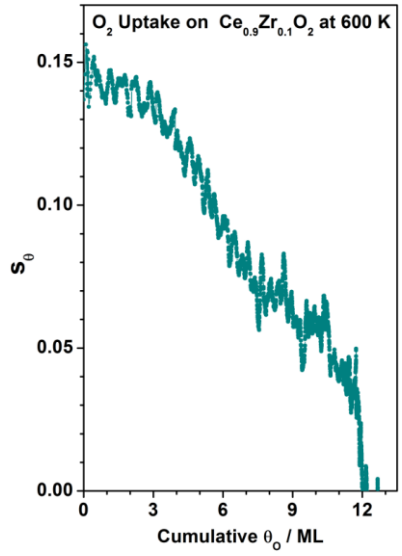

Fig. 3A.12 Sticking coefficient with respect to cumulative oxygen coverage from O_2 adsorption on $Ce_{0.9}Zr_{0.1}O_2$ thin film at 600 K, which is calculated from the data shown in Fig. 3A.10.

Fig. 3A.13 shows the extent of O_2 adsorption on $Ce_{0.9}Zr_{0.1}O_2$ film at various temperatures, by following the procedure explained in Fig. 3A.10. We consider the results shown for 400 K as a reference experiment for adsorption exclusively on surfaces and with no oxygen diffusion, especially in view of zero oxidation activity at 400 K. The results shown in Fig. 3A.13 explain few important points and they are listed below: (a) A gradual increase in the oxygen adsorption or oxygen coverage (by integrating the dotted line area) at higher temperatures suggesting the onset of oxygen diffusion above 400 K. (b) Rate of oxygen adsorption on virgin surfaces, at the time of shutter removal at t = 35 s, gradually increases with temperature suggesting an increase in s_0 as well as s at higher time. (c) Initial rate of adsorption was gradually extended for higher time as well, and the same increases with increasing temperature. Indeed, 800 K results shows the similar rate of adsorption from t = 35 to 240 s; even at t > 240 s only a marginal decline in oxygen adsorption was recorded. This fully supports the precursor mediated adsorption followed by oxygen diffusion into subsurface/bulk layers. (d) High value of s and rate of adsorption at high temperatures is due to oxygen diffusion, which is fully supported by point c. Some peculiar and random signal fluctuation was observed in the processed data, especially at high temperatures, is attributed to an increasing diffusion into subsurface layers, which is indicated for Fig. 3A.12. Further a significant to large difference in substrate temperature and O_2 molecular beam at ambient temperature also could be partially responsible for fluctuations.

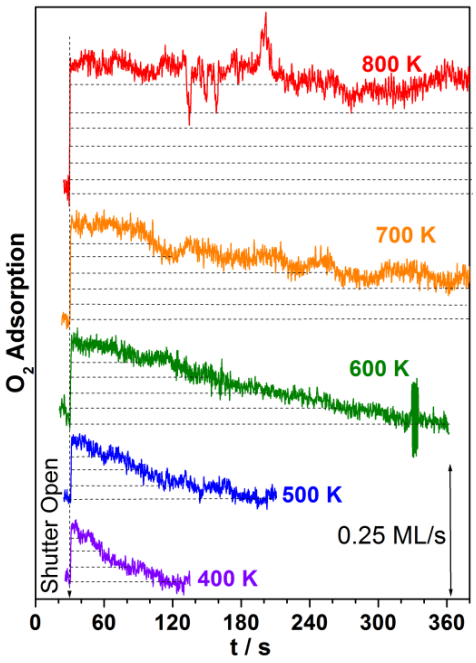

Fig. 3A.13 Rate of O_2 adsorption on $Ce_{0.9}Zr_{0.1}O_2$ thin film as a function of time and temperature, by following the procedure explained in Fig. 3A.7. Oxygen coverage was obtained by integrating the area covered by dotted lines.

s_0, and θ_{OSC} were calculated from the experimental data shown in Fig. 3A.14 for three CZ compositions. s_0 increases linearly between 400 and 800 K for all three CZ compositions. Although high s_0 was observed with Ce-rich composition, all three CZ compositions shows a similar increase in s_0 over the temperature range. This indicates a possibility of large number of oxygen vacancies on Ce-rich surfaces than Zr-rich compositions; porous nature of Ce-rich surfaces also helps for higher s_0. θ_{OSC} calculated by integrating area under O_2 adsorption curve (Fig.3A.14b) shows some interesting insights of oxygen interaction with CZ surfaces. θ_{OSC} increases linearly up to 600 K, and then it increases exponentially; indeed 700 and 800 K data points measured from Fig. 3A.9a shows that the surfaces are not completely saturated for $Ce_{0.9}Zr_{0.1}O_2$, while other compositions shows saturation within the time frame of the experiment. Highly porous textural characteristics associated with $Ce_{0.9}Zr_{0.1}O_2$, indeed, accelerates oxygen diffusion to a predominant level. Increasing Zr-content changes towards less porous nature and making it more dense material with lower rate of oxygen diffusion. In fact, high porous character with Ce-rich composition is the main reason for its sintering behavior at high temperatures. Insignificant OSC observed with high Zr-content (0.3 and 0.5) surfaces up to 600 K reiterates that these surfaces are less amenable for oxidation. Comparable OSC observed between $Ce_{0.9}Zr_{0.1}O_2$ and $Ce_{0.5}Zr_{0.5}O_2$ at 500 and 800 K, respectively, implies the nature of surface changes from oxidizable to non-oxidizable.

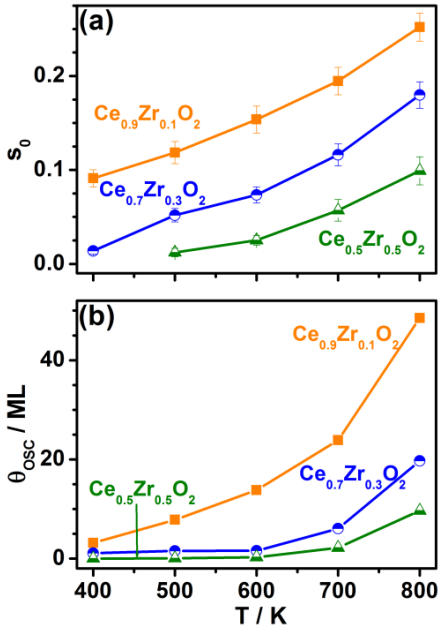

Fig. 3.14 a) s_0 measured for O_2 on different composition of $Ce_{1-x}Zr_xO_2$ thin film as a function of temperature. b) θ_{OSC} calculated for various $Ce_{1-x}Zr_xO_2$ thin films as a function of temperature. 700 and 800 K data points shown for $Ce_{0.9}Zr_{0.1}O_2$ is not fully saturated with oxygen atoms and it should be considered as the θ_{OSC} in the time-frame of experiment, which is about 365 s.

It is also to be mentioned that Si wafer is vulnerable for oxidation at high temperatures. Our efforts to explore silicon oxidation state by XPS were not successful, mainly due to limited probing depth (< 10 nm). Nonetheless, porous layers and underlying 30-40 nm thick layers of CZ would predominantly adsorb oxygen and hence the probability of silicon oxidation is small under the present measurement conditions. Further, XRD results shows high intensity Si features (Fig. 3A.1), suggesting the possibility of Si oxidation is limited. However, we do not want to rule out the oxidation of Si layers by consuming few percent of oxygen measured in MBI experiments (Fig. 3A.14b), especially at 700-800 K, due to continuous oxygen adsorption (Fig. 3A.13). Saturation of oxygen adsorption ≤ 600 K rules out the possibility of oxygen diffusion up to the Si substrate.

A comparison between CO oxidation activity, measured on powder catalyst at ambient pressure (Fig. 3A.8), and θ_{OSC}, measured on thin film at high vacuum (Fig. 3A.14b) demonstrates a good correlation between them. As θ_{OSC} increases, oxidation activity also increases. Early onset of CO oxidation (10 % conversion) observed at 490 K, 50 and 100 % CO conversion correlates well with θ_{OSC} observed at 500, 555 and 600 K, respectively, for $Ce_{0.9}Zr_{0.1}O_2$. Although OSC was found to increase at higher temperature, it is to be noted that the CO oxidation was carried out at ambient pressure, which is 8-9 orders of magnitude higher than the pressure in MB experimental conditions. 100 % CO oxidation observed at 600 K suggests an enhancement in OSC at higher pressure and hence an increase in oxidation activity. Indeed, same reason holds good for other compositions too. For eg. $Ce_{0.7}Zr_{0.3}O_2$ shows insignificant OSC at 600 K, whereas in powder form it shows 50 % CO oxidation activity around the same temperature. Onset of catalytic activity for $Ce_{0.5}Zr_{0.5}O_2$ was observed at 573 K with little conversion of 6.5 % is well correlated with O_2 uptake results as there is marginal O_2 adsorption takes place at 600 K and below this temperature generally no O_2 adsorption takes place as was observed from Figs. 3A.9c and 3A.14b.

3A.4 Conclusion

Uniform nanocrystalline ceria-zirconia (CZ) thin film was prepared by sol-gel synthesis and spin coating combination. Above combination is a potential method to prepare the film in a nano thick regime with high surface quality and uniform morphology over a large area. The profilometer result confirms the thickness of the film in nano-regime. Uniform and high quality surface characteristics were measured and corroborated by several methods.

Molecular beam studies have been carried out on CZ thin films under ideal surface science conditions and it provides the fundamental and necessary catalytic properties, such as OSC, oxygen sticking coefficient on thin film surfaces. An increase in OSC along with

oxygen sticking coefficient with increase in Ce-content in the CZ film was observed. Highly porous nature of Ce-rich CZ film is partly responsible for the above observations. CO oxidation catalytic activity measured at ambient pressure on powder CZ materials and found that the most active catalyst for CO oxidation is $Ce_{0.9}Zr_{0.1}O_2$. Indeed, a good correlation exists between the oxygen sticking coefficient, OSC measured on CZ thin films in molecular beam instrument at high vacuum, and CO oxidation activity measured on CZ powder materials at ambient pressure. These positive aspects suggests the potential nature of the method to bridge the disconnect to a significant extent between ideal surface science and industrial catalysis conditions. However, many other catalyst systems for different reactions needs to be evaluated to fully bridge the material gap. It is also to be mentioned that CO oxidation at ambient pressure on thin films are not successful due to very small amount of CZ material present on the Si-wafer.

A combination of high quality thin films with real world catalyst features, such as mesoporosity, reported in this communication opens up a possible potential synthesis method to bridge the material gap. Although the textural characteristic changes drastically from Ce-rich to Zr-rich compositions of CZ materials, it also helps to investigate and confirm the oxygen diffusion into the subsurfaces and bulk of CZ. In fact this helps to ascertain the prevalence of MvK mechanism in CZ materials. It is worth exploring the synthesis method reported herewith to prepare different catalyst materials and evaluate the same under *operando* conditions to bridge both material gap and pressure gap. This is likely to lead to a better understanding of heterogeneous catalysis.

3A.5 References

(1) G. A. Somorjai, J. Y. Park: *Chem. Soc. Rev.* **2008**, *37*, 2155.

(2) J. Libuda, H. J. Freund, *Surf. Sci. Rep.* **2005**, *57*, 157.

(3) F. Zaera, *J. Phys. Chem. B,* **2002**, *106*, 4043.

(4) M. Bowker, *Phys. Chem. Chem. Phys.* **2007**, *9*, 3514.

(5) H. J. Freund, H. Kuhlenbeck, J. Libuda, G. Rupprechter, M. Baumer, H. Hamann, *Top. Catal.* **2001**, *15*, 201.

(6) C. S. Gopinath and F. Zaera, *J. Phys. Chem. B* **2000**, *104*, 3194.

(7) V. M. Baumer and H. J. Freund, *Prog. Surf. Sci.* **1999**, *61*, 127.

(8) S. Velu, K. Suzuki, M. Vijayaraj, S. Barman, C. S. Gopinath, *Appl. Catal.* B **2005**, *55*, 287.

(9) C. P. Vinod, *Catal. Today* **2010**, *154*, 113.

(10) S. Velu, K. Suzuki, C. S. Gopinath, *J. Phys. Chem.* B **2002**, *106*, 12737.

(11) T. Mathew, M. Vijayaraj, S. Pai, B. B. Tope, S. G. Hegde, B. S. Rao, C. S. Gopinath, *J. Catal.* **2004**, *227*, 175.

(12) V. Subramanian, E. S. Gnanakumar, D. W. Jeong, W. B. Han, C. S. Gopinath, H. S. Roh, *Chem. Commun.* **2013**, *49*, 11257.

(13) E. S. Gnanakumar, K. S. Thushara, D. S. Bhange, R. Mathew, T. G. Ajithkumar, P. R. Rajamohanan, S. Bhaduri, C. S. Gopinath, *Dalton Trans.* **2011**, *40*, 10936.

(14) V. Johanek, S. Schauermann, M. Laurin, C. S. Gopinath, J. Libuda, H. J. Freund, *J. Phys. Chem. B* **2004,** *108*, 14244.

(15) S. Nagarajan, K. Thirunavukkarasu, C. S. Gopinath, J. Counsell, L. Gilbert, M. Bowker, *J. Phys. Chem.* C **2009**, *113*, 9814.

(16) F. Zaera, C. S. Gopinath, *J. Chem. Phys.* **2002**, *116*, 1128.

(17) M. Salmeron, R. Schlögl, *Surf. Sci. Rep.* **2008**, *63*, 169.

(18) C. S. Gopinath, K. Roy, S. Nagarajan, *ChemCatChem* **2015**, *7*, 588.

(19) K. Roy, R. Jain, C. S. Gopinath, *ACS Catal*. **2014**, *4*, 1801.

(20) R. Jain, A. Dubey, M. K. Ghosalya, C. S. Gopinath, *Catal. Sci. Technol.* (DOI: 10.1039/c5cy01428j)

(21) A. Cavallaro, F. Sandiumenge, J. Gazquez, T. Puig, X. Obradors, J. Arbiol, H. C. Freyhardt, *Adv. Funct. Mater.* **2006**, *16*, 1363.

(22) P. L. J. Gunter, J. W. Niemantsverdriet, F. H. Ribeiro, G. A. Somorjai, *Catal. Rev. Sci. Eng.* **1997**, *39*, 77.

(23) T. P. S. Clair, D. W. Goodman, *Top. Catal.* **2000**, *13*, 5.

(24) J. Loos, P. C. Thüne, J. W. Niemantsverdriet, P. J. Lemstra, *Macromol.* **1999**, *32*, 8910.

(25) A. M. Saib, A. Borgna, J. V. D. Loosdrecht, P. J. V. Berge, J. W. Niemantsverdriet, *J. Phys. Chem.* B **2006**, *110*, 8657.

(26) C. J. Brinker, G. C. Frye, A. J. Hurd, C. S. Ashley, *Thin Solid Films* **1991**, *201*, 97.

(27) T. J. Kirk, J. Winnick, *J. Electrochem. Soc.* **1993**, *140*, 3494.

(28) J. H. Shim, C. C. Chao, H. Huang, F. B. Prinz, *Chem. Mater.* **2007**, *19*, 3850.

(29) D. Beckel, A. Bieberle-Hutter, A. Harvey, A. Infortuna, U. P. Muecke, M. Prestat, J. L. M. Rupp, L. J. Gauckler, *J. Power Sour.* **2007**, *173*, 325.

(30) M. Bowker, *Chem. Soc. Rev.* **2008**, *37*, 2204.

(31) E. S. Gnanakumar, J. C. John, T. Raja, C. S. Gopinath, *J. Nanosci. Nanotech.* **2013**, *13*, 2682.

(32) G. Liu, J. A. Rodriguez, Z. Chang, J. Hrbek, C. H. F. Peden, *J. Phys. Chem. B* **2004**, *108*, 2931.

(33) J. A. Rodriguez, T. Jirsak, A. Freitag, J. C. Hanson, J. Z. Larese, S. Chaturvedi, *Catal. Lett.* **1999**, *62*, 113.

(34) J. Kaspar, P. Fornasiero, M. Graziani, *Catal. Today* **1999**, *50*, 285.

(35) M. Sugiura, *Catal. Survey Asia* **2003**, *7*, 77.

(36) E. Mamontov, T. Egami, R. Brenzy, M. Koranne, S. Tyagi, *J. Phys. Chem.* B **2000**, *104*, 11110.

(37) P. Fornasiero, R. D. Monte, G. R. Rao, J. Kaspar, S. Meriani, *J. Catal.* **1995**, *151*, 168.

(38) T. Staudt, Y. Lykhach, L. Hammer, M. A. Schneider, V. Matoline, J. Libuda, *Surf. Sci.* **2009**, *603*, 3382.

(39) N. Ozer, *Solar Energy Mater. Solar Cells* **2001**, *68*, 391.

(40) S. Balasubramanian, C. S. Gopinath, S. Subramanian, N. Balasubramanian, *Semicond. Sci. Technol.* **1994**, *9*, 1604.

(41) M. Saini, K. Vivekanand, P. Poddar, K. V. G. K. Murty, K. S. Thushara, C. S. Gopinath, *Int. J. Nanotech.* **2010**, *7*, 919.

(42) D. G. Kulkarni, A. V. Murugan, A. K. Viswanath, C. S. Gopinath, *J. Nanosci. Nanotech.* **2009**, *9*, 371.

(43) P. Fornasiero, G. Balducci, R. D. Monte, J. Kaspar, V. Sergo, G. Gubitosa, *J. Catal.* **1996**, *164*, 173.

(44) A. Dubey, Sadhu K. Kolekar, C. S. Gopinath, *ChemCatChem***2016**, DOI: 10.1002/cctc.201600365.

(45) D. W. Schubert, T. Dunkel, *Mat. Res. Innovation* **2003**, *7*, 314.

(46) T. Mathew, K. Sivaranjani, E. S. Gnanakumar, Y. Yamada, T. Kobayashi, C. S. Gopinath, *J. Mater. Chem.* **2012**, *22*, 13484.

(47) M. Mapa, K. Sivaranjani, D. S. Bhange, B. Saha, P. Chakraborty, A. K. Viswanath, C. S. Gopinath, *Chem. Mater.* **2010**, *22*, 565.

(48) K. Roy, C. P. Vinod, C. S. Gopinath, *J. Phys. Chem.* C **2013**, *117*, 4717.

(49) K. Roy, C. S. Gopinath, *Anal. Chem.* **2014**, *86*, 3683.

(50) K. Thirunavukkarasu, C. S. Gopinath, *Catal. Lett.* **2007**, *119*, 50.

(51) K. Thirunavukkarasu, K. Thirumoorthy, J. Libuda, C. S. Gopinath, *J. Phys. Chem. B*, **2005**, *109*, 13272.

(52) K. Thirunavukkarasu, K. Thirumoorthy, J. Libuda, C. S. Gopinath, *J. Phys. Chem. B* **2005**, *109*, 13283.

(53) A. C. Sunilsekhar, K. Sivaranjani, C. S. Gopinath, C. P. Vinod, *Catal. Today*, **2012**, *198*, 92.

(54) B. Murugan, A. V. Ramaswamy, D. Srinivas, C. S. Gopinath,V. Ramaswamy, *Chem. Mater.* **2005**, *17*, 3983.

(55) C. Liang, J. Qiu, Z. Li, C. Li, *Nanotech.* **2004**, *15*, 843.

(56) K. N. Chappanda, Y. R. Smith, M. Misra, S. K. Mohanty, *Nanotech.* **2012**, *23*, 385601.

(57) K. Sivaranjani, A. Verma, C. S. Gopinath, *Green Chem.* **2012**, *14*, 461.

(58) K. Sivaranjani, C. S. Gopinath, *J. Mater. Chem*. **2011**, *21*, 2639.

(59) K. Sivaranjani, S. Agarkar, S. B. Ogale, C. S. Gopinath, *J. Phys. Chem. C* **2012**, *116*, 2581.

(60) J. P. Winterstein, J. Basu, A. Herzing, I. A. Anderson, C. B. Carter, *Microsc. Microanal.* **2008**, *14*, 280.

(61) E. Paparazzo, G. M. Ingo, N. Zacchetti, *J. Vac. Sci. Tech. A.* **1991**, *9*, 1416.

(62) A. Pfau, K. D. Schierbaum, *Surf. Sci*. **1994**, *321*, 71.

(63) A. Galtayries, R. Sporken, J. Riga, G. Blanchard, R. Caudano, *J. Elect. Spect. Relat. Phenom*. **1998**, *88-91*, 951.

(64) D. R. Mullins, S. H. Overbury, D. R. Huntley, *Surf. Sci.* **1998**, *409*, 307.

(65) S. Velu, K. Suzuki, C. S. Gopinath, H. Yoshida, T. Hattori, *Phys. Chem. Chem. Phys.* **2002**, *4*, 1990.

(66) E. S. Gnanakumar, J. M. Naik, M. Manikandan, T. Raja, C. S. Gopinath, *ChemCatChem* **2014**, *6*, 3116.

(67) T. Rajesh, A. K. Rajarajan, C. S. Gopinath, R. Nandini Devi, *J. Phys. Chem. C* **2012**, *116*, 9526.

(68) L. Q. F. Liu, L. Zhao, Y. Ma, J. Yao, *Appl. Surf. Sci*. **2006**, *252*, 4931.

(69) B. Murugan, D. Srinivas, C. S. Gopinath, V. Ramaswamy, A. V. Ramaswamy, *ActaMater.* **2008**, *56*, 1461.

(70) P. Bharali, P. Saikia, B. M. Reddy, *Catal. Sci. Technol*. **2012**, *2*, 931.

(71) M. Manzoli, R. Di Monte, F. Boccuzzi, S. Coluccia, J. Kašpar, *Appl. Catal. B: Environ.* **2005**, *61*, 192.

(72) F. Zhang, C-H. Chen, J. M. Raitano, *J. Appl. Phys.* **2006**, *99*, 084313.

(73) S. Nagarajan, K. Thirunavukkarasu, C. S. Gopinath, *J. Phys. Chem. C* **2009**, *113*, 7385.

(74) S. Nagarajan, K. Thirunavukkarasu, C. S. Gopinath, J. Counsell, L. Gilbert, M. Bowker, *J. Phys. Chem.* C **2009**, *113*, 9814.

(75) P. Mars, D. W. van Krevelen, *Chem. Eng. Sci.* **1954**, *3*, 41.

(76) M. A. Vannice, *Catal. Today*, **2007**, *123*, 18.

(77) S. S. Negi, A. T. Venugopalan, T. Raja, A. P. Singh, C. S. Gopinath, *RSC Adv*.**2014**, *4*, 57087.

(78) J. Liu, M. Xu, T. Nordmeyer, F. Zaera, *J. Phys. Chem.* **1995**, *99*, 6167.

(79) C. S. Gopinath, F. Zaera, *J. Catal.* **2001**, *200***,** 270.

(80) S. Nagarajan, K. Thirunavukkarasu, C. S. Gopinath, S. D. Prasad, *J. Phys. Chem. C* **2011**, *115*, 15487.

Chapter 3B – C-H Activation of Methane to Formaldehyde on $Ce_{1-x}Zr_xO_2$ Thin films.

$Ce_{1-x}Zr_xO_2$ (ceria-zirconia - CZ) thin films were prepared by a combination of sol-gel and spin coating method and evaluated for C-H activation of methane in a molecular beam setup. C-H activation of methane begins at 950 K, and Ce-rich CZ composition displays high selectivity (4-12 %) to partially oxidized formaldehyde.10-12 % selectivity towards HCHO was observed with methane-rich CH_4:O_2 reactants compositions at 1050 K. Low contact time conditions, prevalent under molecular beam experimental conditions, could be a possible reason for HCHO formation. While combustion products were observed instantly upon shining reactants mixture on CZ surfaces, up to 20 s delay was observed before the start of formaldehyde generation underscores its predominant contribution towards the rate determining step and diffusion controlled nature. Kinetic results also indicate the necessity of reduction sites for HCHO generation.

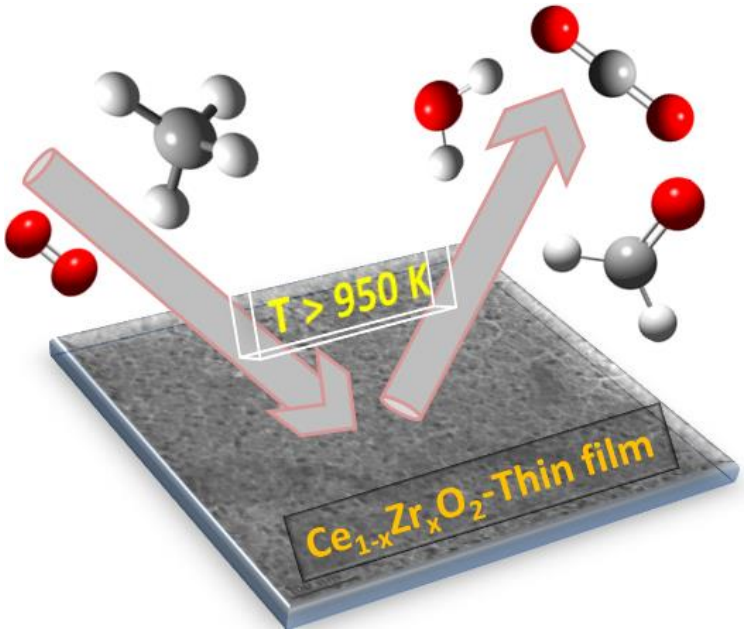

3B.1 Introduction

Selective conversion of methane to oxygenates, such as formaldehyde, is an important reaction to exploit natural gas reserves. Formaldehyde is the simplest aldehyde which is an important precursor for many useful chemical compounds. The direct and selective oxidation of methane to oxygenates is very difficult process as it requires high temperature (~1000 K and above) for the activation of C-H bond.[1-3] In the past few decades many efforts have been made to prepare active catalysts for methane to oxygenates with molecular oxygen.[4-7]Despite the serious efforts, low yield and selectivity was observed.[8,9]Direct oxidation of methane to formaldehyde is an energy efficient method as it avoids energy consumption for conversion of methane to syngas through steam reforming process, which is the initial step for production of formaldehyde.[10,11] Activation of C-H bond occurs on ceria-zirconia (CZ) catalyst with an activation energy of 439 kJ/mol. HCHO selectivity is very low as it is thermodynamically unstable and it further oxidizes to CO_2at high temperatures, (Eqns. 1 and 2), which leads to low selectivity.[12-14]

$CH_4 + O_2 \longrightarrow HCHO + H_2O$ $\Delta H^o_{298} = -319 kJmol^{-1}$ (3B.1)

$HCHO + O_2 \longrightarrow CO_2 + H_2O$ $\Delta H^o_{298} = -571 kJmol^{-1}$ (3B.2)

One of the main problems is the high contact time prevalent in the fixed bed reactors being widely employed for methane oxidation. It is generally around 1 s for methane oxidation in fixed bed reactors.[1-7] Probably the best activity reported so far is with monomeric or isolated vanadium supported on mesoporous silica by Nguyen et al[15] at very high GHSV (80000 to 740000 L/kg_{cat} h) or low contact time with methane conversion up to 6 % and HCHO selectivity between 57-93 %.It is also well known that changes in contact time influence the selectivity to a large extent.[16-20] Molecular beam offers the single collision condition of reactants on catalyst surfaces and hence offers to decrease the contact time by few orders of magnitude.

Methane partial oxidation to formaldehyde with high selectivity at low methane conversion has been reported with MoO_3, V_2O_5, Nb_2O_5.[15-20] Michalkiewicz et al.[18] employed polymorphic niobium (V) oxides (H-Nb_2O_5 and M-Nb_2O_5) as a catalyst and evaluated methane conversion to formaldehyde between 693 and 1023 K; 78 % formaldehyde selectivity was observed at 0.2 % methane conversion at a contact time of 0.9 s and 1000 K. More than 0.2 % methane conversion decreases the selectivity exponentially. Nedyalkova et al.[20]synthesized Fe-doped CZ fluorite catalyst and found that low temperature partial oxidation of methane to formaldehyde occurs between 573 and 873 K; while HCHO selectivity was observed to be 20 to 55 % below 673 K, methane conversion is less than 0.5

%. When methane conversion increases to 6 % at ≥773 K HCHO selectivity decreases to 2-4 %. Banares et al[21] carried out partial oxidation of methane on silica supported transition metal (V, Mo, W and Re) oxide and found that 0.8 wt % $MoOx/SiO_2$ shows the maximum activity with 13.9 % methane conversion. Highly monodispersed vanadium oxide[22-24] and molybdenum oxide[25,26] on high surface area support shows better activity for methane oxidation to formaldehyde. Zhang et. al.[27] claimed that NO_2 promotes the partial oxidation of methane and lowers the reaction temperature by 300 K (from 1173 to 873 K). They also claim that NO_2 favours the formation of oxidation product at the expense of C_2 hydrocarbon. Weng et. al.[28] has carried out partial oxidation of methane to formaldehyde on Mo/Sn/P silica supported catalyst in temperature regime of 848 to 948 K. They achieved 2 to 5.8 % methane conversion with 91.9 to 30.6 % HCHO selectivity; selectivity decreases with an increase in reaction temperature. Indeed, above discussion underscores the complexity of the problem; however, low CH_4 conversion generally favours HCHO formation.

We investigated C-H activation of methane to HCHO on $Ce_{1-x}Zr_xO_2$ (CZ; x = 0.1 to 1) thin films in a home-built molecular beam (MB) instrument (MBI).[29]Zr-introduction into the ceria lattice improves the redox properties of CZ along with thermal stability, which prevents agglomeration at high temperatures.[30-34] Brinker et al and Niemantsverdriet et al used different methods to prepare thin films, with the aim to bridge the material gap.[35,36]Our earlier report on porous CZ thin films addresses bridging the material and pressure gaps by correlating the oxygen storage capacity (OSC) measured in MBI and CO oxidation activity measured on powder CZ catalysts at ambient pressure.[37] One to one correlation was observed between the above two extreme conditions makes the method relevant to address material gap problems. Mn-doped CZ films have been employed for methane to syngas conversion.[38] From the present MBI study on CZ films, it has been observed that high cerium content of CZ film increases partial oxidation activity. C-H activation of methane to HCHO on Ce-rich CZ thin film starts at ≥ 950 K and $Ce_{0.9}Zr_{0.1}O_2$ shows partial oxidation of CH_4 to HCHO at T ≥ 1000 K and its activity increases with increase in temperature. Present chapter is focussed on bridging the material gap and related aspects like understanding mechanistic aspect of reaction though MBI, rather than finding a new or improved catalyst for methane activation. CZ thin films prepared and characterised well and those aspects are discussed in detail in chapter 3A. Molecular beam experiment details also have been described in chapter 3A. Methane activation to formaldehyde aspects are exclusively discussed in this chapter.

3B.2 Results and Discussion

3B.2.1 Molecular Beam Studies of Methane oxidation on $Ce_{0.9}Zr_{0.1}O_2$ thin film

MB measurements were made for oxygen adsorption for three CZ compositions and the results are discussed in detail in Chapter 3A. Generally, the rate of O_2 adsorption increases with increase in temperature for any CZ composition. Cerium-rich CZ film ($Ce_{0.9}Zr_{0.1}O_2$) has shown high rate of oxygen adsorption and also high oxygen storage capacity (OSC). Detailed studies of O_2 adsorption on CZ thin films have been reported in our earlier publication and readers are requested to refer ref. 37 and 38. Partial oxidation of methane on CZ thin films have been measured and it is found that Ce-rich thin film exhibits high activity and in correspondence with oxygen adsorption characteristics. Partial oxidation of methane along with kinetic parameters have been studied and discussed in detail, particularly for $Ce_{0.9}Zr_{0.1}O_2$ composition.

Fig. 3B.1 shows the first sign of methane oxidation at 950 K with CH_4:O_2 = 1:2 ratio on $Ce_{0.9}Zr_{0.1}O_2$ thin film; however, the same was not observed at 950 K with methane rich compositions, such as CH_4:O_2 = 1:1 as shown in Fig. 3B.2. At 950 K, only combustion products were observed with stoichiometric and more oxygen containing CH_4 + O_2 mixture. Although oxygen adsorption was observed below 950 K, no methane oxidation/activation was observed with any CZ compositions. At t = 25 s molecular beam of reactants mixture was allowed into the UHV chamber with shutter in closed position; this prevents direct interaction of MB with the surface of catalyst. Partial pressure of methane and oxygen increases immediately. At t = 45 s shutter was opened which allows direct adsorption of reactants on the surface of the catalyst. O_2 adsorption was observed immediately on shutter opening with sign of marked decrease in partial pressure, which indicates the consumption of O_2 during the course of reaction. No fast changes in partial pressure for methane, unlike in the case of O_2, was observed for shutter oscillation; this is mainly due to very small sticking coefficient of CH_4.[39,40] However, a gradual and noticeable change observed for adsorption of methane on shutter opening. Difference in partial pressures between shutter open and close positions has been used for methane conversion calculations. A gradual increase in partial pressure of H_2O and CO_2 was observed along with oxygen and methane adsorption. CO_2 (H_2O) reaches the steady state at t = 155 s (105 s). Thus we observe relatively slow CO_2 formation kinetics, which directly indicates that reaction proceeds via diffusion controlled process due to porous nature of CZ thin films. Being the smallest in size, H-atoms diffuse fast into the pores and reacts with lattice oxygen to form water molecules.

At t = 240 s shutter was closed which prevents direct interaction of reactants on the catalyst; however this leads to a decrease in partial pressure of CO_2 and H_2O and it reaches

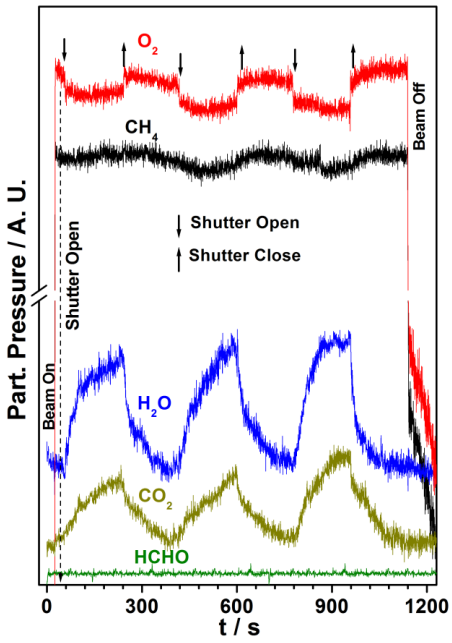

Fig. 3B.1 Experimental kinetic data for oxidation of CH_4 with O_2 in 1:2 ratio at 950 K on $Ce_{0.9}Zr_{0.1}O_2$ thin film. Molecular beam oscillation was made for every 180 s. Only combustion products were observed. Up and down arrow signs for shutter closing and opening, respectively, are used in all figures.

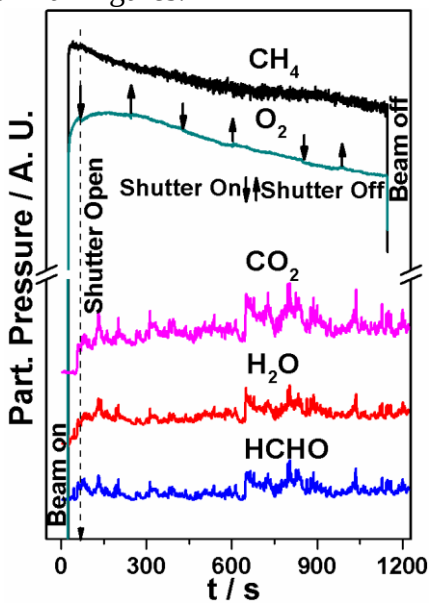

Fig. 3B.2 Selective oxidation of methane using CH_4:O_2 in 1:1 ratio on $Ce_{0.9}Zr_{0.1}O_2$ thin film. No C-H activation takes place at this temperature hence no reaction is observed.

the background level at t = 330 s. Similarly, reactants partial pressure reaches the original level observed before shutter opening at the first instance. No other partially oxidized products were observed, including HCHO. The oscillation of the molecular beam has been made several times to reproduce the kinetic data. Further several parameters, like variation of reaction temperature, O_2-rich to CH_4-rich compositions has been studied and described below. All the reactions reported in this communication have been reproduced at least three

times on the same CZ compositions within an error margin of 10 %. In fact this hints the quality of surface and thin film remains the same.

Fig. 3B.3 shows the experimental kinetic data for the oxidation of methane with CH_4:O_2 = 1:1 composition at 1000 K on (a) $Ce_{0.9}Zr_{0.1}O_2$, as well as (b) $Ce_{0.7}Zr_{0.3}O_2$ compositions. On opening the shutter at t = 55 s (dashed line, Fig. 3B.3a), CO_2 and H_2O forms, which is similar to the results discussed in Fig. 3B.1. However, both H_2O and CO_2reach the steady state at t = 200 and 125 s, respectively; this observation is similar to the combustion products evolution at 950 K, however with relatively fast kinetics. Indeed, partial pressure of water initially overshoots the steady state level indicating a fast diffusion of H-atoms to form water molecules at high temperatures. Along with combustion products, interestingly, HCHO formation begins, albeit, after a delay of 20 s at t = 75s. In fact, a sudden burst in HCHO was observed at the time of shutter opening (t = 55 s), and the same subsides immediately. Spike in HCHO partial pressure was reproducibly observed at the point of opening shutter and one such example is shown in the inset of Fig. 3B.3a. HCHO production reaches the steady state at t = 153 s, which is longer than that for combustion products. This underscores the slow formation kinetics of HCHO and predominantly contributes to the rate determining step for the overall reaction. In general, rate of reaction increases with increase in reaction temperature, which can be easily identified by an increase in consumption of O_2, as well as larger amount of products formation, compared to the reaction at 950 K. Selectivity and yield of HCHO is less compared to CO_2, as the heat of combustion of HCHO is highly exothermic than methane (Equn. 3B.1 and 3B.2).[13,14] While closing the shutter at t = 240 s the partial pressure of all product i.e. CO_2, H_2O and HCHO decreases and it attains the background level. CO_2 takes only 10 s to reach the new steady state at t = 250 s, while H_2O and HCHO takes 65 s to reach steady state indicating that the delay in attaining the new steady state for HCHO is probably due to its further oxidation into CO_2 and H_2O.

MB oscillation was made at least three times to ensure the kinetic data is reproducible within the experimental error limit of 10 %. Every time the shutter was opened, importantly, sudden burst in HCHO pressure was observed followed by HCHO production after about 20 s delay. We attribute this observation to the following: It is very likely that HCHO formation requires catalytic sites that are rich with electrons, such as Ce^{3+} and associated O_v sites. Fully oxidized sites would lead to total oxidation products. After closing the shutter, due to the unavailability of reactants directly, as well as due to high temperatures, CZ surface is likely to be enriched with O_v andCe^{3+}. This factor induces a sudden spurt in HCHO on opening the shutter. Three points are worth highlighting about this observation. First is the direct

conversion of methane to HCHO, albeit in a short burst. Second is the availability of plenty of oxygen from the direct beam of reactants makes the surface more oxidizing and hence combustion products formation increases instantly. Oxygen diffusion into the subsurface and bulk brings in the O_v to the surface and HCHO formation picks up gradually after a delay time of 20 s at 1000 K, and reaches the steady state again. Third point to be noted is an increase in CO_2 and H_2O background level pressure, while HCHO remains at the initial level, under beam off conditions after MB oscillations, indicating the diffusion nature of the entire reaction. Fig. 3B.3b shows the oxidation of methane to combustion products at 1000 K on $Ce_{0.7}Zr_{0.3}O_2$ composition, with no marginal sign of HCHO formation. Similar results were observed for other Zr-rich CZ composition thin films.

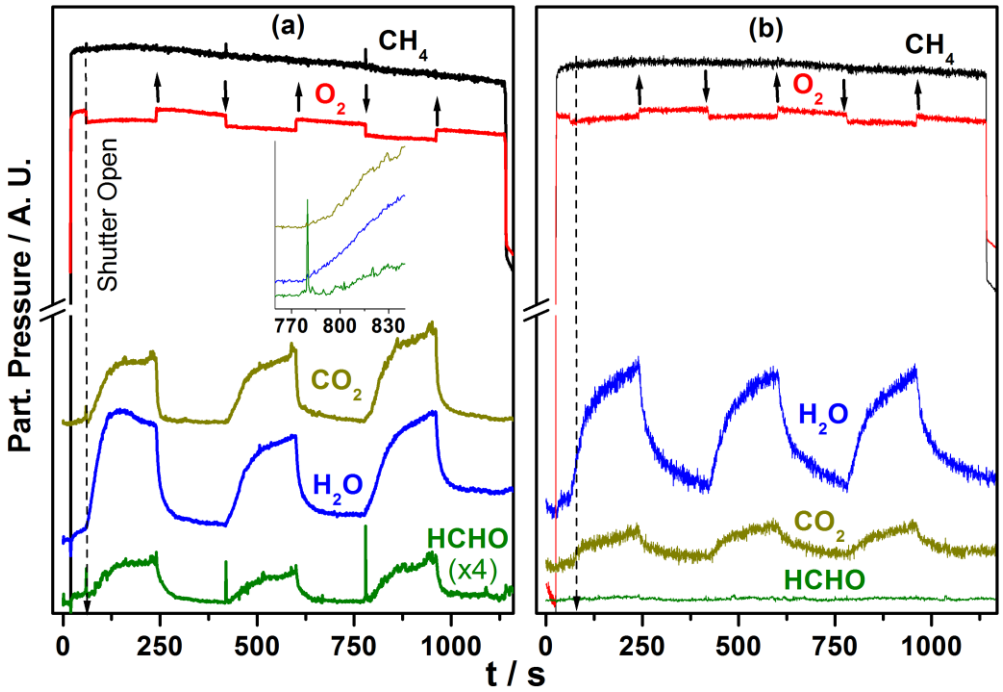

Fig. 3B.3 Experimental kinetic data for selective oxidation of CH_4 with O_2 in 1:1 ratio on a) $Ce_{0.9}Zr_{0.1}O_2$ and b) $Ce_{0.7}Zr_{0.3}O_2$ thin film at temperature T = 1000 K. The shutter operation i.e. opening and closing of MB was made after every 180 s.

Fig. 3B.4a shows the experimental data for oxygen adsorption during the course of reaction at 1000 K with various CH_4:O_2 ratio from 5:1 to 1:5. Figs. 3B.1, 3B.3 and 3B.4a emphasize that oxygen was consumed predominantly under reaction conditions and irrespective of reactants composition; this leads to an inevitable formation of the combustion products, especially with O_2-rich reaction mixture. Fig. 3B.4b shows the rate of oxygen adsorption with various O_2/CH_4ratios at 1000 and 1050 K. Although oxygen adsorption increases with oxygen content, careful analysis of Fig. 3B.4b reveals a change in slope from methane-rich to oxygen-rich compositions. Rate of oxygen adsorption is relatively small with

CH_4-rich compositions underscoring the hindrance for oxygen adsorption; while it is the opposite trend with O_2-rich compositions. Similar analysis show methane conversion gradually changes from 0.9 (0.08 ML/s) to 1.6 % (0.15 ML/s) from CH_4-rich (O_2:CH_4 = 1:5) to O_2-rich (O_2:CH_4 = 5:1) compositions, respectively, on $Ce_{0.9}Zr_{0.1}O_2$. Very likely, carbon or carbonaceous species on the catalyst surfaces due to methane-rich compositions slow down the diffusion of oxygen atoms into the sub-surface and bulk; this is in addition to the oxygen consumption for CO_2 and H_2O formation.

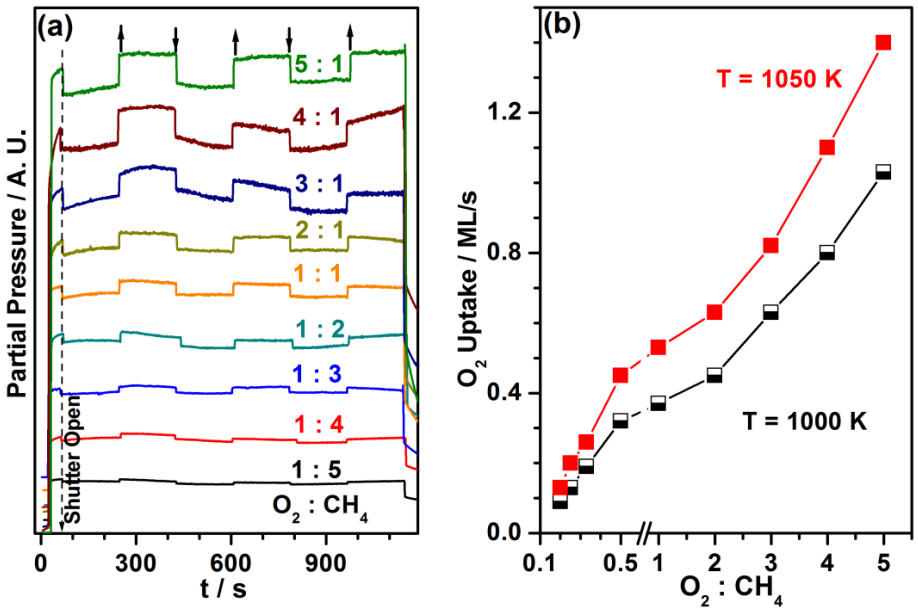

Fig. 3B.4 a) Experimental data for O_2adsorption, and b) rate of oxygen adsorption during the course of reaction with different O_2/CH_4ratio at T = 1000 K and 1050 K on $Ce_{0.9}Zr_{0.1}O_2$.

Fig. 3B.5 shows the dependence of products evolution as a function of time and O_2:CH_4 ratio at 1000 K. Evolution of all products was plotted in separate panels to minimize the complexity of the reaction. Partial oxidation of methane has also been evaluated at 1050 K (results not shown), and the same trend has been found as that of at 1000 K. Irrespective of reactants composition, all products formation occurs, and the same increases form methane-rich to O_2 rich compositions. Especially, with oxygen-rich compositions above 1:1 of O_2:CH_4, the rate of products formation seems to enhance linearly. Rate of CO_2 and HCHO production shows less dependence on CH_4:O_2 ratio for methane-rich compositions. Another important point to be noted is the decrease in delay time between shutter opening and HCHO formation with oxygen rich reactants. In contrast to the expectations of total combustion with O_2-rich compositions, HCHO production at high rate indicates the active nature of the surface. With more oxygen supply at high temperatures, the diffusion is also expected to be faster and this is likely to enhance the O_v diffusion to the surface, which favours HCHO

formation. More carbon species (C, CH_x) deposition on the surface might prevent or decelerate O_v diffusion towards the surface and hence low rate of HCHO occurs with methane-rich compositions; nonetheless, CH_x species on the surface makes it significantly reduced, especially with small amount of O_2 available in gas-phase. Partial (and total) oxidation of CH_4 is facile in O_2-rich beam at high temperature, which accelerates the migration of O_v towards the surface and hence the rate increases.[41]

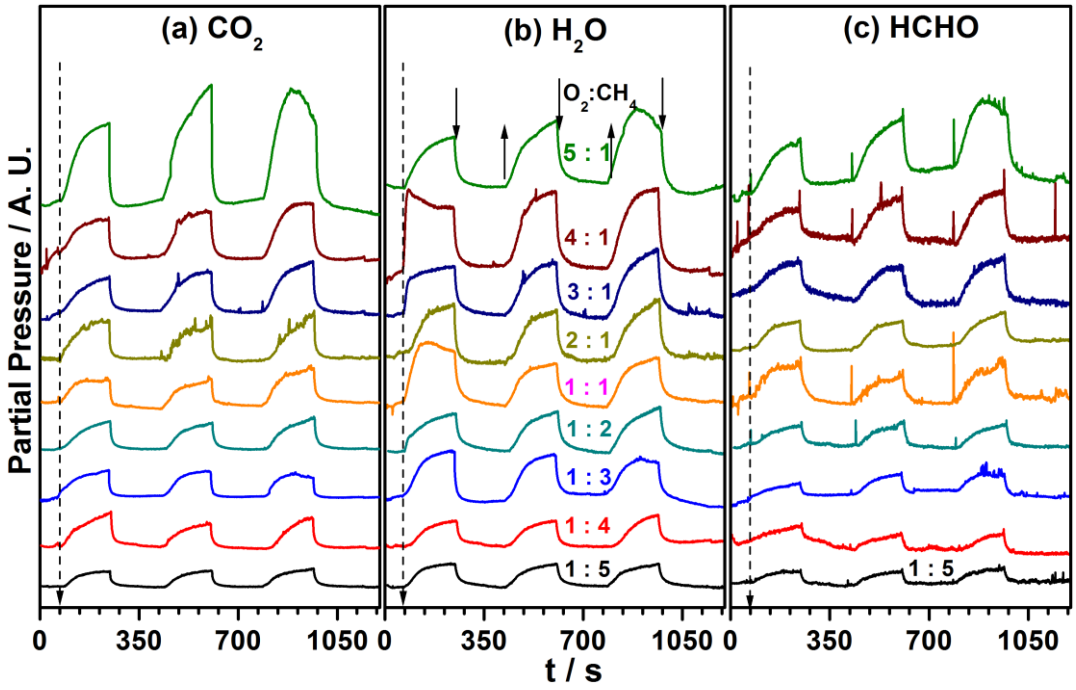

Fig. 3B.5 Products evolution as a function of time at 1000 K for different O_2:CH_4 ratios for a) CO_2, b) H_2O, and c) HCHO.

Rate of formation of formaldehyde and combustion products has been calculated from Fig. 3B.5 under steady state conditions. Fig. 3B.6 shows the rate of formation of products, (a) CO_2, (b) H_2O, and (c) HCHO, as a function of O_2/CH_4 ratio, at 1000 and 1050 K. Percent ratio of rate of formation of HCHO to HCHO + CO_2, which is selectivity of HCHO among carbon containing products, is plotted in Fig. 3B.6d. It has been found from Fig. 3B.6 that the rate of formation of products increases with increase in O_2/CH_4 ratio. There is a slow and steady increase unto O_2/CH_4 ratio of 2. A breakthrough in the overall rate is observed at a ratio of 3. Rate of formation of all products increased 3-5 times that of methane rich composition. This trend is highly prominent at 1050 K. Percent selectivity of HCHO is an important factor, which is shown in Fig. 3B.6d. Not surprisingly, selectivity is found to be higher for the methane rich beam and it is found to be the highest at 12.2 % for 5:1 ratio of CH_4:O_2 at 1050 K. With an increase in O_2 content, selectivity towards HCHO decreases. It was also found that with increase in temperature HCHO selectivity increases up to O_2/CH_4

ratio of 2, thereafter selectivity decreases with increase in O_2 rich compositions. Nevertheless, 12.2 % selectivity observed is better or comparable to the values reported for many of the reported catalyst systems.[16-18] However, compared to the vanadia-

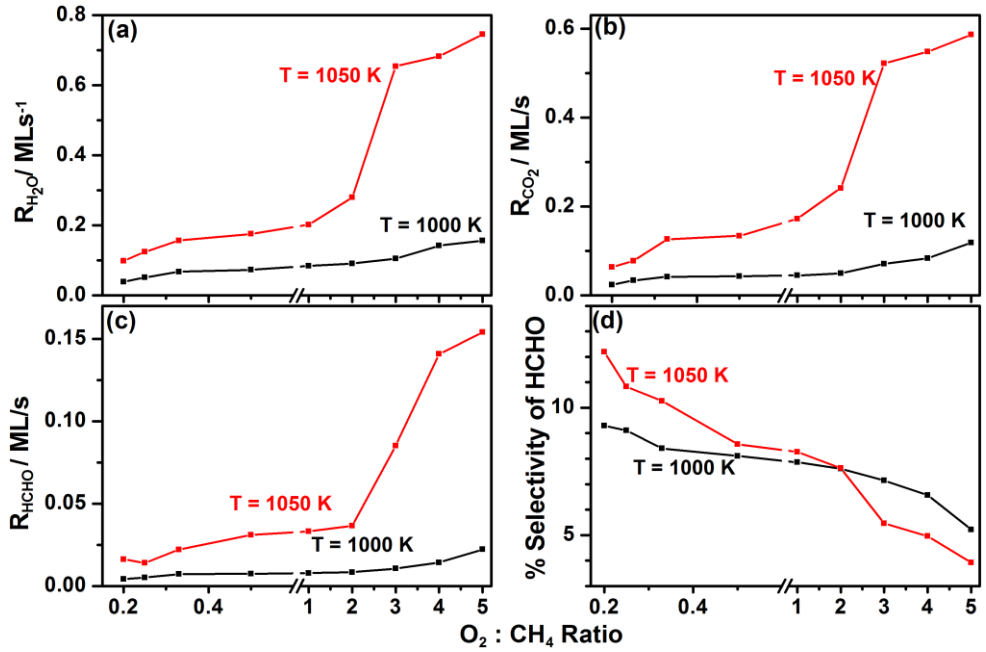

Fig. 3B.6 Rate of formation of oxidation products, a) H_2O, b) CO_2, c) HCHO and d) HCHO/CO_2 ratio at two different temperatures as a function of O_2/CH_4ratio.

-based catalyst,[15,22-24] activity is lower with present CZ catalyst. Lin et al[42] observed HCHO selectivity of 90 % at 873 K using MoO_3/SiO_2 catalyst with low CH_4 conversion but as the temperature increases to 983 K selectivity becomes zero; compared to this $Ce_{0.9}Zr_{0.1}O_2$ thin film shows a maximum selectivity of 12.2 %.

CO was not observed in any of our experiment, may be due to its oxidation to CO_2 due to porous nature of CZ. 100 % CO oxidation to CO_2 was observed on $Ce_{0.9}Zr_{0.1}O_2$ above 625 K.[37] To the best of our knowledge, complex reactions, such as CH_4 activation has not been measured on thin films of real-world catalysts in surface science setup like MBI. Present work underscores the direct conversion of CH_4 to HCHO on reduced Ce^{3+} and O_v sites.

3B.3 Conclusion

Partial oxidation of methane has been carried out on various compositions of ceria-zirconia solid solution thin films in a home-built molecular beam setup. C-H activation of methane generally takes place at temperatures higher than 950 K. Ceria rich thin film $Ce_{0.9}Zr_{0.1}O_2$ exhibits partial oxidation of methane to formaldehyde at 12 % selectivity and 1.6 % methane conversion. Though rate of formation of formaldehyde increases with increase in oxygen rich reactants compositions as well as at high temperatures, HCHO selectivity remains at 12 %. No formaldehyde formation was observed with Zr-rich CZ compositions. A careful analysis

of the results obtained suggests the reduction sites, such as oxygen vacancies, CH_x, are necessary for partially oxidized product. Beam oscillations carried out in the present set of experiments also indicates the necessity to quickly alter the reactants composition between methane-rich to oxygen-rich streams to maximize and manage the activity and selectivity. If large amount of oxygen adsorption can be manipulated by quick excursion between O_2-rich and CH_4-rich compositions, more partially oxidized product can be produced and more work is suggested in this direction. Although diffusion is an integral part of catalysis phenomenon, such material gap reduction attempts allow us to explore more on this.

3B.4 References

1. H. D. Gesser, N. R. Hunter, *Chem. Rev*. **1985**, 85, 235.
2. J. H. Lunsford, *Catal. Today* **2000**, *63*, 165.
3. B. C. Enger, R. Lodeng, A. Holmen, *Appl. Catal. A: Gen.* **2008**, *346*, 1.
4. C. F. Cullis, D. E. Keene, D. L. Trimm, *J. Catal.* **1970**, *19*, 378.
5. L. C. Kao, A. C. Hutson, A. Sen, *J. Am. Chem. Soc.* **1991**,*113*, 700.
6. S. Y. Chen, D. Willcox,. *Ind. Eng. Chem. Res.* **1994**, *33*, 832.
7. Y. Wang, K. J. Otsuka, *J. Catal.* **1995**, *155*, 256.
8. X. Yang, K. D. Jung, S. H. Cho, O. Shim, S. J. Uhm, S. H. Han, *Catal. Lett.* **2000**, *64*, 185.
9. B. Michalkiewicz, *Appl. Catal. A: Gen.* **2004**, *277*, 147.
10. R. A. Periana, D. J. Taube, E. R. Evitt, D. G. Loffler, P. R. Wentrcek, G. Voss, T. Masuda, *Science* **1993**, *259* 340.
11. M. Muehlhofer, T. Strassner, W. A. Herrmann, *Angew. Chem. Int. Ed.* **2002**, *41*, 1745.
12. M. J. Brown, N. D. Parkyns, *Catal. Today*, **1991**, *8*, 305.
13. X. L. Sang, K. Z. Li, H. Wang, Y. G. Wei, *Rare Met.* **2014**, *33*, 230.
14. S. B. Dworkin, A. M. Schaffer, B. C. Connelly, M. B. Long, M. D. Smookea, M. A. Puccio, B. M. Andrew, J. H. Miller, *Proc.Combustion Institutes* **2009**, *32*, 1311.
15. L. D. Nguyen, S. Loridant, H. Launay, A. Pigamo, J. L. Dubois, J. M. M. Millet, *J. Catal.* **2006**, *237*, 38.
16. S. Morteza, V. Leila, *World Appl. Sci. J.* **2009**, *6*, 339.
17. Q. Zhu, X. Zhao, Y. Deng, *J. Nat. Gas Chem.* **2004**, *13*, 191.
18. B. Michalkiewicz, J. S. Nazzal, P. Tabero, B. Grzmil, U. Narkiewicz, *Chem. Papers* **2008**, *62*, 106.
19. M. Faraldos, M. A. Banares, J. A. Anderson, H. Hu, I. E. Wachs, J. L. G. Fierro, *J. Catal.* **1996**, *160*, 214.

20. R. Nedyalkova, D. Niznansky, A. C. Roger, *Catal. Commun.* **2009**, *10*, 1875.
21. M. A. Banares, L. J. Alemany, M. L. Granados, M. Faraldos, J. L. G. Fierro, *Catal. Today* **1997**, *33*, 73.
22. B. Lin, X. Wang, Q. Guo, W. Yang, Q. Zhang, Y. Wang, *Chem. Letters* **2003**, *32*, 860.
23. H. Berndt, A. Martin, A. Brucker, E. Schreier, D. Muller, H. Kosslick, G. U. Wold, B. Lucke, *J. Catal.* **2000**, *191*, 384.
24. A. Parmaliana, F. Frusteri, A. Mezzapica, M. S. Scurrell, N. Giordano, *J. Chem. Soc. Chem. Commun.* **1993**, 751.
25. V. A. Ebrahimi, J. J. Rooney, *J. Mol. Catal.* **1989**, *50*, L17.
26. W. Yang, X. Wang, Q. Guo, Q. Zhang, Y. Wang, *New J. Chem.* **2003**, *27*, 1301.
27. J. Zhang, V. Burkle-Vitzthum, P. M. Marquaire, *Chem. Engineer. J.* **2012**, *189-190*, 393.
28. T. Weng, E. E. Wolf, *Appl.Catal. A: General* **1993**, *96*, 383.
29. C. S. Gopinath, A. Dubey, S. K. Kolekar, (in preparation).
30. E. Mamontov, T. Egami, R. Brezny, M. Koranne, S. Tyagi, *J. Phys. Chem. B* **2000**, *104*, 11110.
31. S. Meiqing, W. Xinquan, A. Yuan, W. Duan, Z. Minwei,W. Jun, *J. Rare Earths* **2007**, *25*, 48.
32. E. Aneggi, M. Boaro, C. D. Leitenburg, G. Dolcetti, A. Trovarelli, *J. Alloys & Comp.* **2006**, *408-412*, 1096.
33. S. Damyanova, B. Pawelec, K. Arishtirova, M. V. M. Huerta, J. L. G. Fierro, *Appl. Catal. A: Gen.* **2008**, *337*, 86.
34. J. Beckers, G. Rothenberg, *Dalton Trans.* **2008**, *46*, 6573.
35. C. J. Brinker, G. W. Scherer, *Sol-gel Science, Academic Press, New York* **1990**, p. 180.
36. A. M. Saib, A. Borgna, J. V. D. Loosdrecht, P. J. V. Berge, J. W. Niemantsverdriet, *J. Phys. Chem. B* **2006**, *110*, 8657.
37. A. Dubey, S. K. Kolekar, E. S. Gnanakumar, K. Roy, C. P. Vinod, C. S. Gopinath, *Catal. Struct. React.* **2016**, DOI 10.1080/2055074X.2015.1133269.
38. A. Dubey, S. K. Kolekar, C. S. Gopinath, *ChemCatChem* (DOI:10.1002/cctc.201600365).
39. L. Jiang, H. Zhu, R. Razzaq, M. Zhu, C. Li, Z. Li, *Int. J. Hydrogen Energy* **2012**, *37*, 15914.
40. *CRC Handbook of Chemistry and Physics*, 85th ed.; Lide, D. R., Ed.; CRC Press: Boca Raton, FL, **2004**.
41. Q. Sun, J. M. Jehng, H. Hu, R. G. Herman, I. E. Wachs, K. Klier, *J. Catal.* **1997**, *165*, 91.
42. Z. Lin, F. Jian, Q.F. Li, *J. Natural Gas Chem.* **1997**, *6*, 322.

Chapter 4 – C-H Activation of Methane to Syngas on $Mn_xCe_{1-x-y}Zr_yO_2$ - A Molecular Beam Study

Mn-doped ceria zirconia thin films ($Mn_xCe_{1-x-y}Zr_yO_2$ (MCZ)) have been employed as flat model catalyst surfaces for CH_4 activation. MCZ thin films exhibit characteristics of single crystal and powder materials, such as smooth surfaces, and porosity. From molecular beam studies, it has been identified that the oxygen storage capacity (OSC) increases with Mn-content. Mutually exclusive observation of H_2O or a mixture of products (CO_2+CO+H_2) occurs, when the reactants was allowed to react directly on MCZ underscoring their formation or prevention (and consumption), respectively. Above observation suggests that there is competition and cooperation among different elementary reactions under complementary conditions. From a significant partial oxidation of CH_4 through C-H activation, it is found that formation of syngas begins at 700 K and the reaction rate increases with increasing temperature. Kinetic evidences indicate that the reaction proceeds through a combustion-reformation pathway.

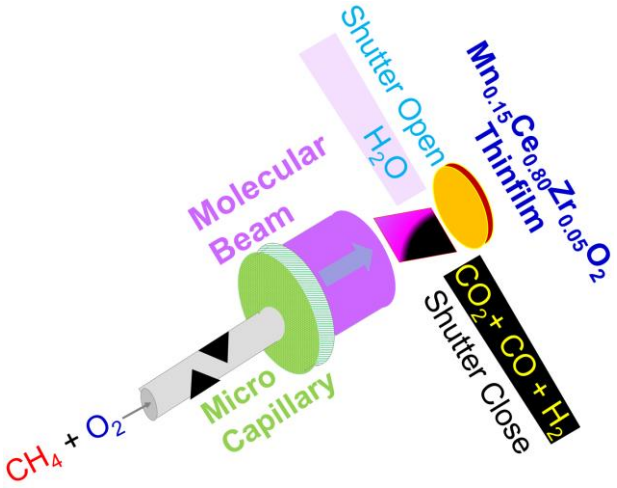

C-H activation of methane to syngas with mechanistic details has been explored on $Mn_xCe_{1-x-y}Zr_yO_2$ porous thin films. Observation of H_2O or (CO_2+CO+H_2) occurs, while the reactants adsorb directly or no adsorption of reactants, respectively, on catalyst. There is competition and cooperation among different elementary reactions under complementary conditions.

4.1 Introduction

Methane is a principal constituent of natural gas, and according to the international energy agency (IEA) its consumption is expected to increase by 30-40 % every 25 years.[1] It is anticipated that there will be a gradual deficit in the oil production in the not so distant future, and there will be an increasing demand for energy resources.[2] Therefore, there is a need to convert natural gas to large petroleum resources to compensate the deficit in the oil production. Production of syngas ($CO + H_2$) is the first step in the conversion of methane gas to liquid fuels. Catalytic partial oxidation of methane (Eq. 4.1) is one of the better methods compared to other processes, such as steam reforming (Eq. 4.2) and auto-thermal reforming for generation of H_2 and CO, which require high temperature and high pressure. Catalytic partial oxidation is exothermic in comparison to steam reforming of CH_4.

$CH_4 + ½\ O_2 \rightarrow CO + 2H_2$, $\Delta H = -36\ KJmol^{-1}$ (4.1)

$CH_4 + H_2O \rightarrow CO + 3H_2$, $\Delta H = +206\ KJmol^{-1}$ (4.2)

Nonetheless, the main hindrance is the C-H activation of CH_4 which requires 439 KJ/mole for its bond dissociation.[3] The adsorption of CH_4 molecule on the catalyst surface decides the activation energy for C–H activation.[4,5] The characteristics of partial oxidation of methane are high temperature and short contact time.[6-8] Generally, metal surfaces are used to oxidize alkanes either to olefins or syngas at high temperatures of around 1000 K.[9,10] It has been suggested that partial oxidation of methane to syngas happens via two types of mechanisms namely, a) direct partial oxidation, and b) combustion-reformation pathway. Wilson et al. studied partial oxidation of CH_4 on Rh(111) surfaces at 1165 K and found that it occurs via direct partial oxidation pathway.[11] Sasaki et al. studied the energetics of activation of methane and ethane on Pt and Rh foils and found that partial oxidation occurs at ≥ 900 K.[12,13] Horn et al. evaluated Rh-coated-α-Al_2O_3 for methane to syngas between 1083 and 1313 K and found that the reaction proceeds through combustion-reformation pathway.[14] In fact, combustion-reformation pathway is highly preferred, as it involves two of the most stable molecules as reactants to produce desired syngas.

$CH_4 + CO_2 \rightarrow 2CO + 2H_2$ $\Delta H = +247\ KJ/mol$ (4.3)

Larimi employed $Ni/CeZrO_2$ mixed oxide and found that methane to syngas reaction occurs between 723 and 1173 K.[15,16] Due to endothermic nature of C-H activation, generally it occurs at around 1000 K and there are not many catalysts that show activity below 1000 K. Further, mechanism of partial oxidation of CH_4 is yet to be addressed in detail, due to complex nature of the reaction itself and macroscopic nature of kinetic data. Little

information on elementary reactions is available,[11] and no such information is available on working catalysts.[6-10,12-16]

Ceria is a versatile material and well known in the field of catalysis because of its high oxygen storage capacity (OSC), and redox property.[17,18] With cation doping in the ceria lattice, its thermal stability, OSC and redox property can be further altered.[19,20] Isolated Mn and V are known to enhance partial oxidation and oxidative dehydrogenation of organic molecules through C-H activation.[21-25] In this context, we have prepared Mn-doped ceria zirconia ($Mn_xCe_{1-x-y}Zr_yO_2$) (MCZ) thin films by a combination of sol-gel and spin coating method,[26,27] and evaluated for partial oxidation of methane.

Molecular beam instrument (MBI)[28,29] has been extensively used to examine the MCZ thin films for the partial oxidation of methane. Present MBI studies revealed that Mn-rich (15 %) MCZ composition was found to exhibit the highest O_2 adsorption at any given temperature, and found to increase with an increase in temperature. To the best of our knowledge, there are not many reports on the surface science studies on partial oxidation of such thin films. Mutually exclusive observation of H_2O or a mixture of CO_2+CO+H_2 products occurs, when the molecular beam (MB) of reactants (CH_4 + O_2) was allowed to react on MCZ surfaces underscoring their formation or inhibition (as well as consumption), respectively. Similarly, when the MB was blocked, exactly the opposite trend occurs, and a mixture of CO_2+ CO + H_2 products was observed. This critical observation underscores that the partial oxidation of methane occurs via combustion – reformation pathway.

4.2 Experimental section

Preparation of ($Mn_xCe_{1-x-y}Zr_yO_2$) (MCZ) thin films has been described in sec. 2.2.1 in chapter 2, further detailed characterisation methods and molecular beam methods are described in chapter 2. Readers are requested to refer chapter 2 for full details.

4.3 Results and Discussion

4.3.1 XRD Analysis

Thin film and powder forms of $Mn_xCe_{1-x-y}Zr_yO_2$ with a different value of x and y is subjected to XRD analysis to determine the crystalline structure, and the results are shown in Fig. 4.1a and 4.1b, respectively. Ce-rich MCZ compositions exhibit diffraction features corresponding to ceria cubic fluorite structure. The different crystallographic planes are indexed in the figure. It can be readily seen that there is a good correspondence between XRD patterns of thin films and powder materials suggesting a solid solution nature of the MCZ. While the powder XRD patterns exhibit high intensity for (111) and hence the preferred facet, thin films show comparable intensity for (111) and (200) facets, indicating a preference for (200) planes

on the surface of thin films. With Mn and Zr introduced into the CeO_2 lattice, there is a small decrease in 2θ value (Fig. 4.1c) observed for 5 and 10 % Mn-containing MCZ compositions; while other compositions do not show a significant shift. Nonetheless, an increased broadening of the peak was observed with increasing Mn-content. Even though ionic radii of Mn^{3+} (0.79 Å) and Zr^{4+} (0.84 Å) are smaller than Ce^{4+} (0.97 Å) or Ce^{3+}(1.14 Å), the above observation indicates the formation of more Ce^{3+} to compensate the structural stress. This leads to the observation of a small increase in lattice parameter and/or peak broadening. This is also an indication of the formation of a solid solution. Basically, Ce in cubic fluorite structure of ceria is coordinated to eight O^{2-}ions, and each O^{2-} is coordinated to four Ce^{4+} ions. With metal ion doping in ceria, stress/defects occur in the lattice which can be partly minimized by Ce-reduction.[30] It is also to be underscored that Mn^{3+} will introduce O-vacancies to maintain the charge balance.

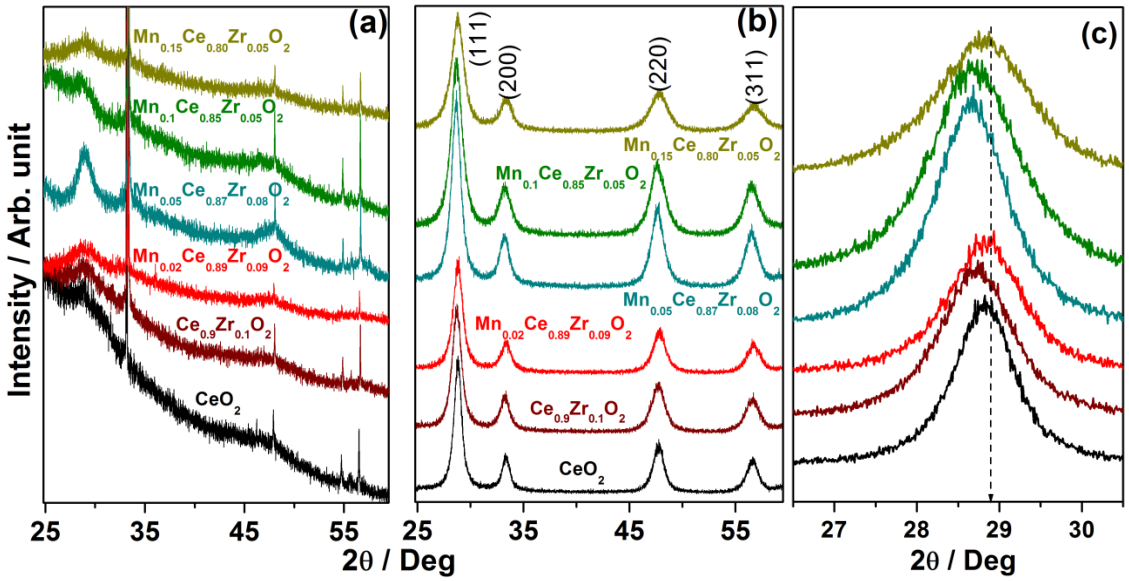

Fig. 4.1 XRD pattern of $Mn_xCe_{1-x-y}Zr_yO_2$ in a) thin film, b) powder sample. High intensity narrow feature observed in panel a are due to Si-substrate. (c) XRD of $Mn_xCe_{1-x-y}Zr_yO_2$ powder sample showing change in lattice parameter. It shows a shift or broadening of (111) diffraction feature. The sharp peak at 2θ = 33.5° corresponds to (111) plane of Si, which appears exactly at the same position as that of (200) facet of MCZ thin films and overlaps. The sharp Si features at 2θ = 47.9 ° (220) and 56.6 ° (311) overlap with that of ceria (220) and (311) features.

4.3.2 Raman Analysis

MCZ thin film has been characterized by Raman spectral measurements and the results are shown in Fig. 4.2. A high-intensity band at 465 cm^{-1} has been observed for pure ceria, which is due to F_{2g} Raman active mode for cubic fluorite structure; this peak arises due to the symmetric arrangement of O-atom around Ce^{4+} ion. On Zr doping in $Ce_{0.9}Zr_{0.1}O_2$ (CZ), F_{2g} feature becomes narrow and shows a small red shift.[22] However, on Mn-doping in CZ, F_{2g}

feature gets broadened, gradually shifts to a lower frequency and observed at 450 cm^{-1} for $Mn_{0.15}Ce_{0.80}Zr_{0.05}O_2$ film. Above red shift of F_{2g} feature is attributed to the change in the lattice spacing and bond length due to minor lattice expansion upon introduction of Mn^{3+} and Zr^{4+} ions in ceria lattice and solid solution formation. When Mn and Zr replace the $Ce^{4+/3+}$ ion from the ceria lattice, the average dipole moment, polarizability and bond vibration of Ce-O-Mn and Ce-O-Zr has a collective effect on each other which induces an environment different from that of Ce-O-Ce in the MCZ solid solution.

4.3.3 Profilometer Analysis

The surface roughness and film thickness of MCZ films were measured, and the results are shown in Fig. 4.3. Although several measurements were made at different areas on various batches of thin films, only a set of representative results are given in Fig. 4.3.The surface profile made on the various area of a thin film was found to be very similar. The thickness of the film was measured with reference to the substrate surface as a reference. Thickness of film was observed to be in the range of 40 to 60 nm for various compositions of MCZ thin film. It was observed that the average surface roughness of film ranges from 8 to 40 nm. CZ

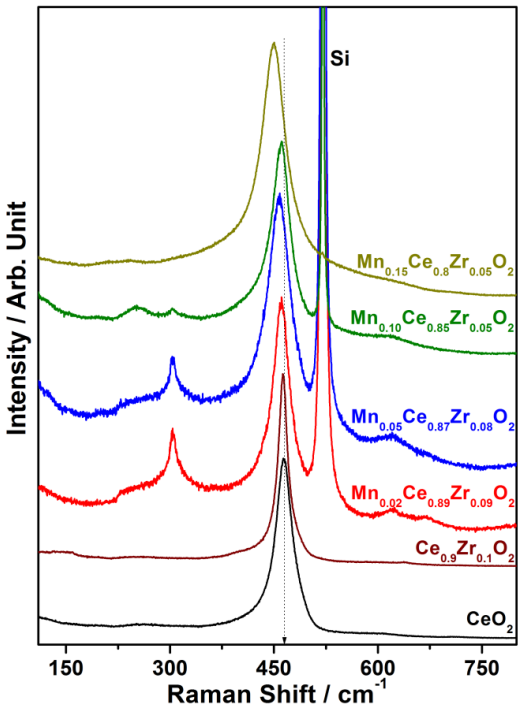

Fig. 4.2 Raman spectroscopy of various composition of $Mn_xCe_{1-x-y}Zr_yO_2$ thin film. Si features are observed around 310 and 535 cm^{-1}.

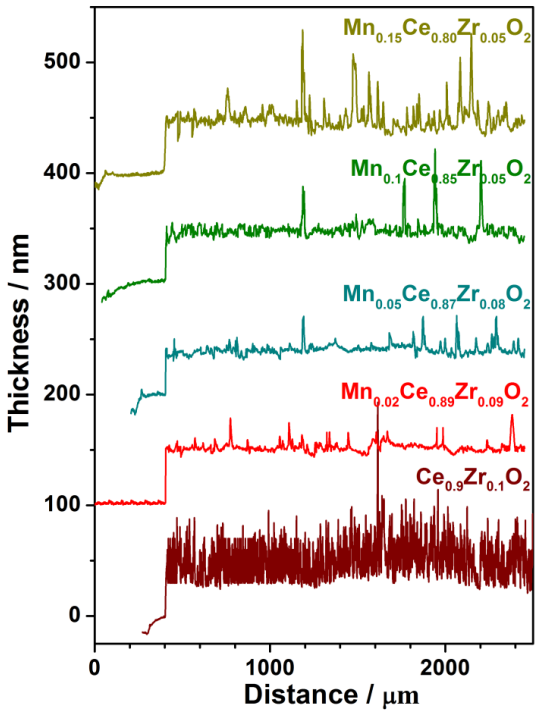

Fig. 4.3 Surface profilometer scan for surface roughness and thickness of various composition of $Mn_xCe_{1-x-y}Zr_yO_2$ thin film.

film exhibits the maximum roughness of 40 nm than any MCZ films. Sporadic spike observed in Fig. 4.3 is from the Si substrate and not from the film, which is confirmed by the

surface profile of Si substrate (not shown). The surface roughness of typical single crystals are observed to be around 30 nm; the results shown in Figure 4.3 for MCZ films compares very well to that. This suggests a comparable surface roughness of films prepared by the present method. On Mn-doping in CZ lattice, the surface roughness is reduced to ~10 nm suggesting a good enhancement in surface quality of the films.

Surface area and porosity of the powder MCZ samples were measured and all of them show type IV adsorption isotherm with H2 hysteresis loop indicating the mesoporous nature[31] of the materials. However, BET surface area changes between 102 ($Ce_{0.90}Zr_{0.10}O_2$) and 64 m^2/g ($Mn_{0.15}Ce_{0.80}Zr_{0.05}O_2$). Pore volume of 0.18 cc/g (0.12 cc/g) was observed for $Ce_{0.90}Zr_{0.10}O_2$ ($Mn_{0.15}Ce_{0.80}Zr_{0.05}O_2$) with pore diameter between 4 and 7 nm for all compositions.

4.3.4 TEM Analysis

MCZ thin films prepared directly on Au-Pt grid were employed for TEM analysis and the results are shown in Fig. 4.4. TEM images show that film formed is uniform and homogeneous throughout the area. It was also observed that as Mn-content increases, thin film becomes more granular in nature and roughness of the film increases significantly which is shown in Fig. 4.4d. With an increase in roughness of the film, the complexity of film increases which leads to various phenomena, like diffusion of reactants and products which exhibit properties of powder catalyst, thus helping to simulate the real-world reaction conditions on porous materials and bridge the material gap. Fig. 4.4a-d inset shows selected area electron diffraction (SAED) patterns, which confirms that the prominent facet exposed in CeO_2 and $Ce_{0.9}Zr_{0.1}O_2$ thin film is (111) plane along with (200), (220) and (311) planes. However, MCZ film shows predominantly (200) facet, which is different from ceria and CZ films, and is in good agreement with XRD results. Although XRD, Raman and HRTEM-SAED analysis reveals high crystallinity of MCZ thin films, small amount of amorphous phase cannot be ruled out; however such amorphous phase, if it exists, might be below the detection level of the above employed analytical methods. No phase segregation of any of the reported MCZ composition was observed. When Mn-content increases ≥ 20 atom %, Mn_3O_4 phase segregation was observed. In fact, due to this reason, it was not employed for any reaction measurements.

4.3.5 XPS Analysis

XPS analysis of MCZ thin films were made to explore the electronic structure aspects and the results are shown in Fig. 4.5 for Ce 3d, Zr 4d and Mn 2p core levels. Ce 3d spectra shows two sets of spin-orbit multiplets and associated satellite features (Fig. 4.5a).[32-34] Multiplets

appears at 882.5(v), 888.6(v″) and 898.3 eV (v‴) binding energy(BE) corresponds to Ce^{4+} $3d_{5/2}$ level; similarly peaks at 901.1 eV(u), 907.6 eV(u″) and 916.7 eV (u‴) corresponds to Ce^{4+} $3d_{3/2}$ core level of ceria. With Zr and Mn doping into the ceria lattice, there is a shift towards lower BE by 0.3 eV indicating a change in the electronic environment of ceria.

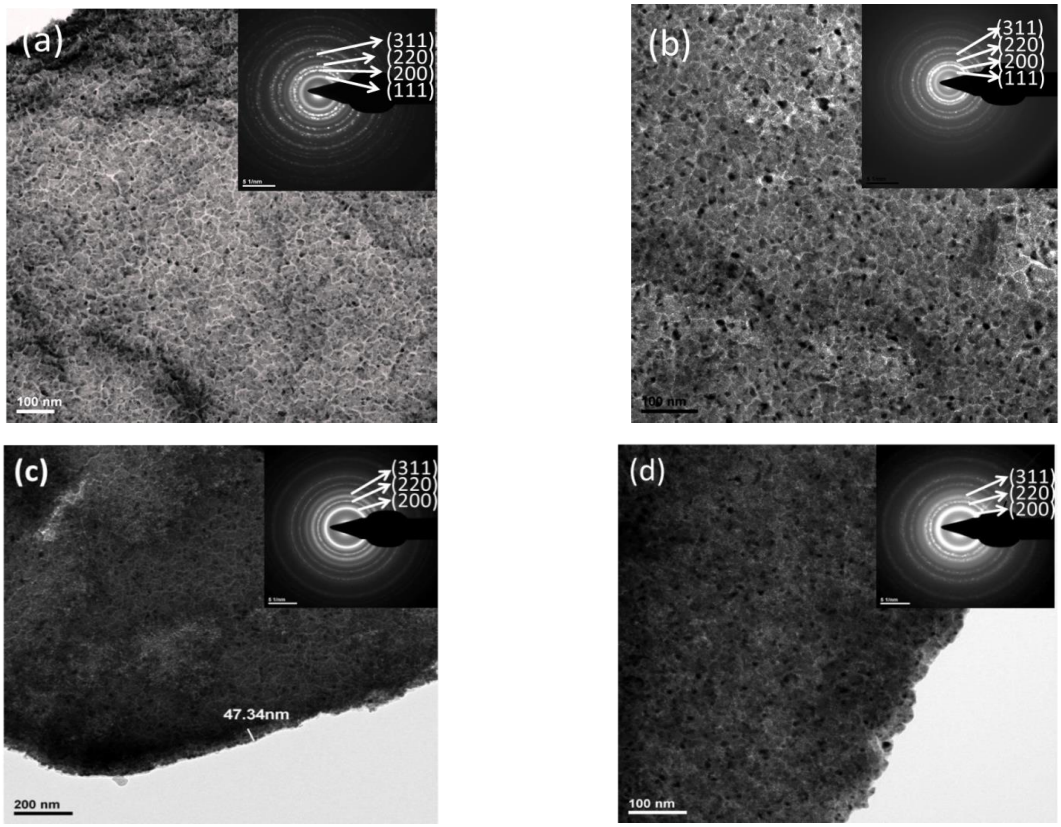

Fig. 4.4 TEM images of thin film of, a) CeO_2, b) $Ce_{0.9}Zr_{0.1}O_2$, c) $Mn_{0.05}Ce_{0.87}Zr_{0.08}O_2$, and d) $Mn_{0.15}Ce_{0.80}Zr_{0.05}O_2$.compositions. It has been shown in panels a-b that as the Zr is doped into ceria, film become more granular in nature. Image c shows that as Mn is doped into lattice of CZ, granular nature of film decreases thus decreasing roughness of thin film. Image c shows that thickness of $Mn_{0.05}Ce_{0.87}Zr_{0.08}O_2$ film is 47 nm which is in accordance with profilometer results.

Two doublets observed due to Ce^{3+} are denoted as v_0 (880.8 eV), v′ (884.6 eV), and u_0 (899.4 eV), u′ (903.2 eV) (denoted by dashed lines) due to the final state configurations of Ce $3d^94f^2$ – O $2p^5$ and Ce $3d^94f^1$ – O2p^6, respectively.[35] Deconvoluted features of Ce^{3+} and $Ce^{4+}$for $Mn_{0.02}Ce_{0.89}Zr_{0.09}O_2$ and $Mn_{0.05}Ce_{0.87}Zr_{0.08}O_2$ is shown in Fig. 4.6. Deconvolution of Ce 3d spectra of all compositions indicates that Ce^{4+} is predominantly present in pure ceria and CZ thin films. However, the above features broaden with increasing Mn-content, along with a decrease in the intensity of u‴ at 916.7 eV suggesting a relative increase in Ce^{3+} content, at the expense of Ce^{4+}. It was a surprise to note a decreasing S/N ratio with increasing Mn-content for Ce 3d, as well as other core levels (Fig. 4.5); however, reason for decreasing S/N is not known at present. O 1s core level recorded for MCZ thin films shows two features at

530.2 and 532.8 eV (Fig. 4.6b). However, no significant change in O 1s BE suggests that the average interaction between metal ions and oxygen remains the same.

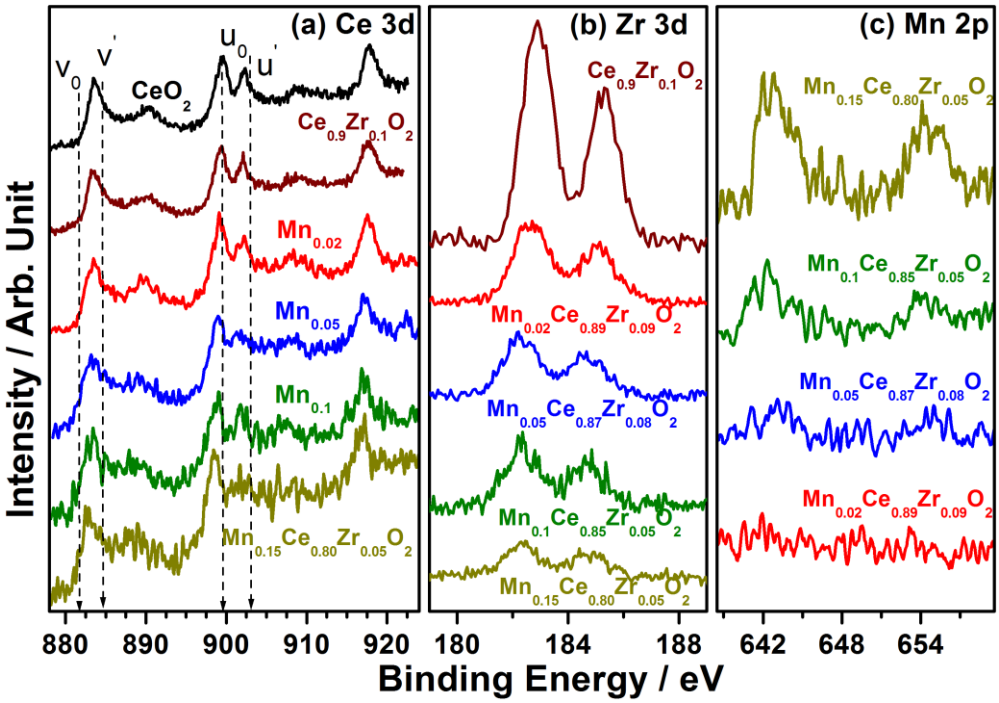

Fig. 4.5 XPS spectra recorded for (a) Ce 3d, (b) Zr 3d, and (c) Mn 2p core levels of $Mn_xCe_{1-x-y}Zr_yO_2$ thin films.

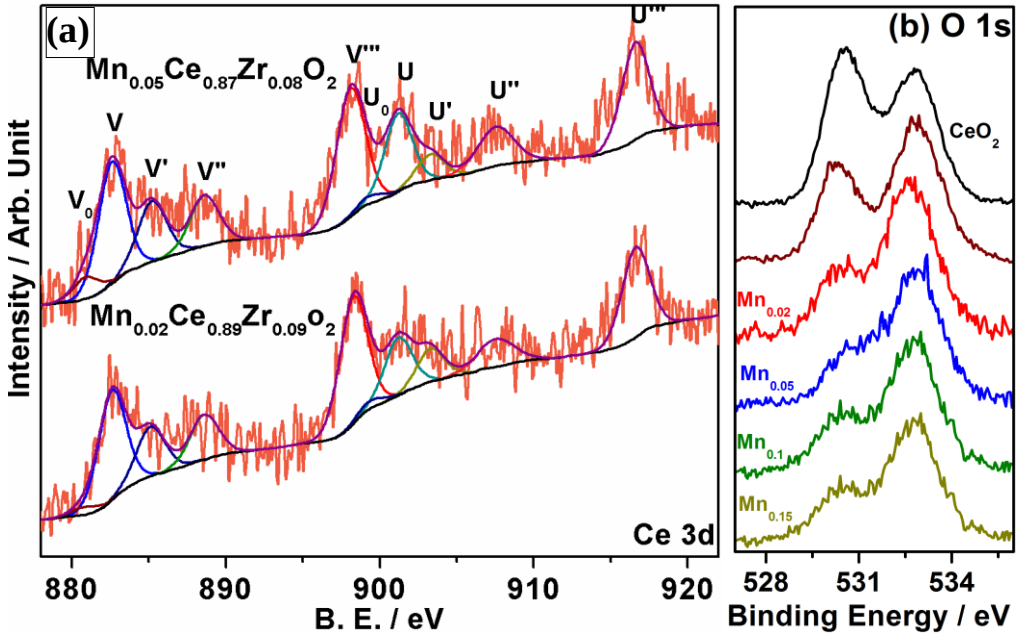

Fig. 4.6 (a) Ce 3d core level XPS spectra of $Mn_{0.02}Ce_{0.89}Zr_{0.09}O_2$ and $Mn_{0.05}Ce_{0.87}Zr_{0.08}O_2$ compositions. (b) XPS spectra recorded for O 1s core levels of $Mn_xCe_{1-x-y}Zr_yO_2$ thin films.

Zr 3d spectra are shown in Fig. 4.5b. BE of Zr $3d_{5/2}$ and $3d_{3/2}$ core levels for $Ce_{0.9}Zr_{0.1}O_2$ appears at 182.9 and 185.3 eV, respectively, indicating the oxidation state to be 4+.[36] Zr 3d features exhibit a gradual shift towards lower BE with increased Mn-doping; BE shift of -0.6 eV was observed with 15 % Mn-doping compared to that of CZ. Mn 2p spectra

are shown in Fig. 4.5c. BE of Mn $2p_{3/2}$ and $2p_{1/2}$ appears at 642.3 and 654.7 eV, respectively.[37-39] This observation confirms that Mn ions are present in +3 oxidation state. It is also observed that as the Mn-content increases from 2 to 15 %, the intensity of Mn 2p feature also increases, at the cost of other elements. A gradual change in the electronic environment and surface composition of MCZ with increasing Mn-content is evident from the above observations. The presence of Mn^{3+}, Zr^{4+}, Ce^{3+} and Ce^{4+} cations along with oxygen vacancies influence the redox properties of MCZ and hence the catalytic activity.

4.3.6 Oxygen adsorption on $Mn_xCe_{1-x-y}Zr_yO_2$

Kinetic results of O_2 adsorption and OSC as a function of temperature has been studied on MCZ thin films. Any MCZ thin film was reduced in H_2 at 700 K for 30 min. at a partial pressure of 1 x 10^{-7} Torr, between any two successive oxygen adsorption experiments; this is mainly to recover the initial surface quality of the sample and also to minimize the chance of any adsorbed oxygen present due to earlier experiment. Possible impurities (such as CO, CO_2, H_2O, H_2, amu 12 and 14) were also recorded to make sure that the thin films are not contaminated which is shown in Fig. 4.7. Other control experiments, such as O_2 adsorption on Si wafer, sample holder, were also carried out. Virgin Si wafer shows less than 10 % O_2 adsorption and sample holder do not show any adsorption. Since MCZ material is deposited to a thickness of 40-60 nm, no significant adsorption of O_2 is expected on Si wafer.

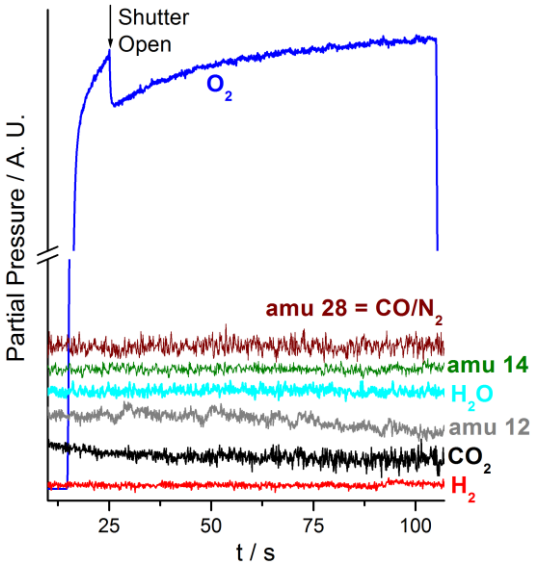

Fig. 4.7 Typical mass spectral results recorded while oxygen adsorption on MCZ surfaces with several mass species/fragments. Experimental traces are vertically shifted to avoid overlap. Results shown in the above figure is on $Mn_{0.05}Ce_{0.87}Zr_{0.08}O_2$is at 600 K.

Fig. 4.8 shows O_2 adsorption on $Mn_{0.15}Ce_{0.8}Zr_{0.05}O_2$ thin film. Typical MBI experiment is explained briefly in the following with reference to Fig. 4.8a. From the

beginnings of the experiment, all the relevant mass species present in the background were observed. At time t = 15 s, O_2 molecular beam was allowed in MBI chamber keeping the shutter in closed position, and it prevents exposure of MB directly to the surface of the catalyst. At t = 25 s, the shutter was opened and it allows a direct interaction of O_2 MB with the surface of MCZ catalyst. Oxygen adsorption from the background was not considered for any calculation between t = 15 – 25 s. At t = 25s, an instantaneous drop in partial pressure of O_2 was observed due to dissociative adsorption of O_2 on pre-reduced MCZ surfaces; this change in O_2 partial pressure gives information about sticking coefficient on MCZ surfaces.[40] The O_2 molecular beam was switched off at t= 105 s. It was observed that O_2 adsorption ceases within 25 s, after opening the shutter and below 500 K, indicating the occurrence of surface saturation; however, O_2 adsorption continues at t > 100 s at ≥ 700 K. Same rate of O_2 adsorption was observed at 800 K throughout the experiment. The extent of O_2 adsorption increases with increasing temperature underscores the diffusion of O-atoms into the sub-surfaces and possibly into the bulk of MCZ films. Oxygen diffusion continues till the catalyst is fully oxidized indicating the Mars van Krevelen (MvK)[41-43] mechanism is operative. Many reference experiments were measured by keeping the shutter in the closed position for the

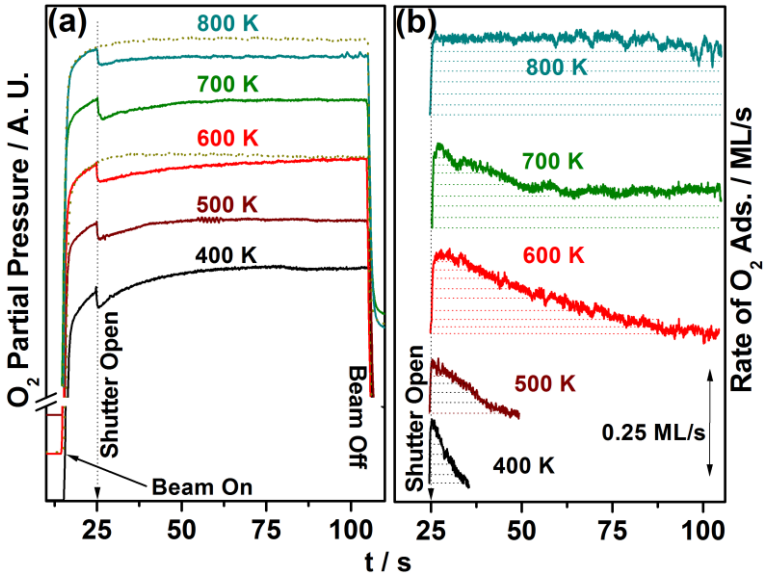

Fig. 4.8 (a) O_2 adsorption with respect to time as a function of temperature on $Mn_{0.15}Ce_{0.8}Zr_{0.05}O_2$ thin film. Reference experiment has been done after O_2 adsorption experiment with shutter in closed position and have been shown at temperature T = 600 K and 800 K. (b) Extent of O_2 uptake with respect to time as a function of temperature by subtracting amount of O_2 uptake from reference experiment. Oxygen coverage (θ_0) is area under curve indicated by dotted line.

entire experiment, but after completing the original oxygen adsorption experiment. Such reference experiments are shown for T = 600 and 800 K in Fig. 4.8a. A difference between

the adsorption and corresponding reference experiment gives the amount of oxygen adsorbed by the catalyst.

Quantification of adsorbed oxygen as a function of time is shown in Fig. 4.8b. A simple integration of the (dotted line) area gives the oxygen coverage (θ_0) or oxygen storage capacity (θ_{OSC}) measured at a particular temperature. This is calculated from the data shown in Fig. 4.8a. Calibration measurements carried out earlier was utilized to convert the above data into (cumulative) oxygen coverage; rate of oxygen adsorption etc.[44,45] It has been found that rate of oxygen adsorption increases as the temperature increases. θ_O measured at 400 K was considered to be a monolayer surface coverage and we assume this as a benchmark for surface saturation with O atoms and without any diffusion or minimum diffusion of O-atoms into subsurface and bulk of the catalyst. Fig. 4.8b shows that as temperature increases above 400 K, rate as well as the extent of oxygen adsorption increases gradually suggesting the onset of oxygen diffusion into the subsurfaces. With an increase in temperature, the initial sticking coefficient (s_0) on reduced MCZ surfaces increases which correspond to increase in oxygen adsorption. At 800 K rate of oxygen uptake was constant over an extended period of time (result not shown) with a marginal decrease in oxygen uptake above 360 s. Constant oxygen adsorption at same rate fully supports the precursor mediated surface adsorption model along with diffusion of oxygen atoms into the subsurface and bulk layers of the catalyst. Similar results were also observed for $Mn_{0.05}Ce_{0.87}Zr_{0.08}O_2$ and $Mn_{0.1}Ce_{0.85}Zr_{0.05}O_2$ thin film (results not shown) with only difference is rate of O_2 adsorption; rate of O_2 adsorption is less compared to $Mn_{0.15}Ce_{0.5}Zr_{0.05}O_2$ thin film.

Calculation of various parameters, such as s, s_0 and the total amount of oxygen uptake (θ_{OSC}) has been demonstrated in chapter 3, (Sec. 3A.3.7), our earlier publication and given in Fig. 4.9. The calculation procedure is simple and it involves subtraction of oxygen adsorption from the reference experiment. Time evolution of the surface coverage method adopted by Zaera et al[46,47] also give very similar result as that of subtraction method. More details about calculation method is given in sec. 3A.3.7 and readers are requested to refer the same. Fig. 4.9a shows direct oxygen adsorption at 600 K on $Mn_{0.15}Ce_{0.8}Zr_{0.05}O_2$ thin film and corresponding reference experiment, after surface saturation and/or without any direct oxygen adsorption. The difference between reference experiment and direct oxygen adsorption gives time evolution of oxygen adsorption, thus rate of oxygen adsorption as a function of time in Fig. 4.9b. Total amount of oxygen adsorbed or OSC (θ_{OSC}) (Fig. 4.9c) was calculated by integrating the area of oxygen adsorption (Fig. 4.9b).

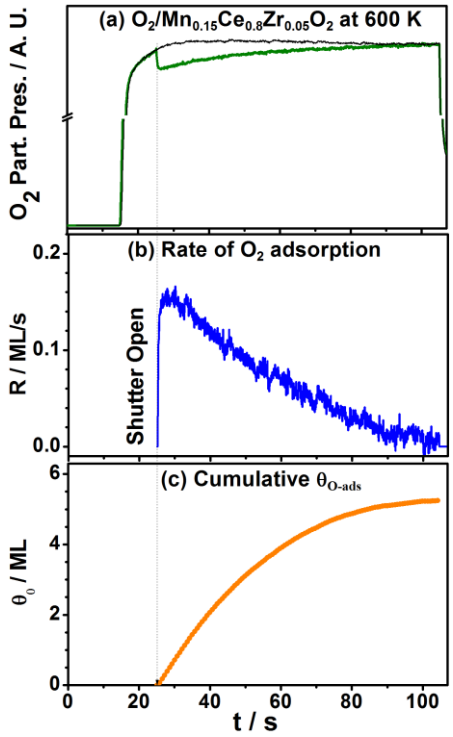

Fig. 4.9 (a) O_2 adsorption at T = 600 K on $Mn_{0.15}Ce_{0.8}Zr_{0.05}O_2$, (**b)** rate of oxygen adsorption as a function of time, (**c)** cumulative oxygen coverage with respect to time. Data in panels b and c is derived from the data given in panel a.

Cumulative sum of θ_0 versus adsorption time reveals that diffusion of oxygen atoms into subsurface/bulk is first order. Fig. 4.9b shows that at 600 K rate of oxygen adsorption as well as s was high (0.16±0.02) at the time of shutter opening, and it continues at the same rate unto t = 32 s. Similar type of desorption trend was observed at other temperatures also, which supports precursor mediated model of adsorption. Rate of O_2 adsorption starts to decline after t = 32 s, and no net oxygen adsorption was observed after t = 90 s; this indicates the saturation of top few layers of thin film at this temperature. 5±0.5 ML of oxygen adsorbed on $Mn_{0.15}Ce_{0.8}Zr_{0.05}O_2$ thin film indicated diffusion of adsorbed O atoms into subsurface as well as bulk layers of the material. Although diffusion of O-atoms is energy neutral, the same needs to be activated; activation of diffusion process begins above 500 K. It is also to be noted that oxygen adsorption occurs mainly to fill the oxygen vacancies and consequent oxidation of Ce^{3+} to Ce^{4+}. Although our experimental results give θ_{OSC}, the precise calculation of depth of oxygen diffusion into MCZ layers is difficult due to porosity associated with thin films. From a molecular beam study it has been found that $Mn_{0.15}Ce_{0.8}Zr_{0.05}O_2$ composition exhibits the highest oxygen adsorption capacity and OSC (see Fig. 4.11). Incidentally, $Mn_{0.15}Ce_{0.8}Zr_{0.05}O_2$also shows the highest activity towards

partial oxidation of CH_4, and hence results from this composition have been discussed in detail.

The sticking coefficient 's' is plotted against cumulative oxygen adsorption 'θ_0' and shown in Fig. 4.10 for $Mn_{0.15}Ce_{0.8}Zr_{0.1}O_2$ thin film. In fact, it is essentially the same data as that of Fig. 4.9b, but plotted versus θ_0 to get more insight. Close observation of it finds similar s value up to 1.3 ML fully supports the precursor mediated adsorption model and after that a decline in s indicating diffusion of O-atoms into the subsurface. The s_0 was observed to be the same (0.16±0.02) at temperatures between 600 and 800 K (Fig. 4.8b). While the adsorption probability remains almost constant throughout the experiment in the 800 K case, it does decreases with coverage (or time) at ≤700 K. The behaviour of oxygen adsorption is typical of precursor mediated adsorption and can be fitted to a Kisliuk-type equation.[48] At high temperatures, the rate of desorption (k_{des}) from the precursor state to that of migration (k_{mig}), ($K = k_{des}/k_{mig}$) was found to be low (<0.05). We also underscore that the migration, mentioned above, is predominantly into the subsurfaces and bulk of MCZ film, apart from surface diffusion. Nonetheless, the kinetics observed at lower temperatures increasingly changes towards Langmuir's model; the Kisliuk equation yields a value of K = 0.33 for the data in Fig. 4.10 at 600 K (inset in Fig. 4.10). It is also to be noted that the saturation coverage is assumed to be 1 and coverage data points are normalized for the Kisliuk fit.

Fig. 4.11 shows the plots of (a) s_0, and (b) θ_{OSC} as a function of temperature for MCZ thin films and $Ce_{0.90}Zr_{0.1}O_2$ (CZ). Arrhenius fashion plot is shown for the latter. It is to be underscored that the values measured and reported in this communication is within the experimental time of oxygen exposure for 80 s (Figs. 4.8). A high value of s_0 was observed over the entire temperature range for $Mn_{0.15}Ce_{0.8}Zr_{0.05}O_2$ over other MCZ compositions (Fig. 4.11a); nonetheless, > 600 K, $Mn_{0.10}Ce_{0.85}Zr_{0.05}O_2$ also shows a comparable s_0 within the experimental accuracy of 10 %. However, CZ shows significantly higher s_0 at high temperatures (≥ 600 K) than $Mn_{0.15}Ce_{0.8}Zr_{0.1}O_2$. Mn-doping in CZ lattice decreases the s appreciably.

θ_{OSC} increases at a slow pace unto 500 K, thereafter it increases linearly with temperature (Fig. 4.11b). This is facilitated due to increased diffusion of O-atoms into the subsurfaces and bulk layer at high temperatures. Arrhenius plots provide the activation energy (E_a) for O-diffusion, which is observed to be 11.5 (for 10 and 15 % Mn in MCZ), 14.5 (CZ) and 19.4 kcal/mol for $Mn_{0.05}Ce_{0.87}Zr_{0.08}O_2$. A change in slope for CZ and low Mn-containing indicates the onset of O-diffusion above 500 K. Likely, O-diffusion occurs at low temperatures on MCZ with high Mn- content. Although there is some difference in θ_{OSC}

between different compositions, it is not that significant to impact on reactivity. In other words, if θ_{OSC} is the only parameter that determines the catalytic activity, all MCZ composition might show similar activity. In view of this, thin films of all compositions have been evaluated for the partial oxidation of methane to explore the effect of MCZ compositions.

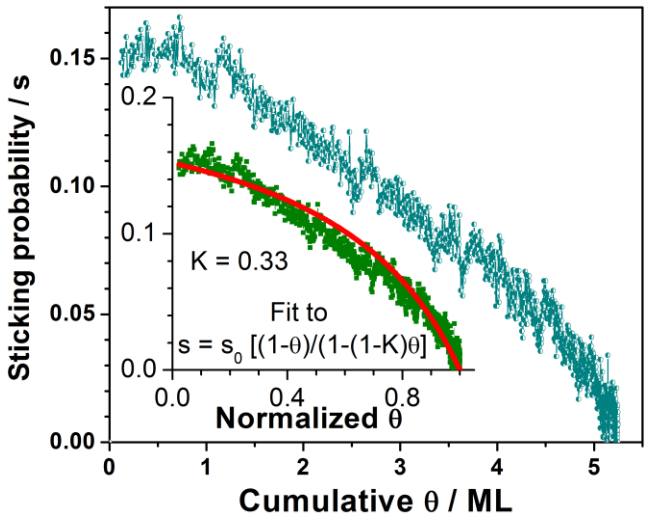

Fig. 4.10 Sticking coefficient vs. cumulative O_2 coverage from O_2 adsorption on $Mn_{0.15}Ce_{0.8}Zr_{0.05}O_2$ thin film at 600 K, and it was calculated from data shown in Fig. 11. Fit to the Kisliuk equation is shown in the inset. Note the saturation coverage is assumed to be 1 and coverage is normalized to that for the Kisliuk fit.

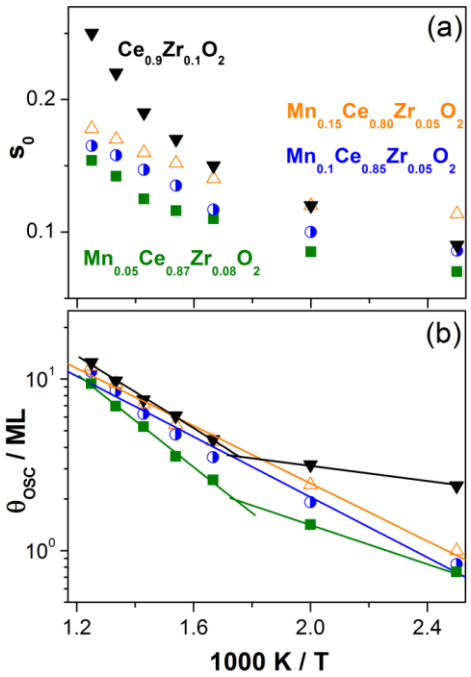

Fig. 4.11 (a) s_0 and (b) θ_{OSC}measured on $Mn_xCe_{1-x-y}Zr_yO_2$ thin films as a function of composition and temperature. θ_{OSC} is plotted in Arrhenius fashion, and 10 and 15 % Mn-containing MCZ composition shows the minimum activation energy for oxygen diffusion.

4.3.7 Molecular Beam study of partial oxidation of methane on MCZ

Kinetics of partial oxidation of methane with O_2 has been studied on MCZ thin films using collimated MB under ultra high vacuum (UHV) conditions. The purpose of the present study is also to draw mechanistic aspect of partial oxidation of methane occurring on MCZ thin film under high temperature and low contact time conditions. In fact, single collision condition is the primary aspect of MB. Methane activation measurements have been measured on same and different batches of MCZ thin films and the results are reproducible within the error limit. $Mn_{0.15}Ce_{0.8}Zr_{0.05}O_2$ thin film has been used for at least a month for various measurements and results are reproducible proves MCZ as a sustainable material.

Generally, two mechanistic pathways have been suggested for partial oxidation of methane to syngas. First one involves dissociative adsorption of reactants and the association

of different fragments on catalyst surface to desorb as different products (pyrolysis-oxidation) i.e. CO and H_2 (Eq. 4-6).[6-8,49]

$CH_4 \rightarrow C_s + 4H_s \ldots$ (4.4)

$C_s + O_s \rightarrow CO \ldots$ (4.5)

$H_s + H_s \rightarrow H_2 \ldots$ (4.6)

The second mechanism involves the formation of complete oxidation products and then they combine with CH_4through reformation pathway to form syngas (combustion-reformation (Eq. 7-8 and 3)).[14,50-55]

$CH_4 + 2O_2 \rightarrow CO_2 + 2H_2O$ ΔH = -802 KJ/Mol (4.7)

$CH_4 + H_2O \rightarrow CO + 3H_2 \ldots$ ΔH = +341 KJ/Mol (4.8)

In our study, we observe the combustion-reformation pathway predominantly, which is discussed below. A systematic study of C-H activation of methane was measured on MCZ films. Particularly, $Mn_{0.15}Ce_{0.8}Zr_{0.05}O_2$ composition is active ≥700 K for methane oxidation towards syngas, while lower Mn-content leads to total oxidation.

Fig. 4.12 shows the partial oxidation of methane at 650 K with CH_4:O_2 = 2:1 ratio on $Mn_{0.15}Ce_{0.8}Zr_{0.05}O_2$ thin film. Between any two successive CH_4 activation experiments, MCZ thin film was first oxidized in $O_2$for 10 min. followed by reduction in H_2 at 700 K for 30 min. each at a partial pressure of 1 x 10^{-7} Torr, to remove any carbon impurities left and recover the initial surface quality of the sample, respectively. Different CH_4:O_2 compositions have been evaluated and 2:1 ratio leads to more syngas than other compositions. Expectedly, oxygen-rich compositions lead to combustion. At the time of shutter opening (t = 40 s), O_2 adsorption begins and it continues to occur at the same rate, which is characterized by a decrease in the partial pressure of O_2 due to its consumption by the catalyst. There is no measurable adsorption of methane was observed; however, a gradual change in partial pressure of CH_4 observed was due to the chamber flushing effect, and it does not change the methane flux on the catalyst surfaces, under the measurement conditions. Very low s of CH_4 molecules on catalyst surfaces[11,52,56] also makes it difficult to follow its adsorption characteristics. There is no product formation observed ≤ 600 K, although O_2 adsorption occurs for about first two minutes, as shown in Fig. 4.8.

The first sign of C-H activation of methane was observed at 650 K. However, only combustion products (CO_2 and H_2O) were observed as shown in Fig. 8.12. Interestingly, H_2O (CO_2) was produced when the reactants were directly dosed (shutter was closed) on the MCZ surface. To explore the mutually exclusive formation of water and CO_2 while the shutter was

opened and closed, respectively, as well as to find out the optimum conditions for syngas production, a systematic temperature dependent methane activation was studied on MCZ surfaces and the results are described below.

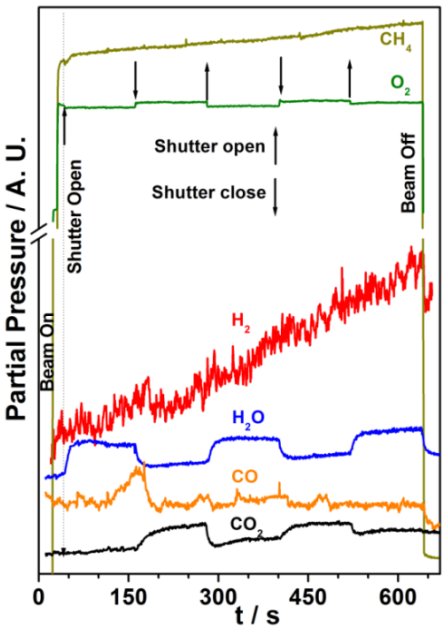

Fig. 4.12 Experimental kinetic data for partial oxidation of CH_4 and O_2 in 2:1 ratio at 650 K. The beam was blocked and unblocked after every 120 s for reproduction of kinetic data. CO and H_2 are not formed during this reaction at 650 K with exclusive production of CO_2 and H_2O.

Fig. 4.13 shows the kinetic results observed for partial oxidation of methane on (a) $Mn_{0.15}Ce_{0.8}Zr_{0.05}O_2$ at 700 K, and (b) $Mn_{0.10}Ce_{0.85}Zr_{0.05}O_2$ at 900 K. $Mn_{0.05}Ce_{0.87}Zr_{0.08}O_2$ thin film at 900 K also shows the similar result as that of Fig. 4.13b (not shown). Very similar to Fig. 4.12, water formation begins instantly by opening the shutter at t = 40 s on $Mn_{0.15}Ce_{0.8}Zr_{0.05}O_2$ surface (Fig. 4.13a), while other products (CO, CO_2 and H_2) were not observed. A large amount of O_2 adsorption was evident from a decrease in partial pressure, while methane shows no significant pressure change, as in 650 K (Fig. 14) experiment. It is also to be noted that water formation reaches the steady state after 45 s (13 s) at 700 K (650 K). Exclusive water formation occurs, while the shutter was open, reiterates the methane dissociation followed by interaction between H and O atoms, leaving all carbonaceous(C, CH_x) species on the catalyst surfaces. Continuous oxygen adsorption/diffusion into subsurfaces oxidizes the surface and enabling water formation, which was assisted by fast H-diffusion. Although H, O, C and CH_x species were available, exclusive water formation (through hydrogen oxidation) demonstrates its highly competing nature, over all other products formation, in the presence of oxygen. Even though enthalpy of H_2O (-241.8

KJ/mol), CO (-110.5 KJ/mol) or CO_2 (-393.5 KJ/mol) formation is favourable for all products, suppression of latter molecules production is attributed to the nature of $Mn_{0.15}Ce_{0.8}Zr_{0.05}O_2$ catalyst.

On closing the shutter under steady state conditions at t = 160 s, water formation ceases to a low rate, while other three products formation begins afresh and slowly it reaches a new steady state in the next one minute. While CO and CO_2 reach the new steady state quickly, H_2 appears to reach the steady state very slowly.[57,58] Attaining the steady state of H_2 was very slow, compared to CO or CO_2, and this may be due to any combination of the following three reasons. (a) Water produced might be consumed by C and CH_x species to produce syngas (Eq. 4.8). (b) H_2 could be stored in MCZ lattices/pores, and hence partly reducing the catalyst surfaces. Indeed, ceria and metal-ion doped ceria are known for H_2storage. (c) Formation of CO and CO_2 in the absence of oxygen indicates the utilization of oxygen that was stored in MCZ lattice in the first part of direct dosing of CH_4 + O_2. Characteristically slow (fast) increase in H_2 (CO_x) production, by closing the shutter, suggests the requirement of reduced MCZ surfaces for H_2 generation. In other words, carbon species consumes the lattice oxygen, which leads to the reduction of MCZ and consequently helps to produce hydrogen. Water formation is either suppressed or consumed for steam reforming (Eq.4.8) under the above conditions highlighting its cooperating nature to generate hydrogen. The blocking and unblocking of MB is repeated to reproduce the kinetic data of the experiment. Each data was reproduced at least three times, and they reproduce well within the experimental uncertainty.

A careful look at the data of evolution of products, as a function of time, demonstrates an increase in the background pressure of all products. Indeed, this is entirely attributed to the slow diffusion of products from the porous thin films. However, the major changes observed in partial pressure of products upon closing/opening the shutter are due to MB. This fully supports the diffusion of reactants as well as products; however, the rate values reported later (in Fig. 4.15) was measured only from the MB oscillations. An important point to be noted is on the dry reforming: On opening the shutter second time (t = 280 s, Fig. 4.13a), H_2, CO, CO_2 partial pressure did not reach the background level and remains at significantly appreciable level. This implies the generation of CO_2, while dosing reactants, and its simultaneous consumption for dry reforming with methane (Eq. 4.3). In other words, part of the amount of CO_2 generated under direct dosing conditions is converted to H_2 and CO; however, this occurs only after first MB oscillation. A continuous increase in the background intensity of all the products underscores the diffusion controlled nature of the reaction and the

necessity to vary the contact time to achieve the desired products. Further careful studies are required to gain more insight on the reaction aspects to propose a suitable kinetic model.

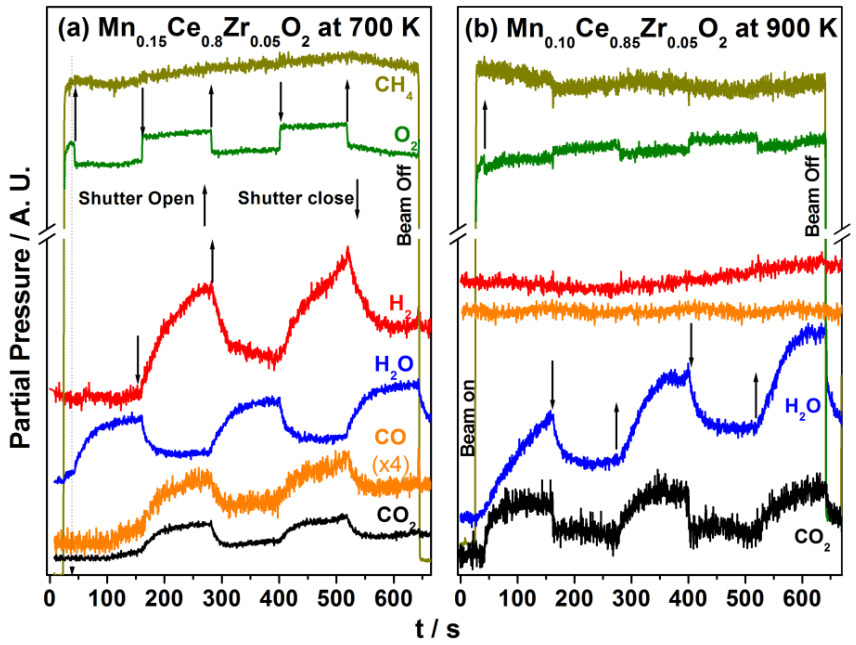

Fig. 4.13 Experimental data for partial oxidation of CH_4 with O_2 in 2:1 ratio, on (a) $Mn_{0.15}Ce_{0.8}Zr_{0.05}O_2$ at 700 K, and (b) $Mn_{0.10}Ce_{0.85}Zr_{0.05}O_2$ at 900 K. The beam was blocked and unblocked after every 120 s. Note the mutually exclusive formation of water or a mixture of CO_2, CO and H_2 products while opening or closing the shutter to allow or block the reactants in molecular beam, respectively, in panel a. Panel b shows a typical combustion products formation. Products traces are vertically shifted to avoid overlap and for better clarity.

Five points are worth noting from the above results: (1) Formation of syngas at 700 K from methane highlights the C-H activation at such low temperatures and underscores the role of Mn. Indeed, there is no C-H oxidation occurs on CZ surfaces below 900 K as shown in Fig.4.14. (2) Exclusive H_2O formation occurs at the expense of other products (CO_2 + CO + H_2), when the molecular beam of reactants (CH_4 + O_2) is allowed to react on $Mn_{0.15}Ce_{0.8}Zr_{0.05}O_2$ surfaces. Similarly, when the molecular beam is blocked, exactly the opposite trend of formation of CO_2 + CO + H_2 products occurs, at the expense of water. This indicates the competition as well as cooperation among the different elementary reactions. For example, H_2 gets oxidized to water or simply desorbed as H_2, while reactants were allowed or blocked, respectively. (3) Although Ce-based catalysts are well-known for efficient CO oxidation at 700 K, no CO_2 formation under shutter open conditions with a high rate of O_2 adsorption underscores its consumption towards dry-reforming (Eq. 4.3).[6-8,14]

In other words, CO_2 produced under the above condition was consumed, at least partially. Very likely, carbon could be diffusing into the subsurfaces and bulk while the shutter is open; this is supported by slow production kinetics of CO_x upon closing the shutter.

Possibly CH_x species could be deposited at the oxygen vacancy sites. The rate of oxygen adsorption remains the same in the transient and steady-state supports the diffusion of carbon

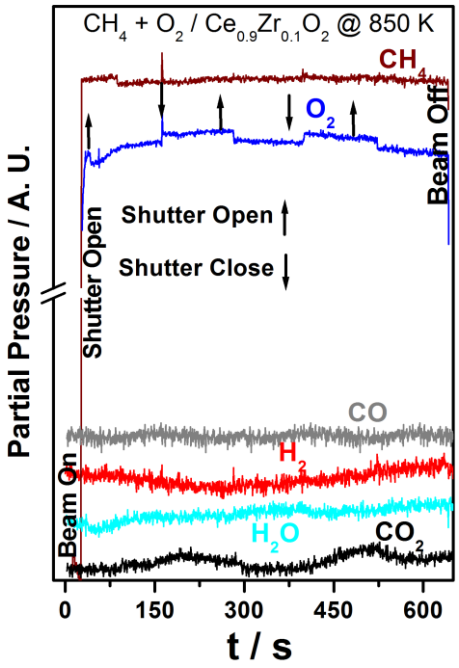

Fig. 4.14 Methane oxidation carried out on CZ surface at 850 K. Although oxygen adsorption occurs, no significant oxidized products or syngas species are observed hints the inactive nature of CZ surface up to 900 K.

into subsurfaces; any significant deposition of coke formation on the surface would reduce the oxygen uptake, especially in the absence of CO_x formation (Fig. 4.13a). (4) Continuous oxygen adsorption under steady-state reaction conditions was indicating the diffusion of O atoms into the bulk while oxygen vacancies were moving towards the surface and keeping the surface amenable for reaction. (5) Production of syngas components demonstrates the combustion-reformation pathway for methane activation. A simple addition of Eqns. 4.3, 4.7-4.8 leads to Eq. 4.9 and a slight modification leads to Eq. 4.10. Both equations are exothermic, which makes the production of H_2-rich syngas possible.

$3CH_4 + 2O_2 \rightarrow 3CO + 5H_2 + H_2O$ … $\Delta H = -214$ KJ/Mol (4.9)

$4CH_4 + 3O_2 \rightarrow 3CO + CO_2 + 7H_2 + H_2O$ … $\Delta H = -532.6$ KJ/Mol (4.10)

In total contrast to the results observed on $Mn_{0.15}Ce_{0.8}Zr_{0.05}O_2$surfaces, exclusive and simultaneous formation of combustion products occurs on $Mn_{0.10}Ce_{0.85}Zr_{0.05}O_2$(and $Mn_{0.05}Ce_{0.87}Zr_{0.08}O_2$) surfaces at 900 K (Fig. 4.13b). There is no significant reaction occurs up to 800 K on MCZ surfaces, that contains ≤10 % Mn. Although there is a minor change in Ce and Zr content in the above compositions, they are not expected to influence the reaction significantly. High Mn-content apparently plays a critical role towards combustion-reformation pathway. It is worth noting a significantly high rate of

oxygen adsorption on $Mn_{0.15}Ce_{0.8}Zr_{0.05}O_2$ surfaces even at 700 K, than other surfaces at 900 K, under reaction conditions. This also suggests a possible coking of MCZ compositions with low Mn-content. This is further confirmed from the similar amount (1.5%) of coke deposition after 0, 30 and 60 min. Ar^+-sputtering of $Mn_{0.02}Ce_{0.89}Zr_{0.09}O_2$ composition. Very low adsorption probability of methane could be another reason.

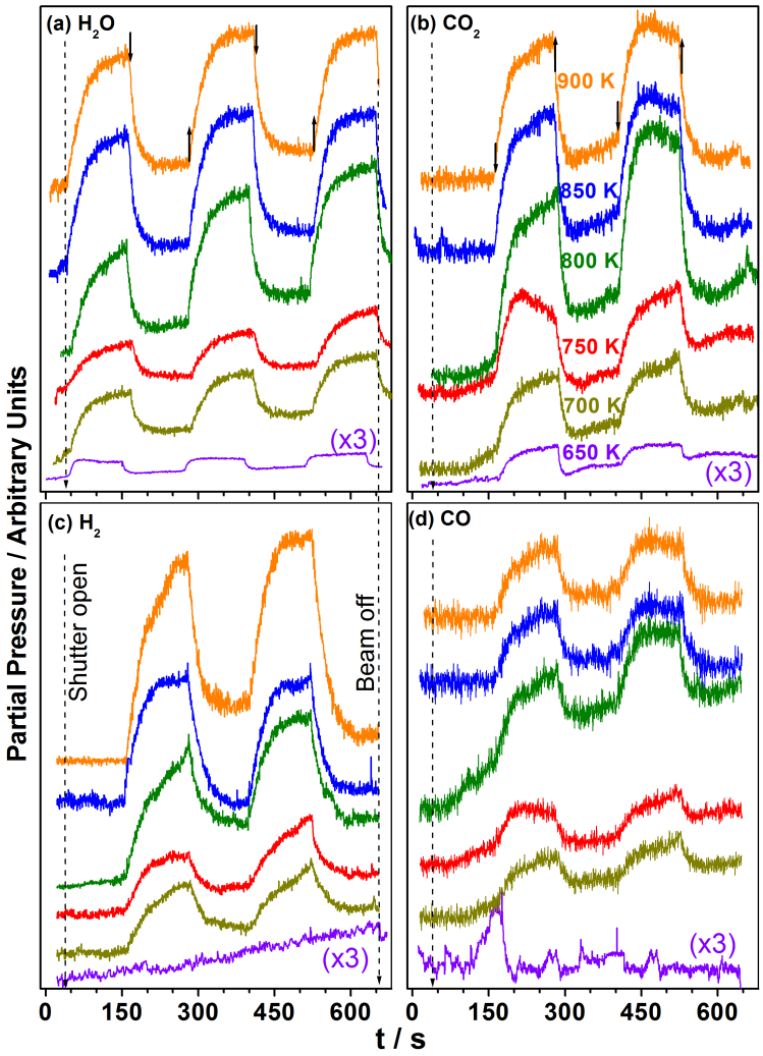

Fig. 4.15 Effect of temperature on formation of combustion products (a) H_2O, and (b) CO_2, and syngas products (c) H_2 and (d) CO. While H_2 production increases linearly with temperature, CO production shows an optimum at 800 K. Dashed arrow indicates the initial shutter open and beam shut off at the end of reaction. Up and down arrows indicates the shutter close and open positions, respectively.

In view of the syngas formation, $Mn_{0.15}Ce_{0.8}Zr_{0.05}O_2$ catalyst was evaluated at different temperatures for partial oxidation of methane. Except for temperature, the reaction was carried out under identical conditions. Fig. 4.15 shows the temperature dependence of products evolution from the partial oxidation of methane. Results are presented in a compact manner mainly to minimize the complexity of the reaction trend. It has been found that as the

reaction temperature increases, the rate of formation of H_2O, CO and CO_2 increases linearly up to 800 K, and then a marginal decrease in the rate was observed. In contrast, H_2 production increases linearly with increasing temperature. Further, H_2 production reaches the steady state faster at high temperatures. Suppression of water formation and an increase in H_2 production at high temperatures correlates well. Due to the diffusion-controlled nature of the reaction, some of the products (CH_x, CO_2, H_2O) formed could be possibly consumed to produce H_2 selectively. Indeed Eqns. 4.3 and 4.8 given earlier are the possible mechanistic steps that help to produce more H_2.

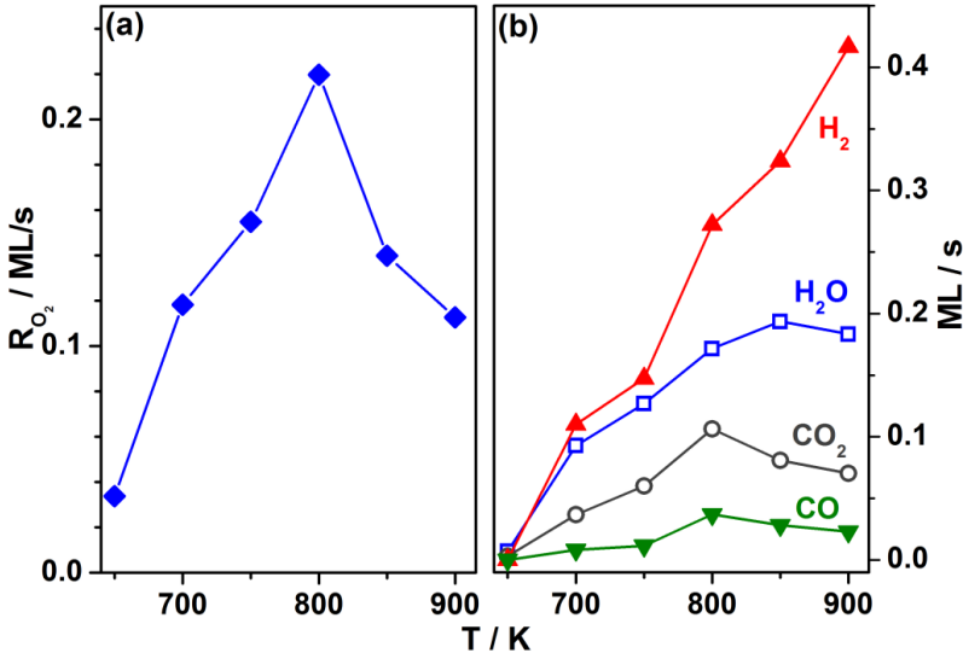

Fig. 4.16 (a) Rate of oxygen adsorption measured under steady state reaction condition on $Mn_{0.15}Ce_{0.8}Zr_{0.05}O_2$. (b) Rate of formation of combustion-reformation products plotted as a function of temperature on $Mn_{0.15}Ce_{0.8}Zr_{0.05}O_2$ thin film.

A careful evaluation of oxygen uptake under steady state conditions reveals the temperature dependence of the rate of oxygen adsorption. Fig. 4.16 shows, (a) the rate of oxygen adsorption, and (b) rate of various products formation. In fact, the ratio of H-containing products to that of carbon is higher than 4 (expected from methane) highlighting the fast out-diffusion of $H_2$and some inevitable carbon (and oxygen) diffusion or deposition in the bulk/pores. Efforts will be made to carry out the measurements at ambient pressure with MCZ powder catalysts in fixed bed reactors. A significant change in oxygen consumption is observed when the temperature varies from 650 to 700 K. In fact, it further increases up to 800 K, before it declines with a further increase in temperature. Except H_2, other oxidized products (CO, CO_2 and H_2O) shows the maximum rate between 800 and 900 K, is in agreement with the rate of O_2 adsorption.

4.4 Surface nature of spent $Mn_{0.15}Ce_{0.8}Zr_{0.05}O_2$ catalyst

XPS spectra of $Mn_{0.15}Ce_{0.8}Zr_{0.1}O_2$ thin film were recorded for O 1s, Ce 3d and C 1s core levels, after performing partial oxidation of methane between 750 and 1050 K, and the results are shown in Fig. 4.17. There is no significant change in the BE of Zr 3d and Mn 2p core levels observed, either before or after the reaction, and the results are shown in Fig. 4.18. However, change in O 1s, Ce 3d and C 1s spectra are observed. Compared to the O 1s spectrum recorded on as-prepared MCZ thin film (Fig. 4.6b), BE of lattice oxygen shifts marginally by 0.2 eV and appears at 530.0 eV (Fig. 4.17a), while the O 1s component at 532.8 eV was shifted to 532.3 eV and decreased in intensity. Spectral deconvolution demonstrates the presence of third oxygen feature at 531 eV, which is attributed to oxygen that is closer to oxygen vacancy sites. Oxygen vacancy feature increases at the expense of OH feature. Indeed, this suggests a diffusion of O-vacancies from bulk to the surface, and a change in surface electronic structure and composition is inevitable.

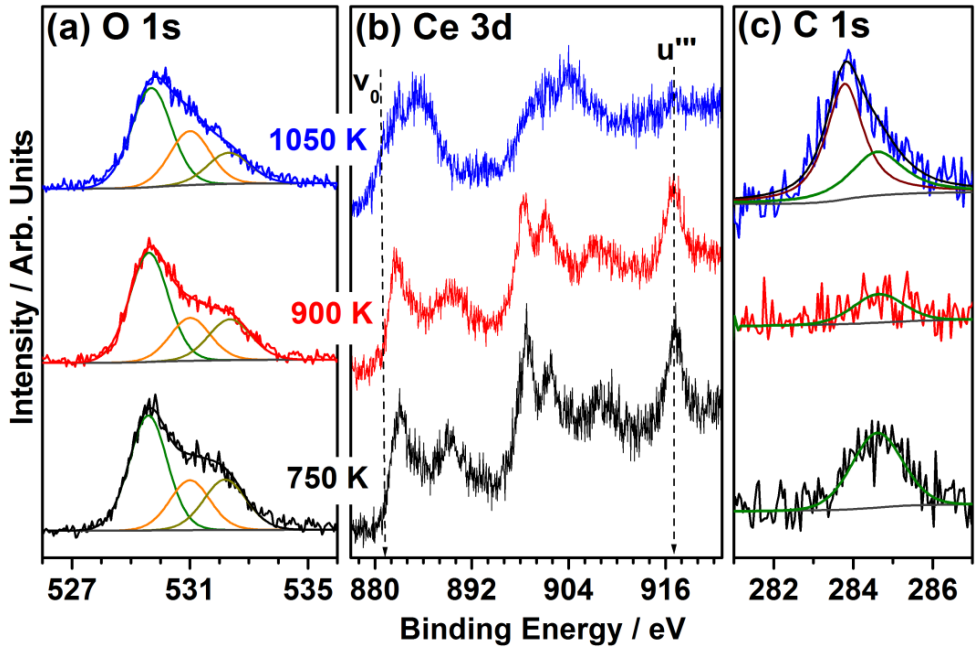

Fig. 4.17 XPS spectra recorded at room temperature for a) O 1s, b) Ce 3d, and (c) C 1s core levels of $Mn_{0.15}Ce_{0.8}Zr_{0.05}O_2$ after partial oxidation of methane measured at various temperatures.

Fig. 14.17b shows a large change in Ce 3d spectra on heating to high temperatures in the presence of $CH_4 + O_2$. As the reaction temperature increases the extent of reduction also increases. Line broadening occurs on increasing the temperature from 750 to 1050 K. Although all the spectra were recorded at room temperature, substantial broadening observed for the surface heated at 1050 K is due to predominant Ce^{3+} concentration on the surface.

Even though the surface was exposed to ambient atmosphere while transferring the $Mn_{0.15}Ce_{0.8}Zr_{0.1}O_2$from MBI to XPS unit, large Ce^{3+} observed suggest the stability of the reduced surfaces. This also indicates a significant number of oxygen vacancy sites associated with Ce^{3+} sites.

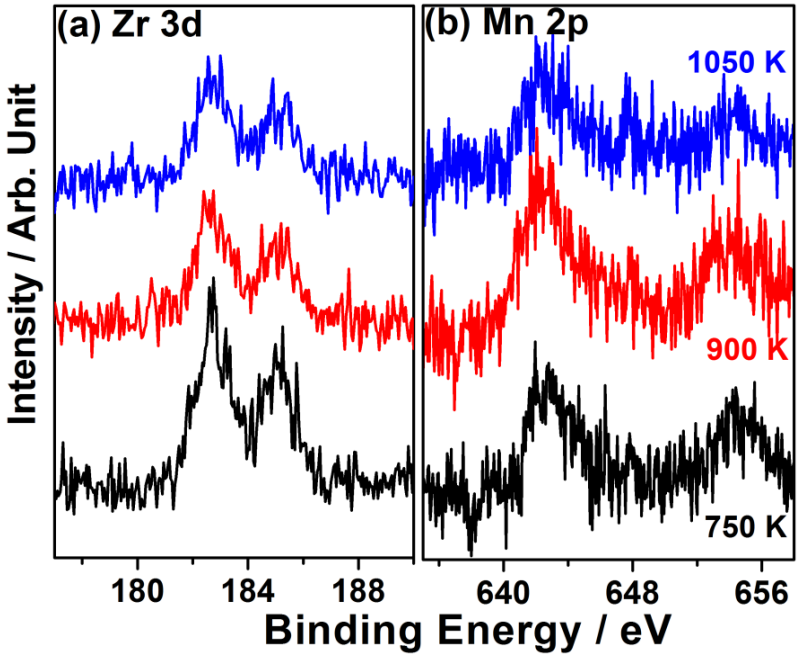

Fig. 4.18 XPS Spectra of a) Zr 3d and b) Mn 2p of $Mn_{0.15}Ce_{0.8}Zr_{0.05}O_2$ at various reaction temperatures.

Fig. 4.17c shows C 1s core level spectra after the reaction. Feature observed at 284.7 eV is attributed to CH_x species present on the surface,[59,60] which is observed at all temperatures. Indeed, very low intensity observed after the reaction at 900 K suggests a better oxidation and less deposition of carbon around 900 K. Although CH_x content is low after reaction at 1050 K, graphitic carbon (283.8 eV) appears prominently suggesting the increased carbon deposition, which decreases the activity at high temperatures. A high rate of oxygen adsorption and low carbon contamination at 900 K is in good agreement with the kinetic results.

4.5 Conclusion

Porous $Mn_xCe_{1-x-y}Zr_yO_2$ thin films were prepared by a combination of sol-gel and spin coating method and evaluated for C-H activation of methane. This is also a first step towards addressing the material gap for an extremely complicated reaction on working catalyst. Interesting observations were made, and conclusions were derived from the molecular beam data on oxygen adsorption, and C-H activation of methane on MCZ thin films. Although the OSC of all MCZ compositions is similar, C-H activation of methane to syngas on $Mn_{0.15}Ce_{0.8}Zr_{0.05}O_2$ is attributed to a few important factors. While simple combustion reaction

takes place on other MCZ compositions, $Mn_{0.15}Ce_{0.8}Zr_{0.05}O_2$ shows combustion-reformation pathway to syngas. A characteristic new observation on elementary reactions is of paramount importance for syngas formation with $Mn_{0.15}Ce_{0.8}Zr_{0.05}O_2$. While water formation occurs during the direct exposure of reactants, syngas along with CO_2 production occurs when the reactants are blocked from interacting with the catalyst surface. This underscores the spontaneous water formation in the presence of oxygen. Notably, hydrogen desorption requires reduced MCZ sites, which is fully supported by slow desorption kinetics. This particular aspect needs to be further investigated by site-specific structural/spectroscopy/microscopy methods. While the entire reaction is diffusion controlled, desorption of syngas highlights the prevailing dry-reforming conditions under beam blocking conditions. At least, part of CO_2 produced reacts with CH_x to generate syngas under beam blocking conditions. Above findings underscores the competition as well as cooperation among the different elementary reactions, depending on the experimental conditions. Sustainability of the reaction for two minutes while blocking the reactants from direct exposure to catalyst surfaces demonstrates the diffusion of CH_x species to subsurfaces and bulk. It is possible that CH_x species occupies oxygen-vacancy sites and diffuses into the bulk; however, more detailed work is required to confirm this hypothesis.

4.6 References

1. IEA (http://www.iea.org).
2. T. S. Alhbrandt, *Int. Geol. Rev.* **2002**, *44*, 1092.
3. D. R. Lide, (Ed.), *CRC handbook of chemistry and physics*, CRC Press, **2005**.
4. C. T. Au, M. S. Liao, C. F. Ng, *J. Phys. Chem. A* **1998**, *102*, 3959.
5. T. V. Choudhary, D. W. Goodman, *J. Mol. Chem. A* **2000**, *163*, 9.
6. D. A. Hickman, L. D. Schmidt, *Science* **1993**, *259*, 343.
7. D. Pakhare, J. Spivey, *Chem. Soc. Rev.* **2014**, *43*, 7813.
8. V. Subramanian, E. S. Gnanakumar, D-W. Jeong, W-B. Han, C. S. Gopinath, H-S. Roh, *Chem. Commun*. **2013**, *49*, 11257.
9. F. Cavani, N. Ballarini, A. Cericola, *Catal. Today* **2007**, *127*, 113.
10. V. R. Choudhary, A. S. Mammon, S. D. Sansare, *Angew. Chem. Int. Ed.* **1992**, *31*, 1189.
11. J. N. Wilson, F. Zaera, *J. Phys. Chem. C* **2010**, *114*, 16946.
12. T. Sasaki, K. Nakao, K. Tomishige, K. Kunimori, *Appl. Catal. A* **2007**, *328*, 140.
13. S. Velu, K. Suzuki, C. S. Gopinath, *J. Phys. Chem. B* **2002**, *106*, 12737.
14. R. Horn, K. A. Williams, N. J. Degenstein, L. D. Schmidt, *J. Catal.* **2006**, *242*, 92.
15. A. S. Larimi, S. M. Alavi, *Int. J. Chem. Eng. Appl.* **2012**, *3*, 6.

16. S. Velu, K. Suzuki, M. Vijayaraj, S. Barman, C. S. Gopinath, *Appl. Catal. B: Environ.* **2005**, *55*, 287.
17. E. Mamontov, T. Egami, R. Brenzy, M. Koranne, S. Tyagi, *J. Phys. Chem. B* **2000**, *104*, 11110.
18. E. Aneggi, C. de Leitenburg, A. Trovarelli, *Catal. Today* **2012**, *181*, 108.
19. S. Pengpanich, V. Meeyoo, T. Riksomboon, K. Bunyakiat, *Appl. Catal. A: Gen.* **2002**, *234*, 221.
20. V. Polshettiwar, T. Asefa, *Nanocatalysis Synthesis and Applications, John Wiley & Sons, Weinheim*, **2013**.
21. K. Sivaranjani, A. Verma, C. S. Gopinath, *Green Chem.* **2012**, *14*, 461.
22. S. S. Negi, K. Sivaranjani, A. P. Singh, C. S. Gopinath, *Appl. Catal. A: Gen.* **2013**, *452*, 132.
23. P. Devaraji, N. K. Sathu, C. S. Gopinath, *ACS Catal.* **2014**, *4*, 2844.
24. S. S. Negi, A. T. Venugopalan, T. Raja, A. P. Singh, C. S. Gopinath, *RSC Adv.* **2014**, *4*, 57087.
25. N. R. Shiju, M. A. Kumar, S. P. Mirajkar, C. S. Gopinath, C. V. Satyanarayana, B. S. Rao, *J. Catal.* **2005**, *230*, 484.
26. A. Pandikumar, K. Sivaranjani, C. S. Gopinath, R. Ramaraj, *RSC Adv.* **2013**, *3*, 13390.
27. M. Saini, K. Vivekanand, P. Poddar, K. V. G. K. Murty, K. S. Thushara, C. S. Gopinath, *Int. J. Nanotech.* **2010**, *7*, 919.
28. C. S. Gopinath, F. Zaera, *J. Catal.* **1999**, *186*, 387.
29. K. Thirunavukkarasu, K. Thirumoorthy, J. Libuda, C. S. Gopinath, *J. Phys. Chem. B* **2005**, *109*, 13283.
30. B. Murugan, A. V. Ramaswamy, D. Srinivas, C. S. Gopinath, V. Ramaswamy, *Chem. Mater.* **2005**, *17*, 3983.
31. T. Mathew, K. Sivaranjani, E. S. Gnanakumar, Y. Yamada, T. Kobayashi, C. S. Gopinath, *J. Mater. Chem.* **2012**, *22*, 13484.
32. S. A. C. Carabineiro, S. S. T. Bastosa, J. J. M. Orfao, M. F. R. Pereira, J. J. Delgado, J. L. Figueiredo, *Appl. Catal. A: Gen.* **2010**, *381*, 150.
33. J. Rynkowski, J. Farbotko, R. Touroude, L. Hila, *Appl. Catal. A: Gen.* **2000**, *203*, 335.
34. T. Rajesh, A. K. Rajarajan, C. S. Gopinath and R. N. Devi, *J. Phys. Chem. C* **2012**, *116*, 9526.
35. S. Kato, M. Ammann, T. Huthwelker, C. Paun, M. Lampimaki, M. T. Lee, M. Rothensteiner, J. van Bokhoven, *Phys. Chem. Chem. Phys.* **2015**, *17*, 5078.

36. S. Velu, K. Suzuki, C. S. Gopinath, H. Yoshida, T. Hattori, *Phys. Chem. Chem., Phys.* **2002**, *4*, 1990.
37. V. L. Joseph Joly, P. A. Joy, S. K. Date, C. S. Gopinath, *Phys. Rev.B* **2002**, *65*, 184416/1.
38. J. He, G. K. Reddy, S.W. Thiel, P. G. Smirniotis, N. G. Pinto, *J. Phys. Chem. C* **2011**, *115*, 24300.
39. B. Murugan, D. Srinivas, C. S. Gopinath, V. Ramaswamy, A. V. Ramaswamy, *ActaMaterialia* **2008**, *56*, 1461.
40. D. A. King, M. G. Wells, *Surf. Sci*. **1972**, *29*, 454.
41. C. S. Gopinath, F. Zaera, *J. Phys. Chem. B.* **2000**, *104*, 3194.
42. S. Nagarajan, K. Thirunavukkarasu, C. S. Gopinath, *J. Phys. Chem. C* **2009**, *113*, 7385.
43. S. Nagarajan, K. Thirunavukkarasu, C. S. Gopinath, J. Counsell, L. Gilbert, M. Bowker, *J. Phys. Chem. C* **2009**, *113*, 9814.
44. F. Zaera, C. S. Gopinath, *J. Mol. Catal. A: Chem.* **2001**, *167*, 23.
45. F. Zaera, C. S. Gopinath, *J. Chem. Phys.* **2002**, *116*, 1128.
46. C. S. Gopinath, F. Zaera, *J. Catal.* **2001**, *200*, 270.
47. S. Nagarajan, K. Thirunavukkarasu, C. S. Gopinath, S. D. Prasad, *J. Phys. Chem. C* **2011**, *115*, 15487.
48. P. J. Kisliuk,*J. Phys. Chem. Solids***1957**, *3*, 95.
49. D. I. Iordanoglou, A. S. Bodke, L. D. Schmidt, *J. Catal.* **1999**, *187*, 400.
50. B. C. Enger, R. Lodeng, A. Holmen, *Appl. Catal. A: Gen.* **2008**, *346*, 1.
51. A. P. E. York, T. C. Xiao, M. L. H. Green, J. B. Claridge, *Catal. Rev. Sci. Eng.* **2007**, *49*, 511.
52. T. Liu, C. Snyder, G. Veser, *Ind. Eng. Chem. Res.* **2007**, *46*, 9045.
53. A. Donazzi, A. Beretta, G. Groppi, P. Forzatti, *J. Catal.* **2008**, *255*, 241.
54. M. Maestri, D. Vlachos, A. Beretta, P. Forzatti, G. Groppi, E. Tronconi, *Top. Catal.* **2009**, *52*, 1983.
55. *CRC Handbook of Chemistry and Physics*, 85th Ed., Lide, D. R., Ed.; CRC Press: Boca Raton, FL, **2004**.
56. J. Chen, C. Yao, Y. Zhao, P. Jai, *Int. J. Hyd. Energy* **2010**, *35*, 1630.
57. L. Jalowiecki-Duhamel, A. Ponchel, C. Lamonier, *Int. J. Hyd. Energy*, **1999**, *24*, 1083.
58. L. Jalowiecki-Duhamel, *Int. J. Hyd. Energy* **2006**, *31*, 191.
59. S. G. Gholap, M. V. Badiger, C. S. Gopinath, *J. Phys. Chem. B* **2005**, *109*, 13941.
60. T. Mathew, B. S. Rao, C. S. Gopinath, *J. Catal.* **2004**, *222*, 107.

Chapter 5 – In-situ preparation of random morphology spinel Co_3O_4 and its activity evaluation for ambient CO-Oxidation

Spinel cobalt oxide (Co_3O_4) has been prepared in-situ in Molecular Beam Instrument (MBI) directly on Co-Metal foil. Spinel cobalt oxide is formed by dosing 5 x 10^{-6} Torr of molecular O_2gas directly onto the surface of Co-foil at 600 K. Formation of spinel cobalt oxide on cobalt metal foil is confirmed XRD and Raman spectroscopy. CO oxidation has been measured on $Co_3O_4$with various ratios of CO : $O_2$and between 275 and 500 K. It has been found that CO oxidation activity occurs at 275 K; this confirms the low temperature CO-oxidation on spinel cobalt oxide even with random morphology. It has been found that CO:O_2 = 1:3 ratio is the optimum reactants composition for the reaction to occur on the spinel surface. It has also been observed that the rate of the reaction increases marginally with an increase in reaction temperature. Although FE-SEM results show that no definite morphology (or random morphology) is present onto the surface of the spinel catalyst, it is able to catalyze low-temperature CO oxidation. These observations signify that the low-temperature CO oxidation occurs in the absence of nanorod morphology too, as against the literature reports. Apparently the rate of CO oxidation reaction is dependent on Co^{3+}content present on the surface of the catalyst.

5.1 Introduction

With increase in the population of the world industrialization, transport facility increases, and this causes the emission of large amount of greenhouse gases. It is necessary to keep a check on this greenhouse gas emission, in a way to find a method which can maintain the proper level of these gases in the atmosphere. Plying automobiles on the road discharges exhaust gases consisting harmful CO, NO_x along with small amount of unburnt hydrocarbons into the atmosphere, which needs to be converted to innocuous gases such as CO_2, N_2 and H_2O.[1,2] For the last few decades noble metal based catalysts, i.e. Pt, Pd, Rh[3-6] has been generally used in three way catalytic reactors, which are also very costly. Three way catalytic reactors need to be replaced with cost-effective materials which can perform alike noble metals in similar conditions. In lieu of this several nanomaterials have been synthesized which can work as a better catalyst for CO oxidation, NO_x and hydrocarbon conversion such as ceria-zirconia, copper-ceria zirconia mixed oxide.[7,8] Non-noble metal based catalysts can also work in high-temperature environment because of their facile oxygen mobility under technically relevant conditions. Many studies have also been carried out on single crystal under in-situ condition to study the kinetics aspects of CO oxidation. Nagarajan et al. reported CO oxidation on Pd (111)[9] single crystal and discussed the kinetics as well as various surface science parameter in details. Several studies have been reported on CeO_2, $Ce_{1-x}Zr_xO_2$, nobel metal supported on alumina, etc. and single crystal like Pd, Rh, etc which claim to have maximum conversion for CO oxidation.[10-13]

CO oxidation is of utmost importance not only because of its relevance to three-way catalytic converter,[14,15] purification of air,[16] but also to study the mechanistic aspect of reaction on the catalyst surface. Among these catalysts, $Co_3O_4$and nanogold based catalysts demonstrates CO oxidation at ambient temperatures and below.[16,17] Co_3O_4 is not much active at high temperature like platinum group metals(PGM), since at high temperatures in the presence of plenty of water vapour it gets converted back to CoO, as it loses oxygen at this temperature, which is less active for CO oxidation.[18] Spinel cobalt oxide is known for low-temperature CO oxidation, and it catalyzes the CO oxidation reaction below room temperature.

Few studies have been reported on low-temperature CO oxidation reaction on spinel cobalt oxide. Xie et al[17] prepared Co_3O_4 nanorod by calcination of cobalt hydroxide carbonate precursor and it shows CO oxidation activity with 100 % conversion even at 200 K; this catalyst shows CO oxidation with a normal feedstock of gas containing few ppm moisture. Gu et al[19] prepared mesoporous CoO and Co_3O_4 material and found that 50 % of

CO oxidation happens for Co_3O_4 below 223 K under normal and dry feedstock of gas; while CoO shows no activity at temperature below 323 K with normal feedstock, however, under dry gas condition it shows U-shaped curve with 22 % CO conversion at 328 K. It has been confirmed from several studies that presence of moisture,[20] NO[6] and hydrocarbon[20] slows down the rate of low-temperature CO oxidation. Several studies have been reported where it shows maximum activity for spinel cobalt oxide system in the literature.[21] All these reports suggests that Co^{3+} present in octahedral site is the active form for catalyzing CO oxidation, which has spinel structure; while CoO has rock salt structure and have Co^{2+} in tetrahedral sites is less active but also show CO oxidation reaction, which is probably due to the oxidation of top few layer into Co^{3+}, which is responsible for the CO oxidation reaction.[19] Co_3O_4 is not only known for low-temperature CO oxidation[22] but it is also extensively studied for other reaction also, such as hydrocarbon oxidation,[23] Fischer-Tropsch synthesis[24,25] etc.

To explore the role of nanorod morphology, Co_3O_4 without any particular morphology or random morphology was prepared and evaluated for CO oxidation around ambient temperatures in a MBI setup. Co_3O_4 was prepared in-situ on Co-metal foil in MBI by heating it at 600 K for 3 h in O_2 partial pressure of 5×10^{-6} Torr. In this process, few hundred atomic layers get oxidized into Co_3O_4 as was analyzed and confirmed by XRD and Raman Spectroscopy. Raman spectroscopy clearly shows the formation of Co_3O_4 on the surface of the catalyst with no sign of the presence of CoO on to the surface of catalyst.

From the MBI study on spinel surfaces, it is evident that CO oxidation activity occurs at room temperature as well as at 275 K. We have also studied the effect of moisture on CO oxidation reaction. We found that presence of H_2O in gas mixture inhibit the rate of reaction mostly at low temperature. Water molecules adsorbs on the active site strongly which prevents adsorption of reactant i.e.CO and O_2 molecules on the surface of catalyst due to which CO oxidation reaction is inhibited. From MBI studies, $CO:O_2$ = 1:3 ratio was found to be the optimum condition for the reaction, where it shows maximum activity for CO oxidation. Most of the studies claim that low-temperature CO oxidation is dependent on morphology and the plane exposed on the surface of catalyst.[19] From FE-SEM result we found that no particular morphology occur on the surface of catalyst even though it is active for CO oxidation at low temperature. This observation signifies that morphology may not be the critical factor deciding the reaction to occur at low temperatures, but it is the Co^{3+} site which is catalyzing the reaction.[19] From another independent XPS analysis, it has been found that Co-metal foil changes to Co_3O_4 at 500 K and below ambient pressures. Oxidation of Co

metal to Co_3O_4 occurs under very similar conditions in both studies, and this confirms the spinel formation in MBI conditions too. However, for the present chapter, detailed MB studies in UHV condition has been carried out on in-situ generated Co_3O_4 on Co-metal foil and its evaluation for CO oxidation under variety of conditions. A thin film of Co_3O_4 on Co-metal foil is characterized by XRD, Raman, and FE-SEM to know the structural and morphological details about the catalyst. A detailed study about the preparation of catalyst as well as the activity towards CO oxidation is explained in detail in this chapter.

5.2 Experimental Section

5.2.1 In-situ Preparation of Co_3O_4 in MBI

A polycrystalline Co-metal foil (MaTeck, Germany) of 1 x 1 cm^2 was placed in a niobium metal holder, which can be heated by tantalum wire from RT to 1200 K. Co-foil surface is cleaned first by dipping in 1 M aq. HNO_3 acid to remove the coarse oxidized surface layers. Acid-etched Co-metal foil was placed in MBI and then it is further cleaned several times by repeated-Ar^+ sputtering. Similar procedure was carried out in XPS to make sure the surface is completely metallic in nature. Then the surface of the Co-metal foil was exposed to controlled O_2 atmosphere in UHV chamber at a O_2 partial pressure of 5 x 10^{-6} Torr which is heated up to 600 K for 3 h. A few layer of the surface gets oxidized into spinel cobalt oxide. Formation of Co_3O_4 was confirmed by XRD, Raman and XPS spectra.

5.3 Results and discussion

5.3.1 XRD analysis

Fig. 5.1 shows the XRD pattern of the in-situ prepared Co-oxide on Co-metal foil. From Fig. 5.1 we can say that top few layer gets converted into Co_3O_4 under oxygen and temperature treatment in MBI. XRD pattern was recorded after the sample was removed from MBI. The peaks appear in XRD analysis is of low intensity and indicating that only top few layers are converted into spinel cobalt oxide. The peak which appears at 36.7º, 44.7º and 51.9º corresponds to (311), (400) and (420) facets of spinel cobalt oxide,[19] while peak appears at 42.2º corresponds to (200) facet of cubic CoO.[31] The observed XRD features confirms the formation of crystalline spinel cobalt oxide with face-centered cubic structure. Since prominent peaks are for Co_3O_4 with a moderate peak of CoO at 42.2º, so we can say that top few layers of Co-metal foil gets easily oxidized to spinel cobalt oxide at 600 K and 5 x 10^{-6} Torr O_2 pressure, which is stable even after exposing to atmosphere.

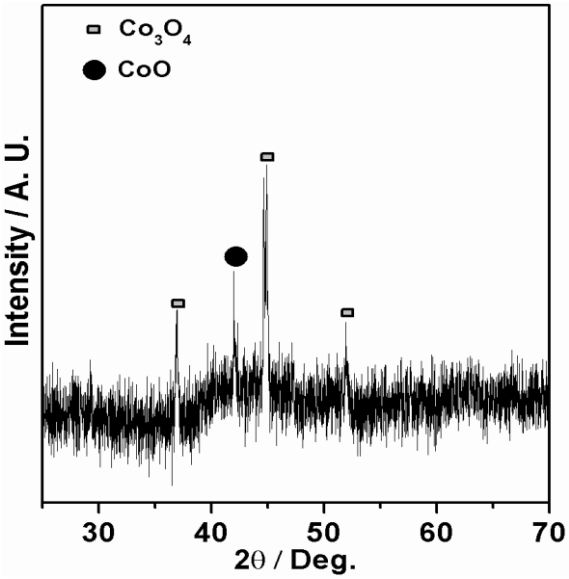

Fig. 5.1 XRD pattern of Co-Oxide formed on Co-metal foil in-situ in MBI at 10^{-6} mbar partial pressure of oxygen and 600 K.

5.3.2 Raman Analysis

Raman spectrum was recorded using 632 nm laser source and the result is shown in Fig. 5.2. Raman spectrum shows the typical features of Co_3O_4 on the surface. Raman spectrum of Co_3O_4 consists of five peaks which appears at 198, 487, 528, 627 and 696 cm^{-1} which corresponds to F_{2g}, E_g, F_{2g}, F_{2g}, and A_{1g} modes of crystalline spinel cobalt oxide.[32] High intense peak at 198 cm^{-1} and other broad peak at 528 cm^{-1} are observed, this is due to oxygen vibration involving E_g, O-Co-O bending, and A_{1g}, O-Co stretching modes.

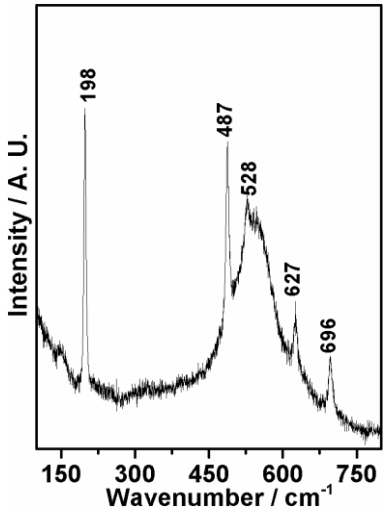

Fig. 5.2 Raman spectrum of Co_3O_4 prepared on Co-metal foil in MBI.

5.3.3 FE-SEM Analysis

Fig. 5.3 shows the FE-SEM images of surface of Co_3O_4 formed on Co-metal foil in MBI. From Fig. 5.3 we can say that no regular morphology was formed on the surface. The surface of Co_3O_4 is very rough which is granular in nature as shown in Fig. 5.3b.

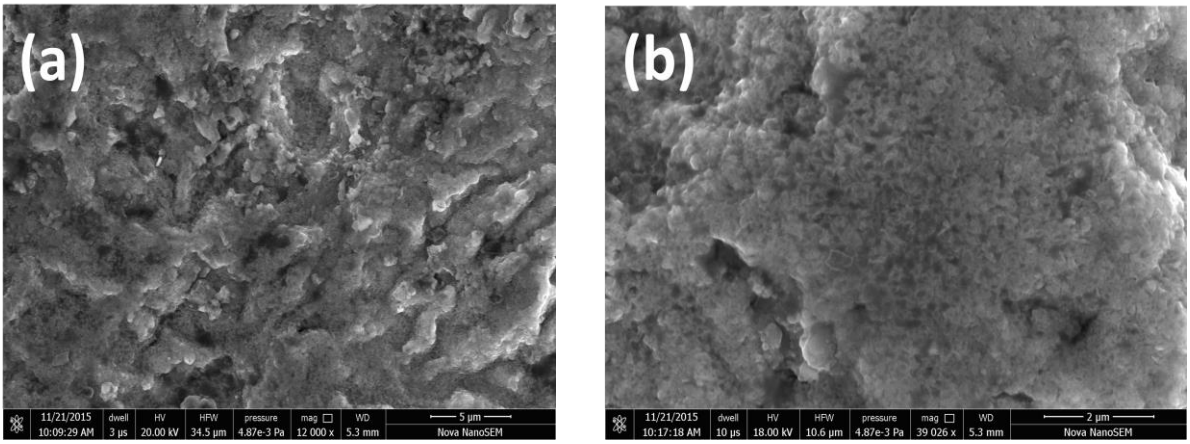

Fig. 5.3 FE-SEM image of surface of Co_3O_4 disclosing no specific morphology formed on surface at different magnifications. Scale bar shown in a) 5 µm and b) 2 µm.

5.3.4 Molecular Beam Study of CO oxidation on in-situ prepared Co_3O_4 surface.

MB studies of CO oxidation have been carried out on in-situ prepared $Co_3O_4$from Co metal foil. CO oxidation with different $CO:O_2$ ratios was carried out on Co_3O_4 in a temperature regime from room temperature (RT = 293 K) upto 375 K in ascending and descending order of temperature with no observable differences or hysteresis in reaction pattern. The reaction was also carried out at 275 K for $CO:O_2$ ratio of 1:2 as well as 1:3. The in-situ generated catalyst was activated in O_2 atmosphere at $5x10^{-6}$ Torr) for half an hour at 723 K. The reaction was carried out under isothermal condition with steady state (SS) values reproducible several times within the experimental error limit of 10 %. The catalyst surface was activated after every reaction to regain the virgin surface. Fig. 5.4 shows the CO oxidation with $CO:O_2$ = 1:1 and 1:3 ratio at 300 K. At t = 10 s the MB with reactants gaseous mixture was introduced into the UHV chamber while keeping the shutter in closed position; this prevents any direct impingement of MB on to the surface of catalyst. At t = 20 s shutter was opened to allow direct interaction of MB with surface of catalyst at 300 K. A decrease in the partial pressure of CO and O_2 was observed which indicates its adsorption as well as consumption during the course of reaction. Transient state was observed for the first few seconds and reaction reaches SS within 30 seconds. During the reaction, MB was blocked after every 60 s to reproduce the kinetic data as well as to study the rate of reaction in the SS. As soon as the shutter was opened there is an increase in partial pressure of CO_2 observed which reaches SS immediately. At t = 80 s the shutter was closed which is marked by an increase in the partial pressure of reactant i.e. O_2 and CO with a decrease in partial pressure of product i.e. CO_2. This confirms the CO oxidation occurs at ambient temperature on Co_3O_4 surface. A close observation of Fig. 5.4a and b reveals that the rate of O_2 and CO uptake is

high with $CO:O_2$ = 1:3 and hence high CO_2 production, compared to that of 1:1 ratio. This suggests that net adsorption is totally dependent on the reaction condition. It is likely that large amount of CO poisons the surface and hence significantly low reactivity was observed with 1:1 beam composition. CO oxidation was measured with different ratios of CO and O_2, and it was observed that the rate of CO oxidation was maximum with $CO:O_2$ ratio of 1:3; it is shown in Fig. 5.4b. Finally at t = 380 s the MB was turned off.

To explore more about CO oxidation, it was carried out as a function of temperature and different $CO:O_2$ compositions. Fig. 5.5 shows the experimental kinetic data of CO oxidation with $CO:O_2$ ratio of 1:3 as a function of temperature. This reaction was carried in a similar way as described above but with a difference of shutter movement i.e. MB was kept open for every 120 s, while it is closed for 60 s only. The reaction temperature was increased between RT (293 K) and 375 K after every 180 s by 15 K. The MB was opened at t = 30 s which is marked by an increase in partial pressure of CO_2 and a simultaneous decrease in the partial pressure of CO and O_2.

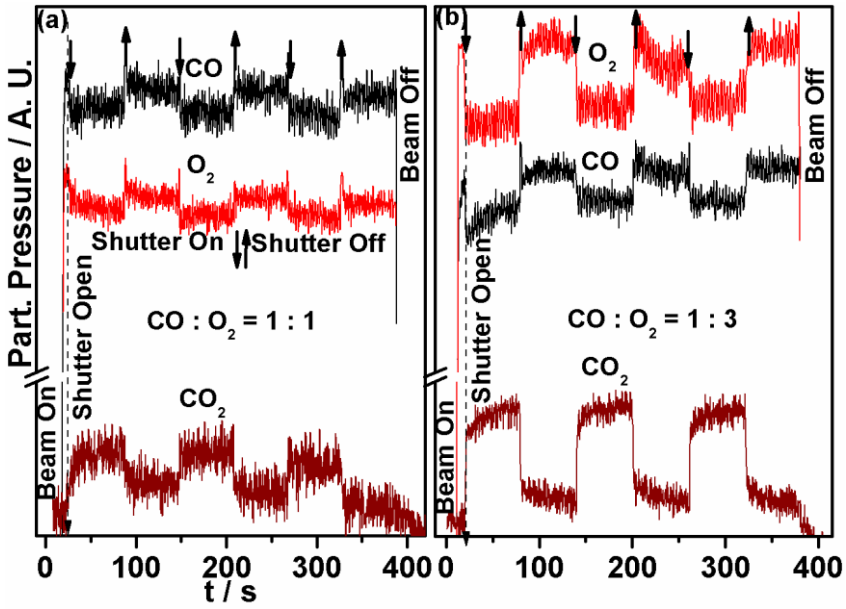

Fig. 5.4 CO oxidation reaction measured at 300 K on in-situ generated Co_3O_4 with $CO:O_2$ ratio of a) 1:1, and b) 1:3. MB oscillation was made after every 60 s to reproduce the kinetic data. Note the higher oxidation activity with 1:3 compositions of reactants in panel b.

The MB was blocked at t = 150 s with a decrease in partial pressure of product and increase in partial pressure of reactant. At t = 210 s the MB was opened at RT. At t = 240 s the temperature of reaction was increased from RT to 300 K which shows a minimal increase in formation of CO_2 with increase in temperature as shown in Fig. 5.5 inset. At t = 600 s and at 330 K we found that the SS is not reached with passage of time. There was a marginal increase in CO_2 formation which shows a possibility of diffusion on the surface of catalyst

with further increase of temperature of reaction. Diffusion assisted CO_2 formation gives an indication of possible diffusion of reactants and products, which is happening during reaction condition. It is to be noted that diffusion is an activated process, which occurs faster at higher temperatures. From Fig. 5.5 we also observe that with increase in temperature of

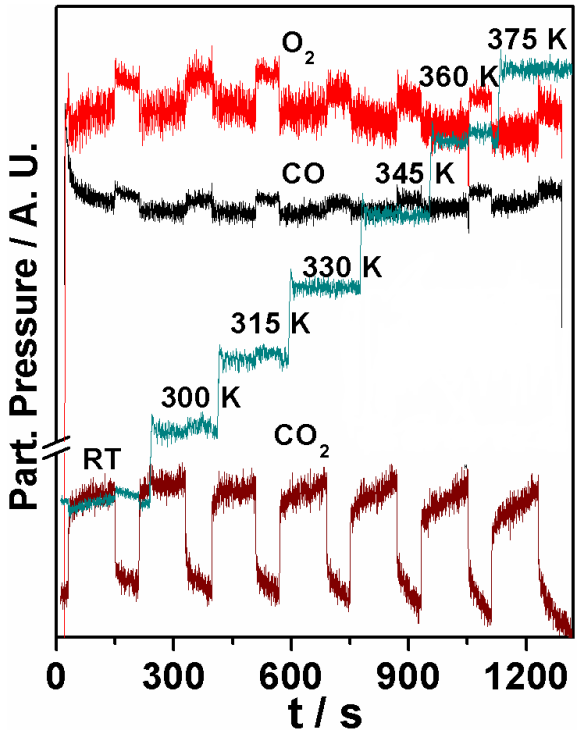

Fig. 5.5 Typical raw kinetic data for CO oxidation as a function of temperature with an effusive 1:3 $CO:O_2$ MB directed onto the surface of Co_3O_4. The MB was blocked and unblocked after 120 s and 60 s, respectively, to study the kinetic aspects of reaction.

reaction the rate of O_2 as well as CO uptake remains more or less constant which underscores that increasing temperature has a minimal effect on rate of adsorption of reactants. However, the slow decay observed with CO_2 for shutter oscillations underscores the diffusion controlled nature of the reaction at high temperatures. Porosity observed in FESEM images supports the porous channels available for diffusion, which increases the accessibility to more number of active sites in the pores. About 70 % increase or decrease in the rate of CO_2 formation at temperatures higher than 340 K for shutter opening or closing, respectively, demonstrates the major contribution to the reaction arises from surface sites from molecular beam. Up to 30 % contribution to the reactivity comes from surfaces available in the pores and subsurfaces at high temperatures.

Fig. 5.6 shows the CO oxidation reaction for 1:3 ratio at 275 K and observed that reaction occurs at this temperature also. The low temperature CO oxidation occurs even with the presence of random morphology on surface of catalyst was confirmed by FE-SEM. Many studies[18,19] claims that low temperature CO oxidation occurs on nanorod morphology with

(011) plane exposed; our study found that presence of Co^{3+} on the surface of catalyst, as was confirmed by XPS, is the driving factor for low temperature CO oxidation of Co_3O_4. Fig. 5.6 demonstrates that CO oxidation increases with increase in oxygen-content in the molecular beam. For MB oscillations, a clear change in partial pressure of O_2 and CO was observed and it signifies that they are consumed during the course of the reaction. Increase in partial pressure of CO_2 on shutter closing signifies that they are formed during reaction. CO oxidation occurs at sub-ambient temperatures and it is observed with in-situ generated Co_3O_4 spinel too. This is in good agreement with the literature reports; however, it is to be underscored that there is no specific morphology associated with the spinel reported in the present system. CO_2 production is comparable to that of observed at high temperature (350-375 K). Further, sharp changes in CO_2 decay kinetics indicates that there is no diffusion of reactants into the porous channels, which is in contrast to the observation made at high temperatures. Shutter operation was made several times to reproduce the kinetic data. This also confirms that this is a suitable catalyst for the CO oxidation reaction at lower temperature.

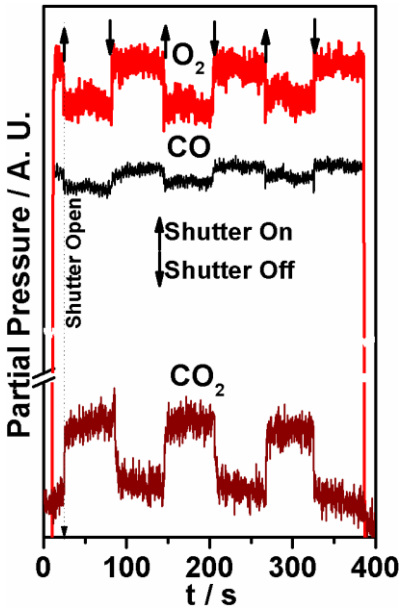

Fig. 5.6 CO oxidation reaction at 275 K with $CO:O_2$ in 1:3 ratio.

To explore the effect of different $CO:O_2$ composition on CO oxidation, systematic studies has been conducted and the results are shown in Fig. 5.7. From Fig. 5.7 it is observed that with CO rich composition, i.e. $CO:O_2$ = 2:1, initially after shutter opening it takes nearly 120 s to reach the steady state. It underscores that CO is strongly adsorbed to the surface of catalyst at RT and in the presence of CO-rich compositions, and hence it inhibit O_2 adsorption due to which SS is delayed for CO_2 production. However, with increasing O_2-

content in the reaction mixture, this trend changes and SS was observed faster. Indeed with 1:3 composition and other O_2-rich compositions, reaction reaches SS instantly on opening the shutter at 293 K, demonstrates the large amount of CO hampers CO oxidation due to poisoning the catalyst surfaces. It was observed from Fig. 5.7 that as the $CO:O_2$ ratio changes from 2:1 to 1:3, SS for CO_2 formation is attained immediately upon opening the shutter at t = 20 s; this infers the enhancement in the rate of CO_2 formation on heading towards O_2 rich MB.

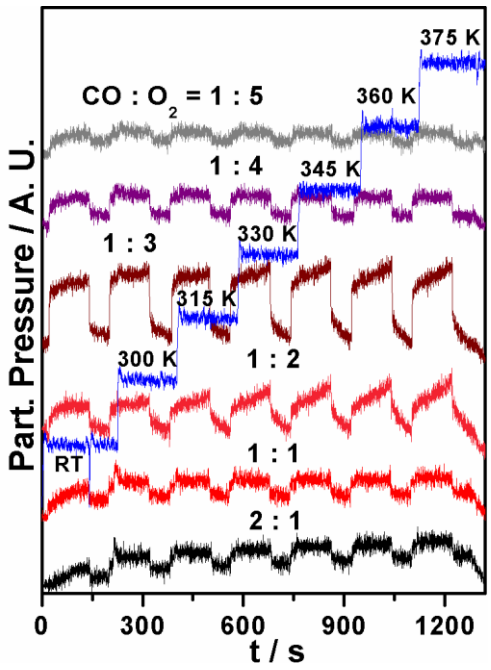

Fig. 5.7 Experimental data for formation of CO_2 as a function of temperature with different CO/O_2 compositions from 2:1 to 1:5. The procedure for calculating the rate of formation of product is similar to as described in Fig. 5.4 and 5.5.

On increasing the temperature from 293 K to higher temperatures, SS has been reached faster. This is supported by the experimental data. However, CO poisoning seems to continue even at high temperatures with O-rich reactants compositions (2:1 and 1:1) and hence rate observed was also low. With 1:2 and other O_2-rich compositions demonstrates the fast reaching of SS, almost instantly, from 293 K and above. Further, a significant increase in CO_2 production was observed at high temperatures. In fact, as discussed earlier, diffusion of reactants occur at higher temperatures and hence an increase in CO_2 production was observed. Further change of $CO:O_2$ ratio from 1:3 to 1:4 and 1:5 decreases the CO_2 production and hence a decline in the rate of formation of CO_2 was observed. This study confirms that 1:3 CO/O_2 ratio is the optimum condition for CO oxidation. It was also observed from Fig. 5.7 that with increase in the reaction temperature, an increase in the formation of CO_2 was observed; however, it is not as dramatic as observed on noble metals.

We also attribute this increase in CO_2 production to limited diffusion of reactants into the pores and subsurfaces, which increases the availability of active sites.

We have further calculated the rate of reactants consumption as well as formation of products. Fig. 5.8a shows the rate of consumption of O_2 and CO at 300 K for different CO/O_2 ratio, while Fig. 5.8b shows the formation of product. From Fig 5.8a demonstrates that the rate of O_2 consumption increases with increase in O_2 content of the molecular beam upto 1:3 CO/O_2 ratio, while CO consumption increases upto 1:2 CO/O_2 ratio. The increase of reactant consumption upto 1:3 ratio and decline thereafter with increase in O_2 rich MB suggests that 1:3 is the optimum composition for CO oxidation reaction to occur on the surface of Co_3O_4. This clearly infers that neither CO rich MB nor O_2 rich MB is the optimum condition of the reaction. Nearly 1:1 ratio of CO to O-atoms observed in Fig. 5.8a reiterates that optimum amount of both reactant species are available on the surface of catalyst with 1:3 composition. According to first order rate equation the above condition provides the maximum rate and the same was observed experimentally. Fig. 5.8b shows the rate of formation of CO_2 as a function of temperature with respect to CO/O_2 ratio. It is observed that with increase in temperature of reaction, increase in rate of formation of CO_2 is minimal with CO or O_2 rich reactants compositions. For 1:2 and 1:3 CO/O_2 ratio there is an increase in the rate of formation of CO_2 with increase in temperature to a significant extent. This is mainly due to the optimum compositions of both adsorbates on the surface of the catalyst.

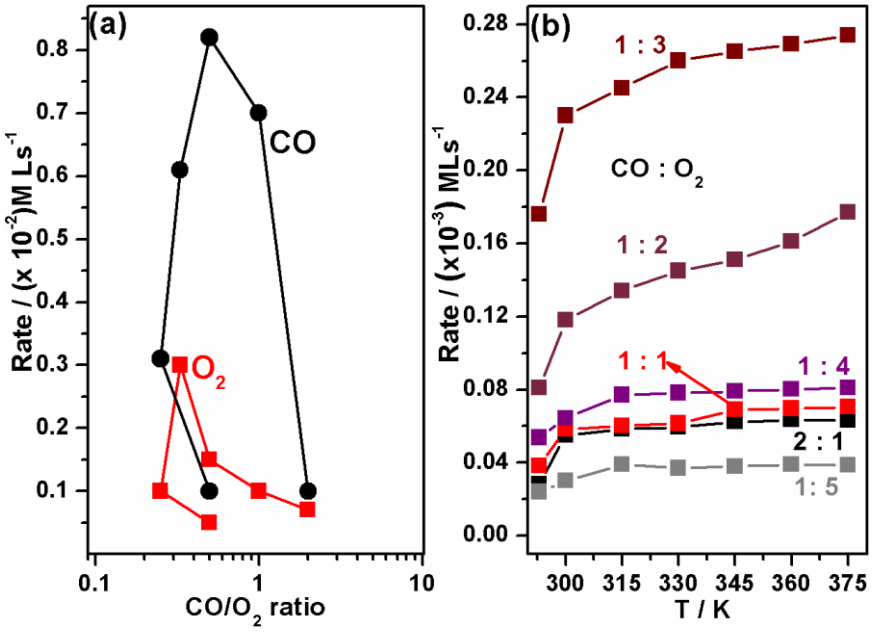

Fig. 5.8 a) Rate of consumption of reactants at 300 K as a function of O_2/CO ratio, and b) Rate of formation of CO_2 as a function of temperature and CO/O_2 ratio.

Presence of moisture in feedstock, generally, inhibits the rate of CO oxidation on many oxide based catalysts and Co_3O_4, also shows similar behaviour. This occurs mainly because of the adsorption of water molecules and possibly dissociates on the active site of catalyst and thus inhibits the reaction. Effect of H_2O vapour present in the reaction mixture was evaluated to understand the nature of spinel catalysts. $CO:O_2$ in 1:3 ratio was maintained for this particular study and mixed with various amount of H_2O vapour with it and used as feedstock for CO oxidation. Fig. 5.9a shows the CO oxidation data measured at 400 K with $CO:O_2:H_2O$ in 24:72:1 ratio; while Fig. 5.9b shows the rate of CO oxidation as a function of temperature with different $CO:O_2:H_2O$ ratios. In terms of partial pressure of reaction mixture, water vapour was increased from 1, 2 and 5 %, while maintaining the 1:3 ratio of $CO:O_2$. Fig. 5.9a shows CO_2 production under steady state conditions at 400 K with 1 % water present in the feedstock. However, no CO oxidation occurs below 350 K even with 1 % water vapour. A careful analysis of experimental data shown in Fig. 5.9a suggests that the CO adsorption seems to be a limiting factor, while oxygen adsorption was observed nicely. A comparison of Figs. 5.9a and 5.4b (CO oxidation at 300 K with 1:3 composition) supports the above point. It is likely that adsorbed CO might undergo some changes towards carbonate, formate group formation. However, this needs to be confirmed by other methods, such as IR.

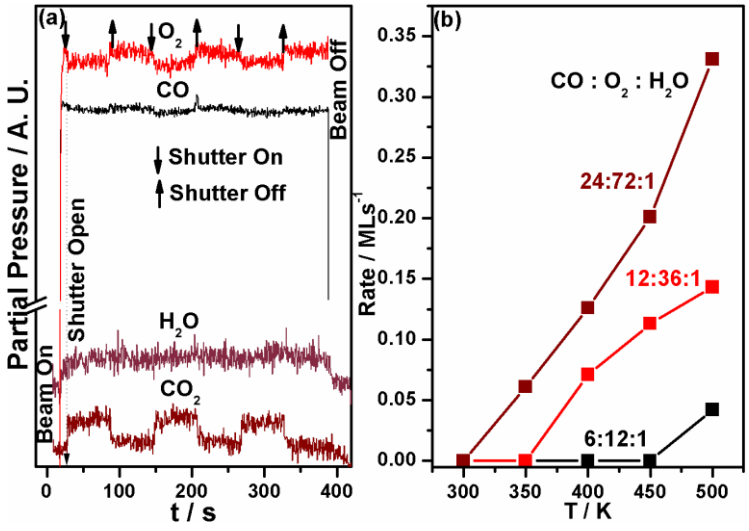

Fig. 5.9 a) CO oxidation reaction at 400 K on Co_3O_4 with 24:72:1 $CO:O_2:H_2O$ ratio. The shutter operation was done after every 60 s to reproduce the kinetic data within experimental limits, and b) rate of formation of CO_2 as a function of temperature different $CO:O_2:H_2O$ ratio of gaseous mixture.

A CO_2 production rate value, measured from raw kinetic data, is plotted in Fig. 5.9b shows very interesting results. As the water partial pressure increases from 1, 2 to 5 %, onset of CO oxidation also shifts towards high temperatures from 350, 400 and 500 K, respectively. This reflects that presence of increasing amount of water vapour in gaseous feedstock

increasingly inhibits the rate of reaction as it blocks the active site of adsorption for $CO+O_2$. Even though water molecules might desorb around the boiling point of water at 373 K, 5 % water containing reactant mixture shows reaction at and above 500 K suggests the formation of possible impurities and intermediates, such as carbonate, formates etc. This highlights the shifting of oxidation regime to higher temperatures in the presences of water vapour.

5.4 Conclusion

Co_3O_4 thin film was generated in-situ on Co-metal foil under UHV at a chamber pressure of $5x10^{-6}$ Torr at 600 K. Co_3O_4 thin film generated displays random morphology as was disclosed by FE-SEM. XRD, and Raman spectra confirms the formation of spinel cobalt oxide on surface of Co-metal foil. MB study of CO oxidation on Co_3O_4 reveals that the reaction occurs at sub-ambient temperatures, 275 K, and temperature has a marginal effect on the rate of reaction. However, due to the porosity associated with Co_3O_4 thin film, diffusion of reactants occur and this increases the activity significantly by exposing to more number of active sites at high temperatures. It is also found from the MB study that neither CO rich MB nor O_2 rich MB is suitable for CO oxidation. 1:3 $CO:O_2$ ratio seems to be optimum condition for CO oxidation reaction on Co_3O_4. It is also found that presence of H_2O in the feedstock inhibits the rate of reaction, likely by poisoning the surface with carbonate or formate below 400 K and hence ambient oxidation activity was no longer observed in the presence of water vapour. A key finding is the requirement of nanorod morphology is not necessary for ambient CO oxidation, which is in contrast to the existing literature reports.

5.5 References

1. V. Johanek, S. Schauermann, M. Laurin, C. S. Gopinath, J. Libuda, H. J. Freund, *J. Phys. Chem. B* **2004**, *108*, 14244.
2. K. Thirunavukkarasu, K. Thirumoorthy, J. Libuda, C. S. Gopinath, *J. Phys. Chem. B* **2005**, *109*, 13272.
3. F. Zaera, C. S. Gopinath, *J. Chem. Phys.* **1999**, *111*, 8088.
4. L. Liu, F. Zhou, L. Wang, X. Qi, F. Shi, Y. Deng, *J. Catal.* **2010**, *274*, 1.
5. A. M. Arias, M. F. Garcia, A. I. Juez, A. B. Hungria, J. A. Anderson, J. C. Conesa, J. Soria, *Appl. Catal. B* **2001**, *31*, 51.
6. Y. Fang, Y. Yao, *J. Catal.* **1984**, *87*, 152.
7. A. Dubey, S. Kolekar, E. S. Gnanakumar, K. Roy, C. P. Vinod, C. S. Gopinath, *Catal. Struc. React.* **2015**, http://dx.doi.org/10.1080/2055074X.2015.1133269.
8. E. S. Gnanakumar, J. M. Naik, M. Manikandan, T. Raja, C. S. Gopinath, *ChemCatChem* **2014**, *6*, 3116.

9. S. Nagarajan, K. Thirunavukkarasu, C. S. Gopinath, *J. Phys. Chem. C* **2009**, *113(17)*, 7385.
10. D. Valechha, S. Lokhande, M. Klementova, J. Subrt, S. Ravalu, N. Labhsetwar, *J. Mater. Chem* **2011**, *21*, 3718.
11. C. Hardacre, R. M. Ormerod, R. M. Lambert, *J. Phys. Chem.* **1994**, *98*, 10901.
12. C. H. F. Peden, D. W. Goodman, D. S. Blair, S. H. Oh, *J. Phys. Chem.* **1988**, *92*, 1563.
13. A. Piednoir, M. A. Languille, L. Piccolo, A. Valcarcel, F. J. C. S. Aires, J. C. Bertolinia, *Catalysis letters* **2007**, *114*, 110.
14. M. Shelef, R. W. McCabe, *Catal. Today* **2000**, *62*, 35.
15. K. M. Adams, G. W. Graham, *Appl. Catal. B* **2008**, *80*, 343.
16. M. Haruta, S. Tsubota, T. Kobayashi, H. Kageyama, M. J. Genet, B. Delmon, *J. Catal.* **1993**, *144*, 175.
17. X. Xie, Y. Li, Z. Q. Liu, M. Haruta, W. Shen, *Nature letters* **2009**, *8*, 746.
18. R. Jin, Y. Chen, W. Li, W. Cui, Y. Ji, C. Yu, Y. Jiang, *Appl. Catal. A: Gen.* **2000**, *201*,71.
19. D. Gu. C. J. Jia, C. Weidenthaler, H. J. Bongard, B. Spliethoff, W. Schmidt, F. Schuth, *J. Am. Chem. Soc.* **2015**, *137*, 11407.
20. D. A. H. Cunningham, T. Kobayashi, N. Kamijo, M. Haruta, *Catal. Lett.* **1994**, *25*, 257.
21. C. J. Jia, M. Schwickardi, C. Weidenthaler, W. Schmidt, S. Korhonen, B. M. Weckhuysen, F. Schuth, *J. Am. Chem. Soc.* **2011**, *133*, 11279.
22. P. Thormahlen, M. Skoglundh, E. Fridell, B. Anderson, *J. Catal.* **1999**, *188*, 300.
23. a) E. Garbowski, M. Guenin, M. C. Marion, M. Primet, *Appl. Catal.* **1990**, *64*, 209. b) M. Meng. P. Y. Lin, Y. L. Fu, *Catal. Lett.* **1997**, *48*, 213.
24. D. Schanke, A. M. Hilmen, E. Bergene, K. Kinnari, E. Rytter, E. Adnanes, A. Holmen, *Catal. Lett.* **1995**, *34*, 269.
25. J. Rathousky, A. Zukal, *Appl. Catal. A* **1991**, *79*, 167.
26. T. Mathew, K. Sivaranjani, E. S. Gnanakumar, Y. Yamada, T. Kobayashi, C. S. Gopinath, *J. Mater. Chem.* **2012**, *22*, 13484.
27. P. A. Bharad, K. Sivaranjani, C. S. Gopinath, *Nanoscale* **2015**, *7*, 11206.
28. K. Roy, C. P. Vinod, C. S. Gopinath, *J. Phys. Chem. C.* **2013**, *117*, 4717.
29. K. Thirunavukkarasu, C. S. Gopinath, *Catal. Lett.* **2007**, *119*, 50.
30. K. Thirunavukkarasu, K. Thirumoorthy, J. Libuda, C. S. Gopinath, *J. Phys. Chem. B.* **2005**, *109*, 13272.
31. Y. Sun, X. Hu, W. Luo, Y. Huang, *J. Mater. Chem.* **2012**, *22*, 13826.
32. Y. Jin, L. Wang, Y. Shang, J. Gao, J. Li, X. He, *Electrochimica Acta* **2015**, *151*, 109.

Chapter 6–Summary and Outlook

6.1 Summary and Outlook

In this thesis, we made an attempt to explore the possible ways in which surface science can help to address the fundamental problem of catalysis. Since the surface of real-world catalyst is very complex, and the complexity is expected to increase further under reaction conditions. Often, the active phase of the catalyst occurs exclusively under reaction conditions. Hence, it is very challenging to study the changes that occur on the catalyst surfaces and not many methods are available. So to explore the catalysis at atomic level, but on real-world working catalyst, is a difficult task and this can be achieved by bridging the material gap between ideal materials (such as single crystals) employed in surface science, and highly complex powder materials employed in industrial heterogeneous catalysis. The emphasis of the current thesis is mainly on addressing to bridge the material gap that exists between the above two extreme conditions.

The major problem in industrial catalysis is how to make a product cost effective through an environmental friendly manner; this is still a very big question? Very minimum amount of fundamental studies are available on working catalysts, especially with surface science and other relevant methods. One potential way to address this serious issue is to prepare thin films of an acceptable surface quality of industrial catalyst and evaluate the catalyst surface with surface sensitive analytical methods under technically relevant conditions or close to those conditions. It is also equally important to incorporate typical characteristics of industrial catalysts, such as porosity, high surface area, along with high surface quality needed for surface analysis. Indeed, they are contradictory characteristics and they cannot go together, at the extreme ends. Nonetheless, a compromise or optimization between those two extremes would lead to a porous thin film with acceptable surface qualities and porous characteristics. Surface science studies on such thin films (better than flat model catalysts) under technically relevant conditions are expected to bridge the material gap. A variety of surface science technique can be applied to study the structural, spectral and electronic properties of the system under study. The aim of this thesis is to study a variety of catalytic and mechanistic aspects of the simple and complex reactions on porous thin films.

This thesis is basically divided into three working chapters. First one is on preparation of ceria-zirconia (CZ) thin film with an aim to bridge the material gap. First part (Chap. 3A)

addresses O_2 adsorption on CZ thin film in MBI and CO oxidation on CZ powder sample; a good correlation was observed between the two parameters measured at extremely different pressure conditions. Indeed this aspect fully bridges the material and pressure gaps simultaneously. We analysed these two different reactions (OSC in MBI and CO oxidation at ambient pressure in a typical reactor) and could demonstrate that with an increase in temperature of reaction or adsorption, rate of CO oxidation and rate of O_2 adsorption increases. Thus we found one to one correlation between O_2 adsorption and CO oxidation reaction. With an increase in temperature, redox property of the catalyst increases which increases the oxygen mobility, thus helpful in catalyzing the reaction. Although this correlation was known from bulk material studies, probably this is the first report to demonstrate the same correlation by addressing the material gap. It is important to highlight the thin film characteristics achieved, which are about 30-50 nm thick, porous, possess desired surface qualities to be evaluated by surface sensitive methods. Porous characteristics ensure the diffusion of reactants/products, which is the prime requirement to meet the industrial catalyst properties, while maintaining high surface qualities to make meaningful surface science measurements, such as sticking coefficient. Although these are the positive points, it is also highly desired to decrease the thickness of the thin films to be around 10 nm or less. This would ensure the diffusion phenomenon to be studied at a better level.

The second part (Chap. 3B) consists of C-H activation of methane on CZ and manganese doped CZ (MCZ) thin films. CZ thin film shows selective oxidation of methane to formaldehyde, while MCZ thin film shows partial oxidation of methane to syngas (Chap. 4). On doping of Mn into CZ lattice lowers the temperature for C-H activation of methane by 300 deg. There are many other important reactions, such asNH_3 synthesis, Fischer-Tropsch reaction, water-gas shift reaction, reforming reactions can be addressed and studied better by surface science techniques to know kinetic and mechanistic aspect. Energy and fuel related industrial catalysis occur at high to very high temperatures. A better understanding of fundamental aspects of energy/fuel related catalysis would lead to an understanding of the obstacles and how to overcome the same. This could lead to operate the same catalysis with less deterioration and better selectivity too.

C-H activation of methane is a perennial issue, since large amount of methane is flared currently, just to add $CO_2$to the environment. A surprise was waiting for us to explore the C-H activation on MCZ surfaces. A key finding was the competition and cooperation among the elementary reactions, which is not anticipated by us or in the literature. Diffusion

of small and light-weight atoms, such as H, is so fast that it combines with oxygen atoms to form water (when oxygen available) or desorbs as H_2 (when oxygen not available). In the absence of oxygen, CO, CO_2 and H_2 formation occurs. Even though CO, CO_2 and H_2O formation are oxidation reactions, former two occur under oxygen-less conditions is a surprise. Present studies on the partial oxidation of methane on MCZ surfaces lead to the mechanistic aspect of reaction, which is the combustion-reformation pathway. We believe, these are the inputs definitely help to develop the catalysts further as well as to fine tune the reaction conditions to move towards desired product(s) selectivity. C-H activation towards desired products is highly dependent on low contact time and molecular beam offers the same. Hence, it is prudent to select the right surface science method too to study the catalysis.

The third part of thesis (Chapt. 5) consists of *in-situ* preparation of thin film of spinel cobalt oxide on Co metal foil in MBI. We have carried out CO oxidation on spinel cobalt oxide thin film which shows ambient and sub-ambient CO oxidation reaction. Literature reports suggested that nanorod morphology is essential to catalyze ambient and sub-ambient temperature CO oxidation reaction. However, we are able to demonstrate the same, but without any particular (or random) morphology. Low temperature CO oxidation is also severely hampered by the presence of moisture in the feedstock. Surface science discloses that presence of Co^{3+} is a necessary condition for catalyzing the reaction rather than any particular morphology.

All these work which is discussed in this thesis was made with an aim to bridge the material gap to address some of the unsolved problems in the field of heterogeneous catalysis. This type of work can be carried out further to solve many issues. We consider our efforts are similar to a baby's first steps in addressing the material gap to understand the real-world catalysis on thin film surfaces (prepared in a simple wet chemical laboratory) with surface science methods. Few different techniques available, such as near-ambient pressure photoelectron spectroscopy, pressure dependent IR studies, should also be employed to investigate the electronic nature of the surfaces to gain more insights of working of industrial catalysts. Indeed, there are number of catalysts systems are available to study by these methods for a variety of reactions. Addressing pressure and material gaps simultaneously would add more value to the heterogeneous catalysis area of research. With our publications, including the present thesis, more such efforts are likely to come from across the globe. In the not so distant future, heterogeneous catalysis may not be considered as black box magic.